2020

Two-Dimensional Nanomaterials and Their Composites for Electrochemical Detection of Toxic Mercury Ions in Water

Md Tawabur Rahman
South Dakota State University

TWO-DIMENSIONAL NANOMATERIALS AND THEIR COMPOSITES FOR ELECTROCHEMICAL DETECTION OF TOXIC MERCURY IONS IN WATER

BY

MD TAWABUR RAHMAN

A dissertation submitted in partial fulfillment of the requirements for the

Doctor of Philosophy

Major in Electrical Engineering

South Dakota State University

2020

DISSERTATION ACCEPTANCE PAGE

Md Tawabur Rahman

This dissertation is approved as a creditable and independent investigation by a candidate for the Doctor of Philosophy degree and is acceptable for meeting the dissertation requirements for this degree. Acceptance of this does not imply that the conclusions reached by the candidate are necessarily the conclusions of the major department.

Qiquan Qiao
Advisor Date

Siddharth Suryanarayanan
Department Head Date

Dean, Graduate School Date

ACKNOWLEDGMENTS

Having the opportunity to work as a graduate research assistant, I am thankful to Dr. Qiquan Qiao for his support and supervision at South Dakota State University. I have been able to complete this research work and improve the dissertation with his direct guidance and inspiration. The whole research was supported by the Economic Development Administration University Center (ED18DEN3030025), National Science Foundation-Major Research Instrumentation (NSF-MRI) (Grant 1428992), and NSF Innovation Corps (1906755), EE Ph.D. program at South Dakota State University.

I am thankful to my committee members including Dr. Parashu Kharel, Dr. Huitian Lu, and Mr. Jason Sternhagen for their precious time to review my dissertation and suggestions to further improve the quality of the dissertation. I am grateful to Khan Mamun Reza, Ashraful Haider Chowdhury, Rajesh Pathak, Ke Chen, Ashim Gurung, Abdullah Al Maruf, Buddhi Sagar Lamsal, Behzad Bahrami, Md Faisal Kabir, Md Nazmul Hasan, and all my group members for their enormous support throughout research work.

Finally, I am grateful to my mother, family members, wife, and my little princess Junaina for their love and support.

TABLE OF CONTENTS

ABBREVIATIONS

AgNWs	silver nanowires
ASV	Anodic Stripping Voltammetry
aM	attomolar
AFM	Atomic Force Microscopy
CV	Cyclic Voltammetry
DPV	Differential Pulse Voltammetry
EIS	Electrochemical Impedance Spectroscopy
EPA	Environmental Protection Agency
FTIR	Fourier-Transform Infrared Spectroscopy
GCE	Glassy Carbon Electrode
GO	Graphene Oxide
HEMT	High Electron Mobility Transistors
LDR	Linear Detection Range
LOD	Limit of Detection
M	Molar
mL	milliliter
ng	nanogram
nM	nanoMolar
nm	nanometer
ppb	parts per billion
ppm	parts per million
pM	picoMolar
Pt	platinum

rGO	reduced Graphene Oxide
R_{ct}	charge transfer resistance
RSD	Relative Standard Deviation
s.d.	standard deviation
SWASV	Square Wave Anodic Stripping Voltammetry
SEM	Scanning Electron Microscopy
TEM	Transmission Electron Microscopy
TMDs	Transition Metal Dichalcogenides
WS_2	tungsten disulfide
WHO	World Health Organization
XRD	X-Ray Diffraction
µM	Micromolar
µA	Microampere
2D	Two-Dimensional

LIST OF FIGURES

LIST OF TABLES

ABSTRACT

TWO-DIMENSIONAL NANOMATERIALS AND THEIR COMPOSITES FOR ELECTROCHEMICAL DETECTION OF TOXIC MERCURY IONS IN WATER

MD TAWABUR RAHMAN

2020

The presence of trace amounts of mercury ion (Hg^{2+}) in drinking water has a detrimental effect on human health. The development of an electrochemical sensor for Hg^{2+} detection is still challenging to obtain ultra-trace sensitivity, excellent selectivity, wide Linear Detection Ranges (LDRs), and ultra-low detection limit. This work presents an electrochemical sensor based on two-dimensional nanomaterials and their composites for the enhanced sensing of Hg^{2+} in water. Graphene oxide (GO)-silver nanowires (AgNWs) composite and metallic 1T phase tungsten disulfide (WS_2) microflowers were utilized for the fabrication of electrochemical sensors using drop-casting. Under the optimized experimental conditions, the GO-AgNWs composite modified sensor showed a high sensitivity of ~ 0.29 µA/nM and linear response in the range of 1-70 nM toward Hg^{2+}, whereas 1T-WS_2 microflowers modified sensor showed excellent sensitivities of ~ 15.9 µA/µM, 2.54 µA/µM, 13.84 µA/µM, and 0.04646 µA/µM toward Hg^{2+} with LDRs of 1-90 nM, 0.1-0.4 µM, 0.5-1.0 µM, and 0.1-1.0 mM, respectively. An ultra-low detection limit of 0.1 nM and 0.0798 nM or 79.8 pM toward Hg^{2+} was obtained by GO-AgNWs composite and 1T-WS_2 modified sensors, which are well below the guideline value recommended by the World Health Organization and the United States Environmental Protection Agency. The sensors exhibited excellent selectivity for Hg^{2+} against other heavy metal ions including Cu^{2+}, Fe^{3+}, Ni^{2+}, Pb^{2+}, Cr^{3+}, K^{+}, Na^{+}, Ag^{+}, Sn^{2+}, and Cd^{2+}. The thus obtained

excellent sensitivity and selectivity with wide LDRs and ultra-low detection limits can be attributed to the synergistic effect of GO and conductive AgNWs, high conductivity, large surface area microflower structured 1T-WS_2, and the complexation of Hg^{2+} ions with sulfur (S^{2-}) and GO. In addition to good repeatability, reproducibility, and stability, these sensors showed practical feasibility of Hg^{2+} detection in tap water suggesting a promising device for real applications.

CHAPTER 1 INTRODUCTION

1.1 Background

1.1.1 Heavy Metals, Sources, and Effects

Heavy metals are all around such as in the air, water, food, etc. To date, there is no globally accepted definition for heavy metals. However, the toxic elements that have a density of more than 5 g cm^{-3} and atomic weights between 63.5 and 200.6 g mol^{-1} are known as heavy metals [1-3]. A trace amount of heavy metals has detrimental effects on human health and other living organisms due to their adverse toxicity and non-biodegradability [4, 5]. Table 1.1 summarizes different heavy metals with their sources effects, and permissible limits recommended by the World Health Organization (WHO) and the Environmental Protection Agency (EPA).

Mercury is a widely known toxic and non-biodegradable metal and a threat to public health and the environment [6, 7]. There are three forms of metal Hg in the environment such as elemental, inorganic, and organic compounds. The accumulation of inorganic mercury into the human body through the food chain can cause several serious diseases including arrhythmia, erethism, cardiomyopathy, nephrotic syndrome, pulmonary edema [8, 9]. It can also cause fatal diseases including kidney and respiratory defects, Minamata disease, acrodynia, hypotonia, hypertension, irregular digestion with damaging the nervous and gastrointestinal system, and immune system. There are many regulations to stop excess exposure to mercury. However, mercury is still originated by natural,

Table 1.1 Sources, effects, and permissible limits of a variety of heavy metals in drinking water [1, 10-16].

Heavy metals	Sources	Effects	Permissible limits (mg/L)	
			WHO	EPA
Mercury (Hg)	Pesticides, energy storage, paper manufacturing, coal combustion, power plants, and volcanic emissions	arrhythmia, cardiomyopathy, kidney and respiratory failure, pulmonary edema, nephrotic syndrome, nervous and gastrointestinal system defects, damaged immune system	0.001	0.002
Lead (Pb)	Tobacco, emission from vehicle, PVC pipes in sanitation, pesticide, paints, jewelry, mining, lead batteries, lunch boxes, burning of coal	Central nervous defects particularly for kids, encephalopathy for infants, kidney failure, gastrointestinal disorders, Alzheimer's disease	0.05	0.01

Heavy metals	Sources	Effects	Permissible limits (mg/L)	
			WHO	EPA
Cadmium (Cd)	Fertilizers, pesticides, paints and lubricants, electroplating for ornaments, cadmium and nickel batteries, solar cells, nuclear power plants	kidney dysfunction, hypertension, fatigue, lung cancer, acute bronchitis, fatal pulmonary fibrosis,	0.005	0.005
Arsenic (Ar)	Fertilizers, agricultural pesticides, Wooden poles, fungicides, mining, geological systems	central nervous system defects, hyperpigmentation, skin cancer, gastrointestinal diseases, pulmonary diseases	0.05	0.01
Copper (Cu)	Solar cells, pesticides, fertilizers, tannery waste, chemical waste	Arthritis, skin allergies, kidney and liver dysfunction, lungs and digestive defects, fatigue, liver and kidney damage, diabetes	1.3	1.3

Heavy metals	Sources	Effects	Permissible limits (mg/L)	
			WHO	EPA
Silver (Ag)	Electroplating parts, refinery industries, jewelry refining	Alzheimer's disease, fatigue, rheumatoid arthritis, cytopathologic effects, local argyria	0.1	0.1
Chromium (Cr)	Mining, dying industry, leathers, electroplating, minerals	Lung cancer, dermatitis, dysfunction of the nervous system, mental fatigues, irritation, skin ulcers	0.05	0.1
Zinc (Zn)	Chemical refineries, electroplating, welding, electric soldering, brass industry, pigments	Bronchitis, respiratory failure, skin diseases, prostate cancer, nervous disorders	5	5

domestic, and industrial sources such as pesticides, energy storage, mining, coal combustion, power plants, thermometers, cosmetics, volcanic emissions, etc. Consequently, the water and air of the environment have been contaminated with mercury which in turn enters our body through drinking water, fishes, vegetables, fruits, etc. The

WHO and the EPA have defined guideline values of mercury in drinking water as 0.001 mg/L (5 nanomolar, nM) and 0.002 mg/L (10 nM), respectively [17].

Lead is another important heavy metal contaminant that has adverse effects on human health and environment species. The leaching of lead from PVC pipes can significantly contaminate drinking water and tap water. Another major source of lead is lead soldered and chrome-plated domestic fixtures which are mixed with water due to corrosion. The exposure of trace levels of lead can cause fatal disorders in the human brain, immune systems, neural systems particularly for kids and youths [18-20]. The WHO and EPA recommended the value of lead in drinking water is 0.05 mg/L and 0.01 mg/L, respectively [10].

Cadmium is another heavy metal element and causes a sudden loss of kidney function, hypertension, fatigue, lung cancer, bone marrow cancer, acute bronchitis, gastrointestinal diseases, fatal pulmonary fibrosis, osteoporosis, etc. Major sources of cadmium pollution are fertilizers and pesticides in agriculture, paints, lubricants, photography, electrical welding, electroplating for ornaments, batteries, solar cells, nuclear power plants, etc. A 0.005 mg/L of cadmium in drinking water is allowed [11]. The contamination of arsenic in drinking water has negative effects on the human body such as the central nervous system, hyperpigmentation, skin cancer, gastrointestinal diseases, pulmonary diseases, dermatologic effects, brain edema, lung edema, atopic dermatitis, etc. A maximum concentration of 0.05 mg/L and 0.01 mg/L is allowed for arsenic contaminants in drinking water [12].

Major sources of copper are solar cells, pesticides, fertilizers, tannery waste, chemical waste, metal pipes, etc. The uptake of toxic copper can cause arthritis, skin allergies, kidney and liver dysfunction, defects in lungs and digestive system, A 1.3 mg/L concentration of copper in drinking water is the maximum allowed limit recommended by environmental agencies [13]. Electroplating parts, refinery industries, and jewelry refining are the major sources of silver and it can cause Alzheimer's disease, fatigue, rheumatoid arthritis, etc. A maximum concentration of 0.1 mg/L is allowed for silver contaminants in drinking [13].

Chromium is usually found in the mining, dying industry, leathers, welding of stainless steel, etc., and it can produce lung cancer, dermatitis, dysfunction of the nervous system, and mental fatigue. The safety level of Cr in drinking water is 0.05 mg/L and 0.1 mg/L, respectively [14]. A trace amount of zinc can cause bronchitis, respiratory failure, skin diseases, prostate cancer, nervous disorders. It is usually found in the chemical refineries, electroplating, welding, electric soldering, brass industry, and pigments. The WHO and EPA guideline value of zinc in water is 5 mg/L [15].

1.1.2 Conventional Techniques and Sensors for the Detection of Heavy Metals

Water is essential for human and animal lives, plants, chemical and food industries, and energy production. Heavy metals in water such as Hg, Pb, Cd, As, Cr, etc., can pollute the groundwater and drinking water. A variety of conventional techniques have been developed for the detection of these heavy metals including colorimetry [21, 22], Atomic Absorption Spectrometry (AAS) [23], fluorescence spectroscopy [24], UV-vis spectrometry [25], and Inductively Coupled Plasma Mass Spectrometry (ICP-MS) [26].

AAS utilizes the absorption of light for the quantitative detection of target metal elements. Light is absorbed by free metal atoms in solution or gaseous phase which can quantify the concentration of 70 different metal elements used in electrochemistry, biology, and pharmacology research [23]. ICP-MS is another technique where the sample is ionized by plasma followed by detection and quantification with a mass spectrometer. It has higher sensitivity and accuracy than AAS. [27]. Colorimetry is another absorption technique for the detection of target analytes using Beer-Lambert law. Gulsu and coworkers used mercaptoundecanoic acid-capped gold nanoparticles (AuNPs) and amino acids for the detection of multiple heavy metals. Due to the complex formation ability with metal ions, amino acid and AuNPs showed significant colorimetric response with excellent selectivity toward Hg^{2+}, Cd^{2+}, Fe^{3+}, Pb^{2+}, Al^{3+}, Cu^{2+}, and Cr^{3+} [28]. The fluorescence sensor is another powerful tool for sensitive and selective detection of toxic heavy metals. Wang et al. demonstrated amino acid-derived carbon dots for fluorescent detection of multiple heavy metal ions [29]. These functionalized carbon dots showed excellent fluorescence quenching response toward Hg^{2+}, Cu^{2+}, Fe^{3+} with high sensitivity and selectivity. Moreover, surface-enhanced Raman spectrometry [30], ion chromatography [31], and inductively coupled plasma optical emission spectrometry [32] are also utilized for the detection of heavy metals. Although these traditional techniques have enabled efficient detection of heavy metals, they are expensive, bulky, complex to operate, and inconvenient for on-site testing [33, 34]. In contrast, electrochemical methods have received significant attention from worldwide researchers for the determination of heavy metals in water due to simplicity, cost-effectiveness, excellent sensitivity, a low Limit of Detection (LOD), and on-site analysis [6, 35, 36]. Anodic stripping voltammetry (ASV) is a promising

electrochemical technique for trace level detection of toxic heavy metal ions owing to excellent sensitivity, simplicity, low detection limit, and the ability for simultaneous detection.

ASV is a two-step technique consisting of deposition (accumulation) and stripping (oxidation). In the first step, the metal ion is deposited on the electrode surface using a constant potential, and then subsequently, stripping is performed which gives a current signal in the output to quantify the concentration of metal ions. The concentration of metal ions is proportional to the intensity of the current signal (height of the peak current). This accumulation of metal ions before stripping gives a low detection limit of an electrochemical sensor. When the stripping is done with a square wave then it is known as square wave anodic stripping voltammetry (SWASV). Similarly, differential pulse anodic stripping voltammetry (DPASV) and linear sweep anodic stripping voltammetry (LSASV) is obtained. Among them, SWASV is the most sensitive and effective technique to detect heavy metal ions [37-39].

1.1.3 Two Dimensional Nanomaterials: Structure and Properties

1.1.3.1 Graphene and Graphene Oxide

Two-dimensional (2D) nanomaterials consist of thin layers with a thickness of one atomic layer. In 2D nanomaterials, two dimensions are at the macroscale and one dimension is at the nanoscale (1 nm to 100 nm). 2D nanomaterials possess a high surface to volume ratio (aspect ratio) compared to bulk materials, which leads to unique properties with widespread applications [40]. 2D nanomaterials include such materials as graphene,

phosphorene, black phosphorous, hexagonal boron nitride, and transition metal dichalcogenides.

Graphene is a widely recognized 2D material composed of a single layer of covalently bonded sp^2-hybridized carbon atoms in a hexagonal crystal structure (Figure 1.1 a) [41-43]. Graphene, graphite, carbon nanotubes (CNTs), and fullerenes are considered allotropes of carbon [44]. A spacing of about 1.42 Å exists between two neighboring carbon atoms in a single graphene sheet and each layer is stacked together with a van der Waals interaction with a spacing of about 3.35 Å (Figure 1.1b). Geim and Novoselov first successfully produced graphene through mechanical exfoliation in 2004 and they were awarded Nobel Prize in Physics (2010). Since then, research has focused on graphene because of its unique electrical, optical, chemical, mechanical, and thermal properties [45-47]. Graphene shows a large surface area (2,600 $m^2 g^{-1}$), high electrical conductivity (3,189 S cm^{-1}), high electron mobility (200,000 $cm^2 V^{-1} s^{-1}$), good thermal conductivity (≈ 4,000 W $m^{-1} K^{-1}$), and high mechanical strength with a tensile strength of 130.5 GPa and Young's modulus of 1 TPa [48-52]. These unique properties have made graphene as promising for biosensors, electronic sensors, gas sensors, and electrochemical heavy metal ion sensors [53, 54]. For example, a large surface area with high conductivity of graphene sheets can facilitate to adsorb a high density of analytes which consequently improves the sensitivity and downscaling of devices [55].

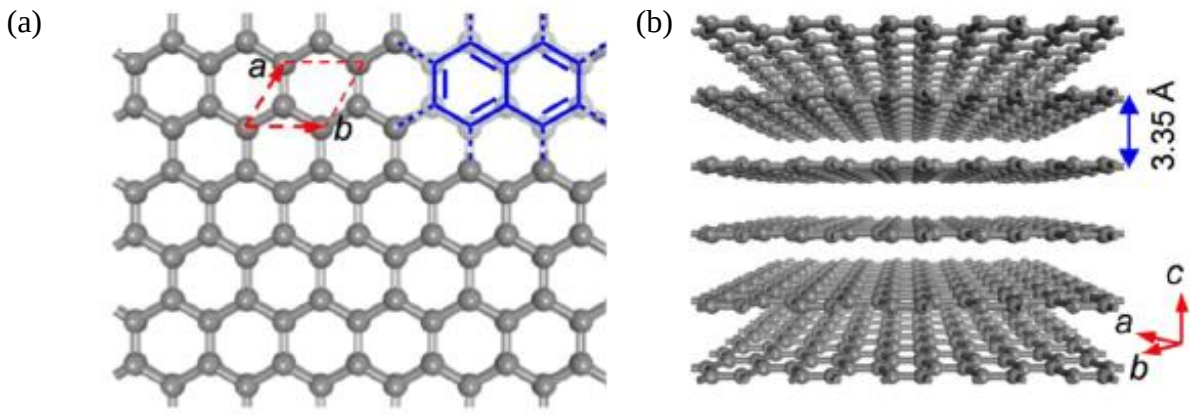

Figure 1.1 (a) Ideal structure of a sheet of graphene that consists of an atomic-scale hexagonal lattice made of carbon atoms (b) Structure of graphene layers [41].

Graphene oxide (GO) is considered a precursor for the large-scale synthesis of graphene through solution-phase exfoliation, chemical, or thermal treatments [56]. GO has a graphene-like layered structure with abundant oxygen-containing functional groups on its surface including carboxyl (-COOH) and carbonyl (C=O) group at the edges and hydroxyl (-OH) and epoxy (C-O-C) on the basal plane, which makes it electrically insulating (Figure 1.2a) [55, 57-59]. The thickness of the single-layer GO measured by atomic force microscopy (AFM) is about 1 nm (Figure 1.2b). The presence of these oxygen-containing functional groups in GO can cause significant structural and compositional defects which in turn reduces the electrical conductivity and limit its application in electrical devices. However, these oxygen-containing groups can make GO promising for many other applications. For example, different oxygen functional groups in GO will facilitate the hydrophilicity and good dispersibility in many solvents including water. A thin film of GO can be prepared by drop-casting or spin coating of a stable GO dispersion. Besides use as excellent electrode materials, the functional groups in GO can

immobilize certain analytes due to electrostatic interactions which in turn increase the sensitivity and selectivity of the developed sensor devices. Further, large surface area and excellent electrocatalytic activities of GO improves the sensitivity of the GO-based sensors [60].

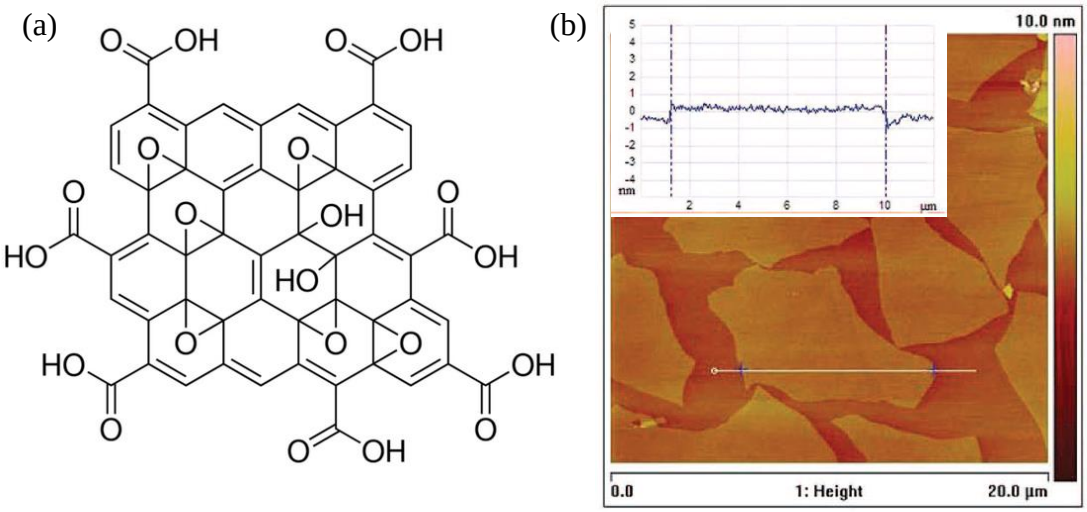

Figure 1.2 (a) Structural model of a single layer of graphite oxide [61] (b) AFM images showing a close-packed graphite oxide monolayer on silicon wafer [62].

1.1.3.2 Transition Metal Dichalcogenides

The rapid progress in the field of graphene research over the past few years has inspired researchers to explore other 2D materials [63, 64]. Single-layer Transition Metal Dichalcogenides (TMDs) are considered analogous to graphene for their intriguing properties [65, 66]. TMDs are the layered structure of inorganic materials with a chemical formula of MX_2 where M is transition metal atom (Mo, W, Ti, Zr, Hf, etc.) and X is a chalcogen (S, Se or Te) (Figure 1.3).

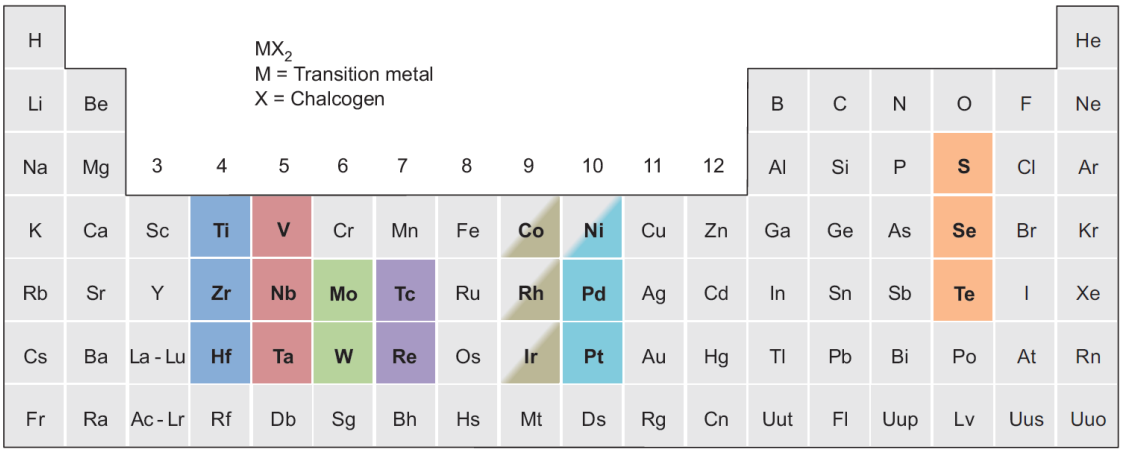

Figure 1.3 Structure of TMDs materials (a) About 40 different layered TMD compounds exist [67]

The transitional metals in the group of IV-VII present layered structures while VII-X has non-layered structures. For example, a layer of metal atoms (M) is sandwiched between two layers of chalcogen (X) atoms in a monolayer of MX_2, where a weak van der Waals interaction lies between stacking monolayers (Figure 1.4a). The stacking of each monolayer gives the thickness in the range of 6-7 Å [68]. The electronic properties depend on the number of layers in TMDs. For example, decreasing the number of layers gives an increased bandgap from about 1.3 eV for bulk MoS_2 to about 1.9 eV for single-layer MoS_2 [69]. Depending on the coordination of metal and chalcogen atoms, TMDs show different polymorphs based on the coordination of metal and chalcogen atoms. For instance, the 2H phase shows a hexagonal symmetry with trigonal prismatic coordination while3R phase has rhombohedral symmetry with trigonal prismatic coordination, and the 1T phase has tetragonal symmetry with octahedral metal coordination (Figure 1.4b) [63, 67]. The number in each phase denotes the number of X-M-X units (i.e. number layers in the stacking sequence) per unit cell. Single layered TMDs show only trigonal prismatic (2H)

and octahedral (1T). The electronic properties of 1T phase TMDs are conducting while that of the 2H phase is semiconducting.

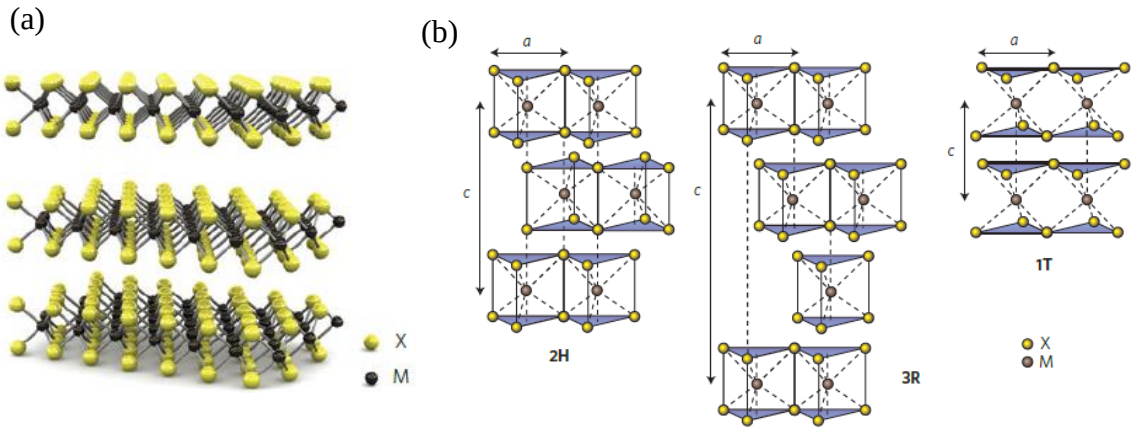

Figure 1.4 (a) Three-dimensional schematic representation of a typical MX_2 structure [70] (b) Schematics of the structural polytypes: 2H (hexagonal symmetry), 3R (rhombohedral symmetry), and 1T (tetragonal symmetry) [63].

It is worthy to note that the transition of crystal phases of TMDs between these phases (from 2H to 1T) can be obtained by a variety of techniques including alkaline metals intercalation (Li, K, or Na), ammonium intercalation, annealing, mechanical exfoliation, solvent exfoliation, and CVD [67]. Zhang prepared single-layer nanosheets of MoS_2 and WS_2 through a simple lithium intercalation method which is shown in Figure 1.5a,b [71, 72]. The thickness of MoS_2 nanosheet and WS_2 nanosheet was found 1 nm which can be observed on the inset of the photographs of their dispersions.

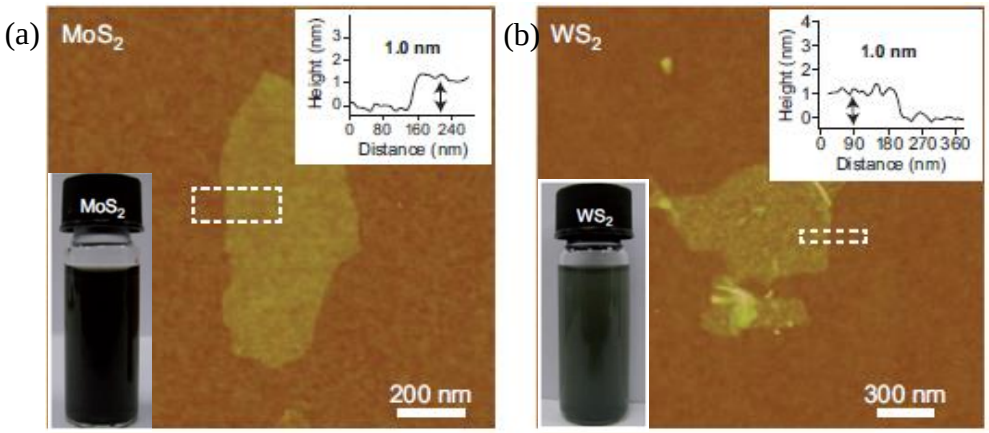

Figure 1.5 Atomic force microscope images of (a) MoS_2 nanosheets (b) WS_2 nanosheets on SiO_2 substrates [71, 72]. The insets of the AFM images represent height profiles from the substrate onto the nanosheets and photographs of MoS_2 nanosheets and WS_2 nanosheets dispersions.

As an emerging TMDs, WS_2 has received significant attraction for gas sensing, electrochemical sensing, energy storage, and supercapacitors due to its high surface area, layered structure, tunable bandgap, excellent electrical conductivity, and fast electron transfer kinetics [73-76]. The chemical and catalytic properties of TMDs mostly depends on the orientation and vacancy of the chalcogen atoms at the edge and basal planes. For example, the vacancy of S atoms at MoS_2 edges enhances the adsorption of gas analytes which results in a superior sensor sensitivity compared to pristine MoS_2 [77]. The electrical conductivity of TMDs also plays an important role in device performance. For example, metallic 1T-WS_2 showed superior performance compared to semiconducting 2H-WS_2 in the field of glucose biosensors [78], electrocatalysts [79], and supercapacitors [80]. Due to the fluorescence quenching properties, TMDs are also promising for the detection of different analytes including nucleic acids, heavy metals, glucose, etc. Because of the

excellent electrical conductivity and presence of abundant sulfur sites, WS_2 is a promising candidate for the detection of heavy metals including Hg^{2+} and Ag^{+} [81] [82].

It is worthwhile to mention that the structural morphology of WS_2 plays a crucial role in superior sensing performance. To date, many strategies including solvothermal [83], lithium-based-intercalation [84], hydrothermal synthesis [85], etc., have been employed to produce various morphologies including nanoribbons [85], nanoflakes [84], nanosheets [79], and nanospheres [86]. Furthermore, the large surface area, structural morphology, excellent chemical stability, and presence of active sites for analytes have made WS_2 a potential electrode material for electrochemical sensors in the field of heavy metal sensing applications.

1.1.4 Silver Nanowires: Properties and Applications

One-dimensional (1D) metallic nanostructures (wires, rods, and tubes) have received significant attention due to their unique electronic, optical, thermal, chemical, and catalytic properties. Silver nanowires (AgNWs) is an example of a 1D-nanostructure with fascinating catalytic, optical, electrical, and chemical properties depending on their size, shape, crystallinity, and structure [87, 88]. Thus, AgNWs is a promising candidate for a variety of applications in the field of chemical sensors, optical devices, and electrocatalysts [89, 90]. In particular, AgNWs are used as an additive to increase the conductivity of the electrode materials by providing conduction pathways for faster electron transfer during chemical sensing and consequently improving the sensitivity and selectivity of the electrochemical sensors [91]. For example, AgNWs have been incorporated in chitosan film for nonenzymatic detection of H_2O_2 [92]. Wang et al. demonstrated an amperometric

sensor based on AgNWs and glucose oxidase (GOD) for sensing glucose with high sensitivity [93]. The resulting sensing performance toward glucose could be ascribed to the high conductivity, excellent catalytic activity, and large surface area of AgNWs. The biomimetic AgNWs templated by peptide nanofibers (PNF-AgNWs)-graphene hybrid modified electrochemical sensor exhibited high sensitivity, specificity, and low detection limit toward H_2O_2 [94]. Due to the excellent flexibility, optical transparency, and mechanical stretchability, AgNWs received tremendous attention from worldwide researchers for developing strain and wearable sensors [95, 96]. For example, Cheng et al, fabricated a strain sensor using 2 nm thin AgNWs and AuNWs through a simple and cost-effective drop-casting process which showed excellent stretchability and optical transparency [95]. Figure 1.6 shows a scanning electron microscopy (SEM) image of AgNWs and its application in display devices, solar panels, electrochemical biosensors, nanophotonic devices, and wearable devices.

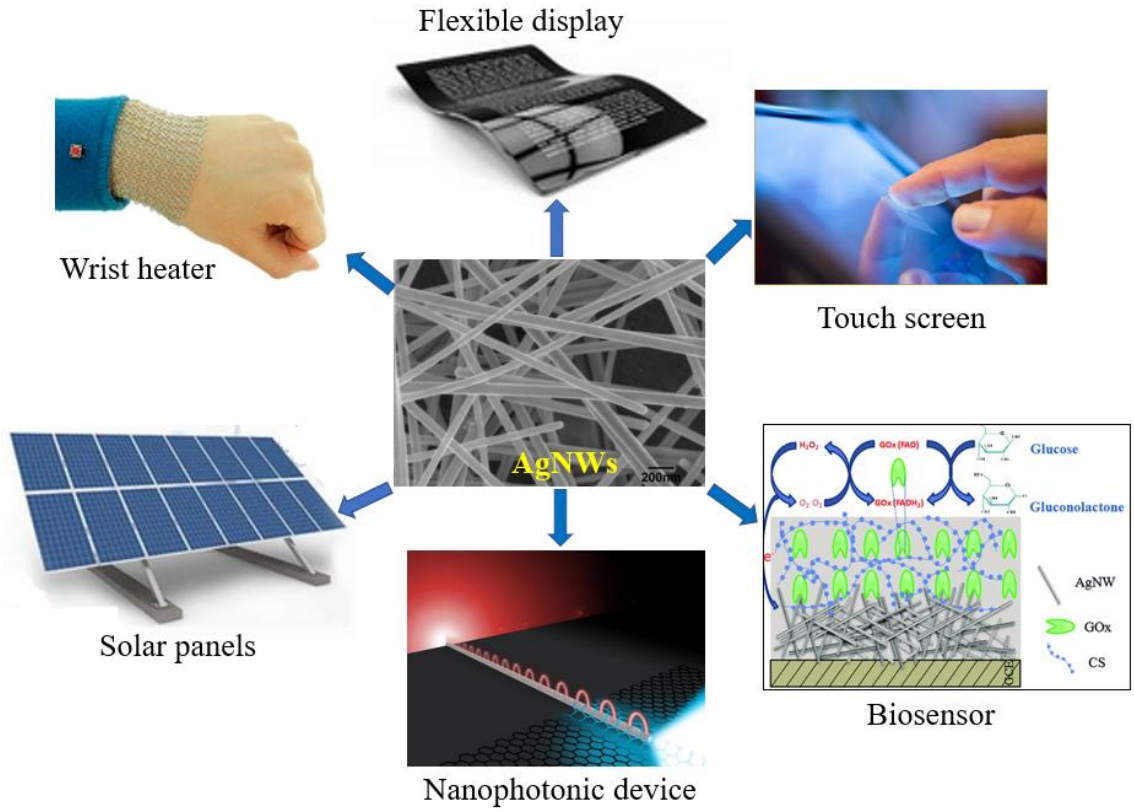

Figure 1.6 Silver nanowires and their application in optical displays, electrochemical biosensors, nanophotonic devices, solar panels, and wearable devices [97-101].

1.2 Previous Work

1.2.1. Graphene, Graphene Oxide, and Composites for the Detection of Heavy Metals

Due to the enhanced surface area, ultrathin nature, layered nanostructures, fast electron transfer kinetics, excellent electrocatalytic activity, and feasibility for functionalization, graphene and GO have become promising electrode materials for sensing [2, 102]. However, van der Waals force and π-π stacking interactions cause agglomeration of graphene sheets in the dispersions of GO [103, 104]. To solve these issues, a variety of strategies have been developed including the incorporation of metal

nanoparticles [105], metal oxide nanoparticles [7], metal nanowires [106-108], nafion [104], chitosan, and conducting polymer [109, 110] into graphene dispersions. These materials form a composite with GO which facilitates high sensitivity, selectivity, and lower detection limits toward chemical sensing by utilizing the synergistic effects of the individual material.

Gong et al. (2010) used chitosan as a stabilizing agent to prevent the agglomeration of graphene sheets in dispersion [105]. They utilized AuNPs-graphene composite for the electrochemical detection of Hg^{2+}. The resulting sensor showed a linear detection range of 0.008-0.05 ppb and 0.1-60 ppb with a detection limit of 6.0 ppt toward Hg^{2+}. Further, it could selectively detect Hg^{2+} even in presence of 20-fold concentrations of Cd^{2+}, Co^{2+}, Cu^{2+}, Fe^{3+}, Zn^{2+}, and I^- in the solution. It also showed the feasibility of the determination of Hg^{2+} in river water with high accuracy. The excellent sensing performance was attributed to the enhanced surface area, good conductivity, and excellent catalytic activities of the AuNP-chitosan-graphene composite [105].

Wei et al. incorporated SnO_2 nanoparticles on reduced Graphene Oxide (rGO) for enhanced detection of heavy metals [7]. The SnO_2/rGO composite modified glassy carbon electrode could detect multiple heavy metal ions including Cd^{2+}, Pb^{2+}, Cu^{2+}, and Hg^{2+} individually and simultaneously. Interestingly, the fabricated sensors showed higher sensitivity toward these heavy metals during simultaneous analysis compared to their individual analysis. The sensor responded linearly toward Cd^{2+}, Pb^{2+}, Cu^{2+}, and Hg^{2+} in the range of 0.3-1.2 μM with a low LOD of 1.0×10^{-10}, 1.8×10^{-10}, 2.3×10^{-10}, and 2.8×10^{-10} M, respectively. An additional stripping peak observed between the Cu^{2+} and Hg^{2+} in the

SWASV response was ascribed to the lack of binding sites and the formation of intermetallic compounds [111, 112].

Ting et al. (2015) developed Graphene Quantum Dots (GQD) functionalized AuNP for the detection of Hg^{2+} and Cu^{2+} in aqueous media [113]. The resulting scaffold could detect Hg^{2+} and Cu^{2+} with a sensitivity of 2.47 μA/nM and 3.69 μA/nM, respectively. In addition to excellent electrochemical stability over a period of one week, it had a very low detection limit of 0.02 nM and 0.05 nM for Hg^{2+} and Cu^{2+}, respectively. They proposed that the electrostatic interaction between Hg^{2+} and carboxyl and hydroxyl groups of GQD could form an R-COO-(Hg^{2+})-OOC-R complex for the selective detection of Hg^{2+}. However, some agglomeration of GQD on AuNP was observed which may have degraded sensor performance.

Zhou et al. (2013) introduced Ionic Liquid (IL) into GO to obtain a homogenous dispersion and the resulting GO-IL-AuNP composite was used for the enhanced sensing of Hg^{2+} in drinking water [114]. Using DPV analysis, a linear detection range of 0.1-100 nM and a detection limit of 0.03 nM toward Hg^{2+}were achieved.

Muralikrishna et al. utilized L-cysteine-rGO composite for simultaneous detection of multiple heavy metals with excellent sensitivity and a wide linear detection range with a detection limit of 0.366, 0.416, 0.261, 1.113 ppb for Cd^{2+}, Pb^{2+}, Cu^{2+}, and Hg^{2+}, respectively [115].

Wang et al. used Thymine (T) functionalized AuNP-rGO nanocomposites for selective detection of Hg^{2+} through the formation of a stable T- Hg^{2+}-T complex [116]. Here, AuNP was immobilized on chemically reduced GO and thymine-1-acetic acid was

incorporated through covalent bonding of amine group of cysteamine. The T/AuNP/rGO modified biosensor showed a linear response in DPV toward Hg^{2+} in the range of 10 ng/L-1.0 μg/L and a detection limit of 1.5 ng/L with an excellent selectivity response against other six metal ions.

Zhang and coworkers developed graphene and nano Au modified electrode with the immobilization of single-stranded DNA probes for ultrasensitive and specific detection of Hg^{2+} at an attomolar (aM) level during SWV analysis. T- Hg^{2+}-T complex enabled the proposed sensor to detect Hg^{2+} at 0.001 aM with a linear detection range of 1.0 aM-100 nM. Moreover, it exhibited excellent selectivity toward Hg^{2+} against 50-fold concentrations of a variety of heavy metals including K^{+}, Ba^{2+}, Ca^{2+}, Cd^{2+}, Co^{2+}, Cr^{2+}, etc [117]. The T-Hg^{2+}-T interactions were also utilized for Hg^{2+} detection in these reports [118]. N-doped rGO and MnO_2 nanocomposite were used as scaffolds for electrochemical detection of Hg^{2+} by SWV and the resulting sensor showed a favorable sensitivity toward Hg^{2+} with a detection limit of 0.0414 nM [119].

Graphene and rGO have been widely applied as a conducting channel material in field-effect transistor (FET) devices to investigate the real-time detection of various heavy metal ions. FET-based sensors work on the change of conductivity or mobility of the graphene channel under the absorption of metal ions via electrostatic interactions. For selective detection of metal ions, the surface of graphene is modified with a receptor for target meta ion through covalent or non-covalent binding [120]. Zhang et al. used 1-octadecanethiol functionalized graphene as a channel on a FET device for the detection of Hg^{2+}. The resulting sensor showed a detection limit down to 10 ppm [121]. Later, Sudibya et al. used metallothionein type II protein for metal ion bonding which required complex

fabrication and the resulting sensor suffered from chemical stability and repeatability concerns [122]. To address these issues, Chen et al. introduced AuNP and Thio Glycolic Acid (TGA) functionalized rGO (rGO/TGA-AuNP) composite. The resulting FET device could detect Hg^{2+} in the range of 2.5×10^{-8}-1.42×10^{-5} M due to a change of conductivity [120]. A quick dynamic response was observed within a few seconds upon the addition of Hg^{2+} on sensor surface which demonstrates its real time applicability. The rGO/TGA-AuNP hybrid sensor showed negligible response against five interfering ions, which confirms its excellent specificity toward Hg^{2+}.

In addition to electrochemical methods, a variety of other techniques including Surface Plasmon Resonance (SPR), UV-Visible absorption spectroscopy, colorimetry, etc., are extensively used for the analysis of heavy metals [82, 123-128]. Kamaruddin et al. proposed a hybrid of gold/silver/gold/chitosan-GO (Au/Ag/Au/CS-GO) for the efficient detection of Pb^{2+} and Hg^{2+} in water using SPR [128]. A linear sensor response was observed for Pb^{2+} and Hg^{2+} in the range of 0.5-25 µM, which is far from the guidelines recommended by the WHO. Also, their developed sensor lacks the analysis of real samples such as drinking water. Further, Golsheikh et al. demonstrated a rGO-silver nanoparticles (AgNPs) composite for the optical detection of Hg^{2+} using UV-Visible absorption spectroscopy [126]. The obtained linear detection range for Hg^{2+} was 0.1 µM-100 µM with a detection limit of 20 nM. The sensor was not tested to detect Hg^{2+} in water samples.

In summary, GO has been utilized for the development of an electrochemical sensor for the detection of Hg^{2+} in water and environmental samples with ultra-high sensitivity, excellent selectivity, and ultra-low detection limit. Furthermore, the incorporation of metal

nanowires such as AgNWs can form GO composites to enhance the sensitivity and lower the detection limit toward Hg^{2+} by utilizing the advantages of AgNWs and GO.

1.2.2. Transition Metal Dichalcogenides and Composites for the Detection of Heavy Metals

Jiang et al. first reported (2015) a few-layer MoS_2 based field-effect transistor for the detection of Hg^{2+} in an aqueous environment [129]. The effect of Hg^{2+} ions on charge transport and photoluminescence properties of ultrathin MoS_2 was investigated. The strong binding affinity of Hg^{2+} toward sulfur with a stability constant of 2.5×10^{52} can effectively bind Hg^{2+} with MoS_2 by the partial electron transfer from MoS_2 to Hg^{2+}, which eventually produces a p-type doping effect in n-type MoS_2. Thus, the conductivity and photoluminescence in MoS_2 can be modulated with the addition of Hg^{2+}. The resulting MoS_2 based FET sensor showed a decrease of conductivity in a few-layer MoS_2 with increasing the concentration of Hg^{2+} in the range of 0-1 µM. The sensor showed an ultralow detection limit of 30 pM with excellent selectivity and specificity over 15 potential interfering ions, which demonstrate a promising device for Hg^{2+} detection in water samples.

Zhou et al. developed a MoS_2 nanosheets-AuNPs-DNA functionalized hybrid FET device on Si/SiO_2 for real-time detection of Hg^{2+} in water [130]. The AuNPs decorated on the MoS_2 surface will immobilize the Hg^{2+} specific DNA by gold-thiol interaction. The formation of the thymine-Hg^{2+}-thymine complex made the sensor highly selective toward Hg^{2+} against other ions. The binding of positively charged Hg^{2+} with DNA leads to an increased hole concentration in the MoS_2 sensing material by causing an electron transfer from MoS_2 to AuNPs. Thus, the conductivity of the p-type MoS_2 channel increased under

the exposure of Hg^{2+} ions. A response time of 1-2 s and ultra-trace detection limit of 0.1 nM were obtained using DNA-AuNPs functionalized MoS_2 hybrid FETs.

Nigam et al. utilized hydrothermally synthesized flower-like MoS_2 for real-time detection of a trace amount of Hg^{2+} in water [131]. Here, the gate region of an AlGaN/GaN HEMT was functionalized with vertically aligned MoS_2 and the change in drain to source current under the exposure of $Hg^{2+}$was monitored in real-time. The formation of the Hg^{2+}-S complex and the electrostatic interaction between MoS_2 and Hg^{2+} made enhanced sensor response. The sensor showed an interesting phenomenon of an initially increasing and then decreasing drain current properties with the increase of Hg^{2+} concentrations. A linear detection range of 0.1 ppb-1000 ppb with an excellent sensitivity of 0.64 μA/ppb and a low detection limit of 0.01152 ppb and a response time of 1.8 s toward Hg^{2+} were achieved.

Aswathi et al. utilized solvent exfoliated MoS_2 sheets for the electrochemical detection of Hg^{2+} in normal water and seawater [81]. A homogenous dispersion of MoS_2 was drop-cast on a glassy carbon electrode and dried at room temperature under air. Since Hg^{2+} acts as a strong oxidizer and S^{2-} acts as a natural reducer, a spontaneous reduction of Hg^{2+} occurred on the MoS_2 by forming Hg-S covalent bonds at room temperature without any preconcentration or accumulation steps. Consequently, an ultra-low detection limit of 0.000001 nM (0.2 ppq) toward Hg^{2+} was achieved with a wide linear detection range of 0.1 nM-0.2 mM. Further, it showed excellent specificity toward Hg^{2+}in presence of ten different metal ions, which can be attributed to the higher standard reduction potential of Hg^{2+} (+ 0.85 V) than other ions.

Li et al. demonstrated a one-pot technique for solvothermal synthesized flower-like WSe_2 and WS_2 as effective adsorbents of Pb^{2+} and Hg^{2+}. Due to the nanosheet structure and the presence of abundant chalcogen ligands, WSe_2, and WS_2 showed an excellent uptake capacity for soft metal including Pb^{2+} and Hg^{2+} from water [132].

In addition, the semiconducting properties of WS_2 have been utilized for the fluorescent detection of heavy metals. Zuo et al. developed a dual-color biosensor by utilizing the fluorescent quenching properties of 2H-WS_2 nanosheets and Hg^{2+} and Ag^{+} specific DNA probes [82]. Those mixture emitted green and red fluorescence signals at 525 nm and 583 nm for Hg^{2+} and Ag^{+}, respectively. The resulting sensor showed a linear response for Hg^{2+} and Ag^{+} in the range of 6.0-650.0 nM and 5.0-1000.0nM, respectively. Furthermore, a low detection limit of 3.3 nM and 1.2n M were calculated for Hg^{2+} and Ag^{+}, respectively. A 10-fold higher concentration of interference metal ions including Co^{2+}, Cu^{2+}, Cd^{2+}, Pb^{2+}, Mn^{2+}, Ni^{2+}, Cr^{2+}, Fe^{3+}, Ca^{2+}, Zn^{2+}, K^{+}, and Ba^{2+} were tested to find the selectivity of the sensor. No significant fluorescence was observed except for Hg^{2+} and Ag^{+} which demonstrates the excellent specificity of the biosensor. Ge et al. demonstrated a simple and highly sensitive biosensor for Hg^{2+} determination using the synergistic effect of T7 exonuclease assisted cyclic signal amplification and the fluorescence quenching ability of few-layer 2H-WS_2 nanosheets [127]. Under optimum experimental conditions, the resulting sensor showed a linear increase of fluorescence intensity with increasing Hg^{2+} concentrations from 0.5 nM-20 nM with a detection limit of 0.1 nM. In addition to excellent selectivity, the sensor also successfully determined the concentrations of Hg^{2+} spiked in tap water and lake water samples with high accuracy. However, owing to the limited fluorescence quenching ability of 2H-WS_2, these sensors suffer from narrow LDRs and

high LODs. Li et al. prepared nitrogen-doped WS_2 through ultrasonic agitation of a mixture of bulk WS_2 and melamine followed by calcination at 400℃ for 4 h under a nitrogen atmosphere [133]. A linear increase of fluorescence intensity with the growth of Hg^{2+} concentrations in the range of 0.1-5 μM with a detection limit of 20 nM was found. On the other hand, only a few works have explored the application of metallic 1T-WS_2 for glucose biosensors [78], electrocatalysts [79], and supercapacitors [80]. As far as we are aware, there have been no reported works on electrochemical detection of Hg^{2+} using metallic 1T-WS_2.

This work is the first report on the electrochemical detection of Hg^{2+} using metallic 1T-WS_2 microflowers. The flower-like WS_2 microstructure provides a high electroactive surface area for enhanced loading and rapid diffusion opportunity for Hg^{2+} ions. The metallic phase of 1T-WS_2 enhances the electrochemical properties by providing a fast-heterogeneous electron transfer (HET) rate. Moreover, the presence of abundant active sites on both edge and basal planes of the 1T-WS_2 will further improve the electrocatalytic performances [134, 135]. Owing to the high electroactive surface area, good conductivity, fast heterogeneous electron transfer rate, and abundant active sites, the exploitation of 1T-WS_2 microflowers for electrochemical sensing of Hg^{2+} leads to wide linear detection ranges with excellent sensitivity and selectivity.

1.3 Motivation

2D-nanomaterials and their composites for electrochemical detection of Hg^{2+} with excellent sensitivity, wide LDR, ultra-low LOD, and high selectivity would prevent the consumption of unsafe drinking water.

1.4 Objectives

The objective of this work is to develop an electrochemical sensor based on 2D-nanomaterials and their composites for the detection of Hg^{2+} in aqueous media with excellent sensitivity, wide linear detection range (1 nM-1 mM), ultra-low detection limit (down to nM or pM level) and high selectivity. The following tasks were performed to achieve the goal.

1. Preparation of GO-AgNWs composite using a simple solution mixing process and synthesis of microflower shaped metallic 1T-WS_2 using a facile hydrothermal method and propose a formation mechanism of microflower-like metallic 1T-WS_2.

2. Confirm the structural and morphological characteristics of GO, AgNWs, GO-AgNWs composite, and 1T-WS_2 microflowers using X-ray diffraction, Raman spectroscopy, scanning electron microscopy, and transmission electron microscopy.

3. Fabricate the GO-AgNWs composite and 1T-WS_2 modified glassy carbon electrode sensors using drop-casting and electrochemical characterization of the developed sensors using cyclic voltammetry and electrochemical impedance spectroscopy.

4. Optimize the experimental conditions including deposition potential, deposition time, concentrations of sensing materials, and pH of electrolyte buffer solution to find ultra-trace sensitivity and wide linear detection range of the sensors toward Hg^{2+}.

5. Study the analytical performance of the developed sensors by recording square wave anodic stripping voltammetry response toward different concentrations of Hg^{2+} under optimum experimental conditions.

6. Test the selectivity of the proposed sensors against a variety of interfering heavy metal ions including Cu^{2+}, Fe^{3+}, Ni^{2+}, Pb^{2+}, Cr^{3+}, K^{+}, Na^{+}, Ag^{+}, Sn^{2+}, and Cd^{2+}.

7. Investigate the repeatability, reproducibility, and stability of the developed sensors and determine the feasibility of the sensors by detecting Hg^{2+} in real samples including tap water using the standard addition method.

8. Propose a sensing mechanism of the developed sensors toward Hg^{2+}.

1.5 Organization of the Dissertation

Chapter 1 describes the sources and effects of different heavy metals on public health and the environment. A variety of conventional methods to detect heavy metals have been discussed briefly. A comprehensive review of electrochemical sensors for heavy metal ion detection with advantages and limitations was also presented. The structure and properties of 2D materials including graphene, GO, and TMDs including MoS_2, WS_2, etc., have been discussed. Further, the previous work on graphene, GO, MoS_2, WS_2, and their composites for heavy metal detection and their limitations have been addressed. Finally, the motivation and objectives of this work have been presented.

Chapter 2 describes the electrochemical sensors with the working principle. The sensing mechanism, method of analysis, and performance parameters have been presented. A variety of electrochemical characterization techniques and structural and morphological characterization techniques are briefly described.

Chapter 3 discusses details of experimental procedures for the preparation of precursor materials, hydrothermal synthesis of 1T-WS_2 microflowers, structural and

morphological characterization, sensor fabrication, and procedures for electrochemical measurements.

Chapter 4 includes the results and discussions of the structural morphological characteristics of GO, AgNWs, GO-AgNWs composite, and 1T-WS_2 microflowers. The electrochemical characterization and optimization of experimental conditions are discussed. Analytical performance of the developed sensors toward Hg^{2+} with obtained selectivity, repeatability, reproducibility, and stability are discussed in detail. The practicability of the sensors has been tested by real sample analysis. A detailed comparison of the sensing performance among developed sensors and previously reported sensors has been completed.

Chapter 5 is a summary of this work with specific conclusions and future work.

CHAPTER 2 THEORY

2.1 Electrochemistry

The branch of chemistry that studies the electrical and chemical phenomenon is called electrochemistry. It discusses the chemical phenomenon that occurs by electric current and electrical phenomena like the generation of electrical current caused by chemical reactions [136]. Generally, electrochemistry studies the different fields of electrochemical phenomenon (like electrophoresis and corrosion), electrochemical devices such as electrochemical sensors, energy storage devices, batteries, supercapacitors, fuel cells, and electrochemical technologies [136]. Scientists may want to know the kinetics of a chemical reaction for the analysis of reaction rates of a chemical species or to detect a trace amount of target metal ions or organic analytes in aqueous solutions. These studies need to employ electrochemical tools and electrochemical methods. The researcher may also have an interest in the understanding of electrochemical properties of chemical reactions on the electrode and the electrical characteristics on electrode-electrolyte interfaces.

2.2 Electrochemical Sensors, Types, Advantages, and Principle of Operation

Sensors that convert the signal from electrochemical phenomenon (oxidation or reaction between an electrode and target ions) into a measurable signal are known as electrochemical sensors. Electrochemical sensors usually include three types such as potentiometric, amperometric or voltammetric, and impedimetric. Potentiometric sensors deal with the change in voltage with changing the analyte concentration, while amperometric sensors deal with a change in current with the concentration of analytes via

oxidation and reduction reaction of analytes. Voltammetry techniques include cyclic voltammetry, differential pulse voltammetry, square wave voltammetry, chronoamperometry, etc. Impedimetric sensors measure the change in impedance due to the adsorption of analytes on the electrode surface.

As an essential part of analytical chemistry, electrochemical sensors have received significant attention from worldwide researchers due to their low cost, excellent sensitivity toward target analytes, low detection limit, and faster response [6, 35, 36]. In addition, these sensors do not require trained personal or the knowledge of electrochemistry due to simple operation and procedures. Because of the portability, small size, and lightweight, electrochemical sensors are promising for on-site detection of environmental contaminants [6, 35]. A variety of functional materials and fabrication techniques are considered based on the application of the sensors. The interest in using different nanomaterials for electrochemical sensors to achieve high sensitivity and specificity has been dramatically increasing [137].

The principle of operation of electrochemical sensors is based on the reaction of an analyte with a sensing material to generate either a current or voltage signal which is proportional to the concentration of the target analyte. These sensors can further interpret the electronic output into a digital format for user convenience which has been illustrated in Figure 2.1. There are three main steps involved in the operation of an electrochemical sensor: analyte adsorption, transduction, and signal processing. The analyte is first adsorbed on the sensor surface through a recognition element and then oxidized or reduced through the interaction between the analyte and sensing element and produced an analytical signal. Then the produced analytical signal is transduced by a transducer to an electronic

circuit in terms of current or voltage signal. A strong interaction between sensing elements and analytes results in an excellent sensing performance such as high sensitivity, selectivity, etc. The electrochemical sensors work based on the charge transfer between the electrode-electrolyte interface. When a constant or variable potential is applied through an electrochemical cell, an overpotential is formed due to the difference between applied potential and cell equilibrium potential. Due to this overpotential, electron transfer kinetics become favorable and chemical reactions like oxidation-reduction take place, which is known as the Faradic process. The faradic current can be expressed by (2.1).

$$i = nFAj \qquad (2.1)$$

where i is faradic current, n is electrons transferred during a redox reaction, F is Faraday constant, A is the area of the electrode, and j is the flux of electroactive analytes at electrode-electrolyte interfaces. The flux of electroactive analytes j demonstrates the rate of reaction which is determined as follows.

$$j = k_0 C_o \qquad (2.2)$$

Where k_0 is defined as heterogeneous electron transfer rate constant which demonstrates the electron transfer kinetics and C_o is the concentration of an analyte. The current signal is correlated to the concentration of analytes.

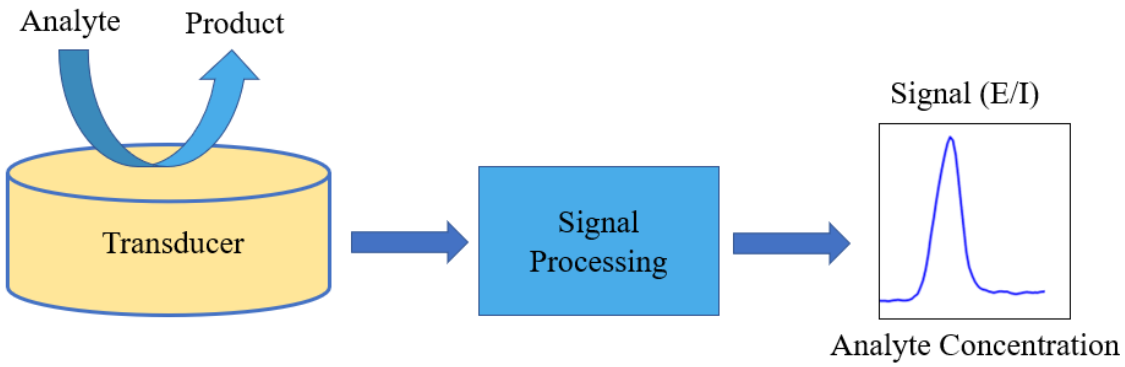

Figure 2.1 Schematic of the steps involved in the operation of an electrochemical sensor.

2.3 Sensor Parameters

2.3.1 Sensitivity

Sensitivity is the ratio of change of output signal to the change of input signal and an important performance parameter of a sensor. Sensitivity is also defined as the slope of the response curve (output signal vs input signal) of a sensor [138, 139]. For example, in the case of electrochemical sensors, sensitivity is the slope of the curve of current vs analyte concentrations. The high sensitivity to analytes in 2D materials-based sensors is attributed to the large surface area and available recognition sites for analyte-active sites interaction. A variety of strategies are employed to enhance the sensitivity including the addition of recognition elements that effectively bind the target analytes [140].

2.3.2 Limit of Detection

Another important parameter of sensor performance is the limit of detection (LOD) or detection limit. It is the smallest concentrations of analyte that can be measured by the sensor and it is easily distinguishable from the baseline signal or blank sample [141, 142].

Blank sample means an absence of analyte in the solution. LOD can be determined by two methods. One is experimental LOD and another one is calculated LOD. Experimental LOD is obtained from the measured sensor response for the lowest known concentrations of the analyte. The calculated LOD is calculated using LOD = 3σ/s, where σ is the standard deviation of blank sample i.e. absence of analyte on sample and s is the sensitivity. Sensitivity (s) is obtained from the slope of the response curve (sensor response vs concentrations of the analyte). Since the LOD is related to sensitivity, a higher sensitivity lowers the LOD. The conductivity of electrode materials, complete coverage of electrode materials, abundant active sites, large available surface area, and strong interaction between analyte-material can improve the sensitivity as well as LOD [143].

2.3.3 Linear Detection Range

A detection range means the range of concentrations of analyte that corresponds to the maximum measurable concentration and the lowest measurable concentration (LOD) by a sensor [144]. A wide range of detection is desired to meet the sensing requirement. Linear Detection Range (LDR) is the detection range where sensor response is linear over a range of concentration of an analyte. LDR is the part of a fitted response curve where the detection range is linear with a correlation coefficient, $R^2 \geq 0.95$ [140]. A wide LDR is desired to calibrate a sensor and satisfy the sensing requirements. A wide LDR is important to assess the range of concentrations where a sensor can work reliably and obtain results precisely and accurately. In contrast, higher-order equations or mathematical manipulations are needed for a non-linear sensor to establish a relationship between analyte concentration and response. If an output data fall outside the detection range, large inaccuracies in the measured data or sensor damage can occur. A wide LDR can be

obtained by considering the suitable electrode materials, the analyte-material interactions, and available surface area [140].

2.3.4 Selectivity

Selectivity is the ability of a sensor to discriminate the target analytes against a variety of potential interferents without any interference [139]. It is also known as specificity. The intensity of the analytical signals obtained from the target analytes is compared with that of the interferents to examine the selectivity of an analytical device. Moreover, the use of recognition elements on an analytical device can selectivity detect the target analytes over possible interferents. Further, the manipulation of experimental conditions such as temperature and pressure can be useful to improve the selectivity of an analytical device [140]. High selectivity in a mixture of various analytes is always desired for sensors.

2.3.5 Stability

Stability is defined as the ability of a sensor to produce the same output for the same analyte concentration over a length of time. The stability of a sensor can be realized by comparing the sensor response measured by a sensor for a prolonged period [141]. The stability of a device is important for continuous and routine measurement of environmental samples. It is desired for a sensor to be unaffected under extreme chemical environmental, mechanical, or physical stress [140].

2.3.6 Repeatability

The ability of a sensor to produce the same output toward the same analytes for a couple of consecutive measurements under the same measurement conditions is known as repeatability[145]. Repeatability measures the precision of a sensor. Repeatability is usually quantified by measuring relative standard deviation (RSD) of multiple measurements with a sensor. A low RSD confirms the good repeatability of a sensor.

2.3.7 Reproducibility

The reproducibility of a sensor is defined is the ability to produce the same output signals under different measurement conditions [145]. It may be the ability of multiple sensors fabricated with the same procedures to produce the same output for an analyte. Repeatability also measures the precision of a sensor It is also quantified by calculating RSD of measured output signals using multiple sensors. A low RSD confirms the good reproducibility of a sensor.

2.3.8 Recovery

The recovery is the ratio of the measured concentration to the added concentration of analytes in a test sample. It measures the accuracy of a sensor. The recovery is quantified in percentage. A high percentage of recovery close to 100% denotes the high accuracy of a sensor.

2.4 Methods of Analysis

2.4.1 Square Wave Anodic Stripping Voltammetry

Stripping voltammetry is an ultrasensitive amperometric technique and the most widely used technique for metal ion detection. Square Wave Anodic Stripping Voltammetry (SWASV) allows for the rapid detection of heavy metal ions in water with high accuracy. SWASV has two steps for the sensing target analytes at the sub nanomolar range. The first step is deposition or accumulation (reduction) where the target analyte or chemical species are electrodeposited on an electrode surface by applying a constant potential. Due to this preconcentration step, a lower detection limit of target analyte in sub nanomolar range can be achieved [146]. The deposition step may be an anodic or cathodic reaction. Generally, the deposition involves the cathodic process where the target analytes or species from the electrolyte solution are reduced on the electrode surface (Figure 2.2). The second step is stripping (oxidation) where the electrode is scanned with an applied range of voltage using square wave voltammetry (SWV). During stripping, the deposited or preconcentrated analytes as a thin film or amalgam on the electrode surface will be stripped or oxidized at a specific potential. Each analyte or species has unique stripping or oxidation potential. The accumulation of electrons during stripping will result in faradic current which is proportional to the concentration of the target analytes or species. The combination of stripping potential and faradic current information enables both the identification of the ion as well as the concentration.

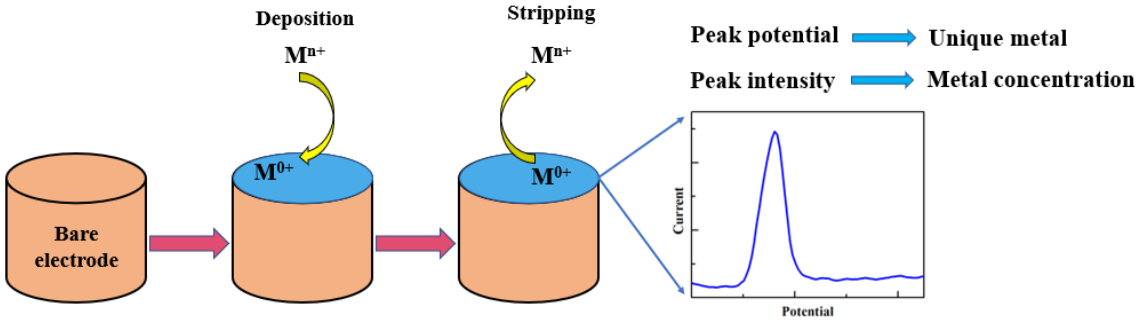

Figure 2.2 Principle of square wave anodic stripping voltammetry.

SWV is a form of linear potential sweep voltammetry where a symmetrical square wave is superimposed on a staircase potential (Figure 2.3). The current is sampled at the end of the forward pulse (i_1) and reverse pulse (i_2). Consequently, the effect of capacitive current (non-faradaic or charging) on the faradic current signal is minimized.

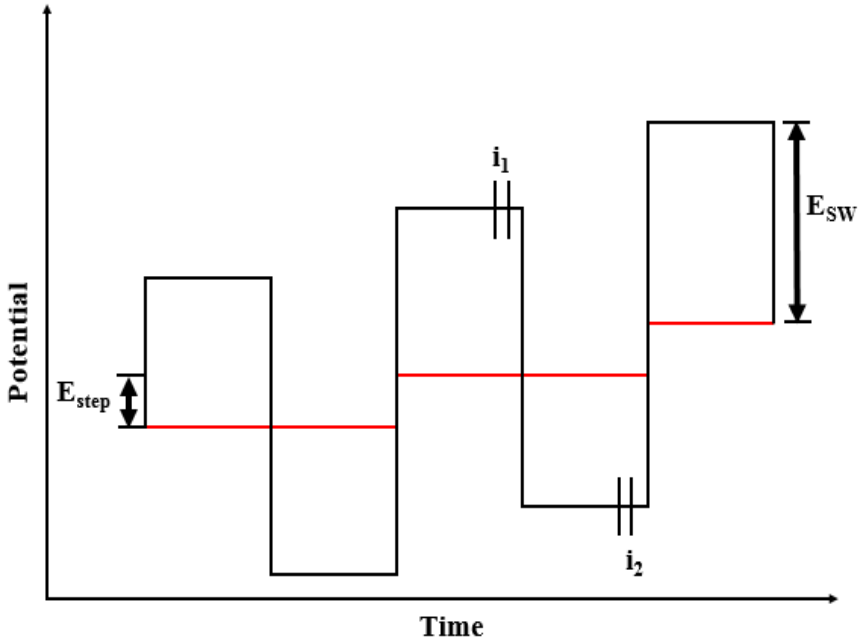

Figure 2.3 A symmetrical square wave is superimposed on a staircase potential.

The net current (i_1-i_2) is shown in Figure 2.4 where the peak current is directly proportional to the concentration of the target analyte in the solutions.

$$\Delta i_p = \frac{nFAD_0^{1/2}C_0^*}{(\pi t_p)^{1/2}}\Delta\Psi p \qquad (2.3)$$

where Δi_p denotes differential peak current, A is electroactive surface area, C_0* is the concentration of analytes, D_0 is diffusion constant, t_p is the pulse width, and $\Delta\Psi_p$ is a unitless parameter that measures the peak height of SWV.

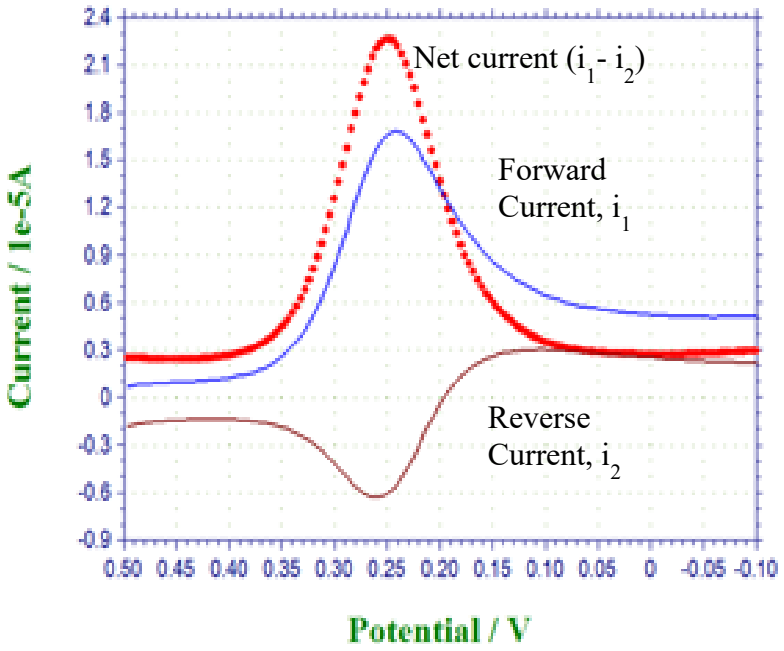

Figure 2.4 A typical square wave voltammetry curve. The voltammogram consist of a forward current (i_1), reverse current (i_2), and net current (i_1 - i_2) [147].

2.4.2 Cyclic Voltammetry

Cyclic voltammetry is a voltammetry technique where a voltage is applied linearly with time in an electrochemical cell and the resulting current is measured between the working electrode and the counter electrode. Cyclic voltammetry is widely used to analyze the redox behavior of chemical species, reaction kinetics, and electron transfer properties of redox species [148].

In cyclic voltammetry, the potential between the working electrode and the counter electrode is linearly varied from a negative to a positive potential with the help of a potentiostat which is called forward scan (Figure 2.5). Further, the applied voltage is swept back to the reverse direction from positive to negative voltage until it reaches a preset value which is called a reverse scan. This forward and reverse scan are repeated multiple times and the resulting current between the working electrode and the counter electrode is recorded and plotted for potential. The resulting 'duck-shaped' plot is known as a cyclic voltammogram.

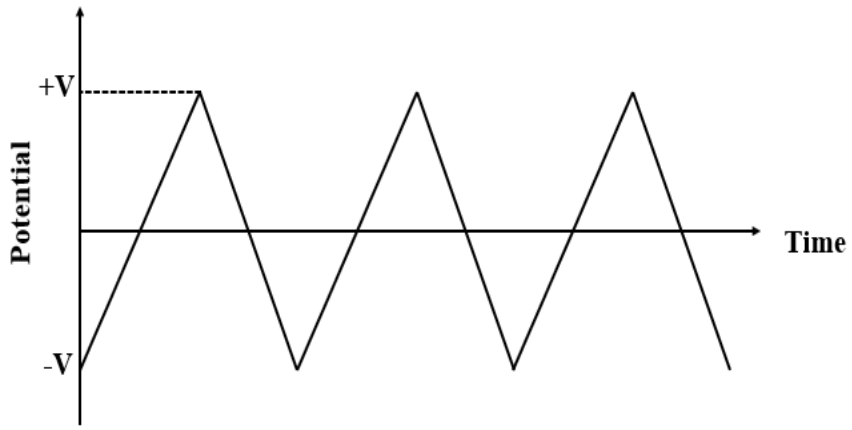

Figure 2.5 A triangular voltage waveform.

A typical plot of cyclic voltammograms is shown in Figure 2.6. Here, in the beginning, the voltage is swept in a forward scan and then in a reverse scan with a triangular voltage. In the forward scan, the voltage of the working electrode is scanned from a negative voltage (- 0.4 V) to a positive voltage (+ 0.4 V). In the beginning, the potential is not enough to oxidize the analyte (point a). The oxidation of analyte on the working electrode starts at oxidation onset potential E_{onset} and resulting oxidation current increases

exponentially with increasing scanning potential (point b). Due to applied potential, the analyte (M) near to the working electrode will start to oxidize i.e. lose electrons and become M^+. The transfer of electron will result in an electrical current which is called faradic current. Meanwhile, the unreacted analytes (M) will diffuse toward the working electrode due to the concentration gradient of analytes and oxidized and a diffuse double layer (DDL) near to electrode surface of the sub-nanometer-thick is formed by the building of M^+ on an electrode surface. This DDL controls the rate at which analytes diffuse toward the electrode. Once the DDL reaches a certain size or certain thickness, the diffusion process becomes slow down. As a result, the current reaches to maximum called anodic peak current i_{pa} at point c with anodic peak potential E_{pa}.

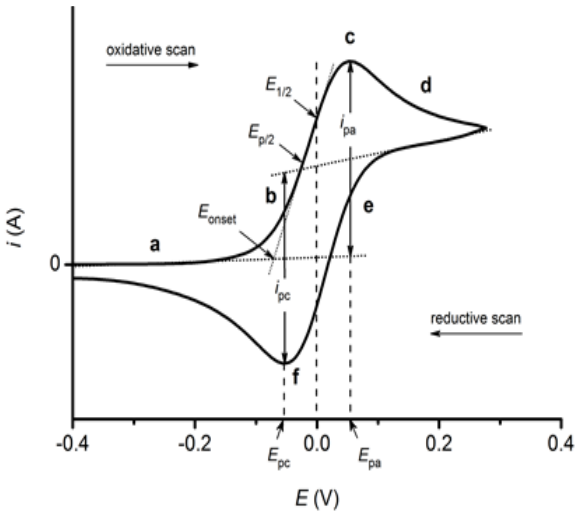

Figure 2.6 Cyclic voltammogram for a reversible electrochemical process [148].

Further, the increase of positive voltage results in a decrease in the current (point d) until a steady-state arrives where there has no effect of further increase of positive voltage. Here, this phenomenon is due to the increase of DDL thickness which impedes the diffusion of M to the electrode, resulting in a decrease in an oxidation reaction and

eventually decreasing the anodic current. During the reverse scan, the analytes still get oxidized until it reaches the voltage where the oxidized analyte on the electrode surface can be reduced (point e). The reduction process is the reverse process of the oxidation process in the opposite direction with a cathodic peak current (i_{pc}) and cathodic peak potential (E_{pc}) (point f). Here, during the reverse sweep of voltage, M^+ close to the electrode starts to reduce (gain of electrons) and becomes M by creating a negative or cathodic current. Due to the concentration gradient, M^+ will diffuse toward the electrode and get reduced eventually increasing the cathodic current. Once the diffusion layer builds up to a certain size, the diffusion of M^+ will become slow down and cathodic current will eventually start to decrease. For a reversible redox process, the anodic peak current and cathodic peak current should be equal in magnitude with an opposite sign. Randles-Sevcik equation describes the peak currents, i_p of a reversible redox system by the following equation [148]:

$$i_p = (2.69 \times 10^5) n^{3/2} A C D^{1/2} v^{1/2} \quad (2.4)$$

Where n denotes the number of electrons involved in the redox process, A is the area of the electrode (cm^2), C is the concentration of an analyte (mol cm^{-3}), D is the diffusion coefficient (cm^2 s^{-1}), and v is the scan rate of potential (V s^{-1}).

2.4.3 Electrochemical Impedance Spectroscopy

Electrochemical Impedance Spectroscopy (EIS) is an important characterization technique for the understanding of the dynamics of an electrochemical process. EIS reveals the response of an electrochemical cell due to the application of electrical potential. This technique is widely used to characterize battery, fuel cells, supercapacitors, and

electrochemical devices. EIS involves the application of an AC voltage and the response of the system is recorded as a function of frequency which reveals the internal dynamics of a nonlinear electrochemical process. The electrochemical impedance is defined as follows [149, 150]:

$$Z = \frac{V_0 \sin(\omega t)}{I_0 \sin(\omega t + \varphi)} = Z_0 \frac{\sin(\omega t)}{\sin(\omega t + \varphi)} \quad (2.5)$$

Where Z is the impedance, V_0 is the amplitude of voltage, I_0 is the amplitude of current, ω is the angular frequency, t is the time, and φ is the phase. By plotting the equivalent electrical circuit, the value of resistance and capacitance can be determined. Most of the electrochemical cells have two types of resistance: a solution resistance due to the electrolyte and charge transfer resistance at the electrode-electrolyte interface. The solution resistance can be used to determine the ionic conductivity of the electrolyte. The electrode-electrolyte interface can be modeled as a capacitance. Charge transfer resistance determines the charge carrier dynamics and current exchange in the electrode-electrolyte interface. Due to the accumulation of counter ions from electrolyte close to the electrode form an electrical double layer (EDL) which in turn develops a capacitance in the electrode-electrolyte interface [150]. However, the capacitance in electrode-electrolyte behaves nonlinearly which can be ascribed to the non-uniform redox reaction rates and roughness of the electrode surface. In terms of a complex number, the sinusoidal ac voltage and current can be expressed as follows [151]:

$$V(\omega, t) = V_0 \exp(j\omega t) \quad (2.6)$$

$$I(\omega, t) = I_0 \exp(j\omega t - \theta) \quad (2.7)$$

where $j^2 = -1$, V_0, and I_0 is the amplitude of voltage and current, respectively. Thus, equation (2.5) can be written as:

$$Z(j\omega) = \frac{V(\omega,t)}{I(\omega,t)} = \frac{V_0}{I_0} e^{j\theta} = Z_{0e^{j\theta}} \qquad (2.8)$$

According to Euler's formula with substituting Z_0 by |Z|, the equation (2.8) can be expressed as follows:

$$Z(j\omega) = |Z|(\cos\theta + j\sin\theta) \qquad (2.9)$$

Equation (2.9) can be further expressed as follows:

$$Z(\omega) = Z_{re} + jZ_{im} \qquad (2.10)$$

Where $Z_{re} = |Z|\cos\theta$ and $Z_{im} = |Z|\sin\theta$

Further, the EIS data can be interpreted as a Nyquist plot where the imaginary impedance (Z_{im}) of an electrochemical cell is plotted against real impedance (Z_{re}). The equivalent model of an electrochemical cell in terms of electrical parameters is called Randles equivalent circuit [152]. Figure 2.7 shows a typical Nyquist plot for an electrochemical sensor and Figure 2.8 shows the Randles equivalent circuit. It can be seen that Nyquist plots contained a semicircle at higher frequencies corresponding to the electron-transfer-limited process and a straight line at lower frequency indicating the diffusion-limited process [153, 154]. The diameter of the semicircle represents the charge transfer resistance (R_{ct}) of the electrode-electrolyte interface. R_s and W represent the solution and Warburg diffusion resistance, respectively. Warburg diffusion resistance describes the diffusion of analytes or chemical species toward the electrode or away from the electrode. The double-

layer capacitance formed on the electrode-electrolyte interface is represented by C [155]. Due to the accumulation of the ions close to the electrode surface, the capacitance increases at electrode-electrolyte interfaces. The non-ideal behavior of the capacitor can be ascribed to the surface roughness of electrode and uneven reaction rates.

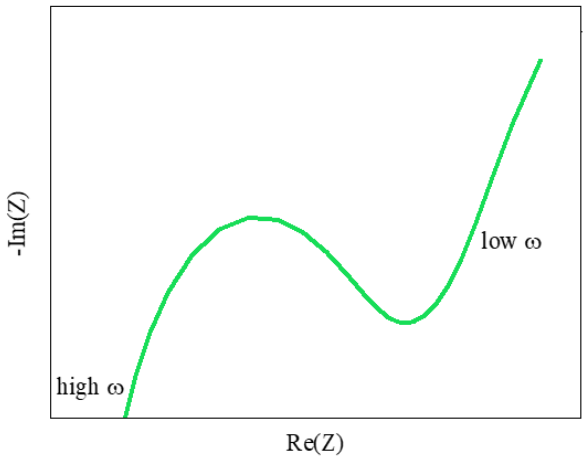

Figure 2.7 Typical Nyquist plot for an electrochemical sensor consists of a semicircle and a linear curve. The diameter of the semicircle denotes charge transfer resistance.

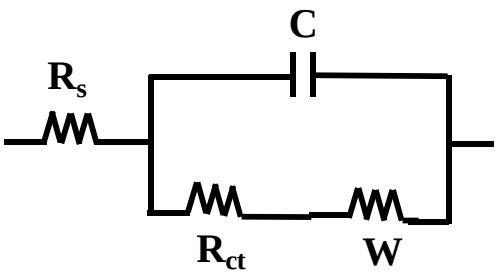

Figure 2.8 Randles equivalent circuit consists of R_s, R_{ct}, W, and C.

2.5 Reduction Potential and Standard Reduction Potential

Reduction potential, measured in volts (V) or millivolts (mV), refers to the potential of a chemical species which determines the tendency of a chemical species (ion or molecule) to be reduced by gaining electrons [156]. It is noted that each chemical species possesses an intrinsic reduction potential. The more positive the reduction potential of a chemical species, it is more likely that the chemical species gains an electron and therefore more tendency to be reduced. To calculate the reduction potential of a redox reaction under non-standard conditions i.e. at any temperature and concentration of reactants and products, the following Nernst equation is used [157].

$$E = E^0 - \frac{RT}{nF} lnQ \qquad (2.11)$$

where E denotes the reduction potential under non-standard condition, E^0 is the standard reduction potential, n is the number of transferred electrons in the reaction, Q is the reaction quotient, T is temperature, R and F are the gas and Faraday constants, respectively. $Q = \frac{C^c D^d}{A^a B^b}$ for the following reaction:

$$aA + bB \rightarrow cC + dD \qquad (2.12)$$

The standard reduction potential is defined as the reduction potential that measures the tendency of a chemical species to be reduced under standard conditions. The standard conditions include a temperature of 25 °C, the concentration of chemical species will be 1 molar (M), and the pressure will be 1 atm. The standard reduction potential is usually measured relative to a Standard Hydrogen Electrode (SHE), which has a potential of zero volts. The symbol of standard reduction potential is E^0_{red} or E^0. It is measured in a half-reaction. Below are a few examples of standard reduction potential (E^0) for a few chemical

species [158]. Here, Hg^{2+} has a more positive standard reduction potential than Cu^{2+} and Ag^{+}, which means Hg^{2+} has more tendency to reduce over Cu^{2+} and Ag^{+} in a solution.

$2H^{+} + 2e^{-} \rightleftharpoons H_2(g)$; $E^0 = 0$ V

$Cu^{2+} + e^{-} \rightleftharpoons Cu\,(s)$; $E^0 = +\,0.34$ V

$Hg^{2+} + 2e^{-} \rightleftharpoons Hg(l)$; $E^0 = +\,0.85$V

$Ag^{+} + e^{-} \rightleftharpoons Ag(s)$; $E^0 = +\,0.7996$ V

On the other hand, the standard oxidation potential is defined as the is the oxidation potential that measures the tendency of a chemical species to be oxidized by losing electrons under standard conditions. The more negative the standard oxidation potential of a chemical species, it is more likely that the chemical species leaves electron and therefore more tendency to be oxidized. Standard oxidation potential (E^0_{ox}) is the opposite of the standard reduction potential (E^0_{red}) for a species ($E^0_{ox} = -\,E^0_{red}$).

2.6 Operating Principle of the Characterization Techniques

2.6.1 Raman Spectroscopy

Raman spectroscopy is an important characterization technique for the understanding of material characteristics including chemical structure, crystallinity, molecular structure, molecular bonds [159]. Raman spectroscopy involves the scattering phenomenon between a high-intensity light incident from a laser source and a chemical bond within a material. If the scattered photon has the same wavelength ($\lambda_{scatter} = \lambda_{laser}$) of the incident laser due to the interaction with the material, it is called elastic scattering or

Raleigh scattering. Here, the scattered photon conserves the same energy of an incident photon, but different direction. This Rayleigh scattering does not provide any information about the characteristics of material [160].

In contrast, if the scattered photon has a different wavelength (usually $\lambda_{scatter} > \lambda_{laser}$) than the incident laser due to the exchange of energy between laser light and material, it is called Raman scattering or inelastic scattering. Since the molecule gains energy, the photon shifts to lower energy. This Raman scattering can provide useful information about the characteristics of a material such as chemical structure, crystallinity, molecular structure, and phase. A typical Raman spectrum shows several peaks with different intensities and wavelengths. The intensity of the peak relates to the crystallinity of a material. A narrow and high-intensity peak means high crystallinity of material [161]. On the other hand, wide and low-intensity peak denotes disorder in the crystal structure of a material. Each peak denotes a vibrational property of a specific molecular bond including C-C, C-H, C-N, C=O, etc. For instance, because of Raman scattering, graphene shows two characteristic peaks in the Raman spectrum such as D band at 1350 cm^{-1} and G band at 1580 cm^{-1} (Figure 2.9) due to the sp^3 hybridized carbon and the first order in-plane scattering of the E_{2g} phonon of the sp^2 carbon lattice, respectively [115, 162, 163].

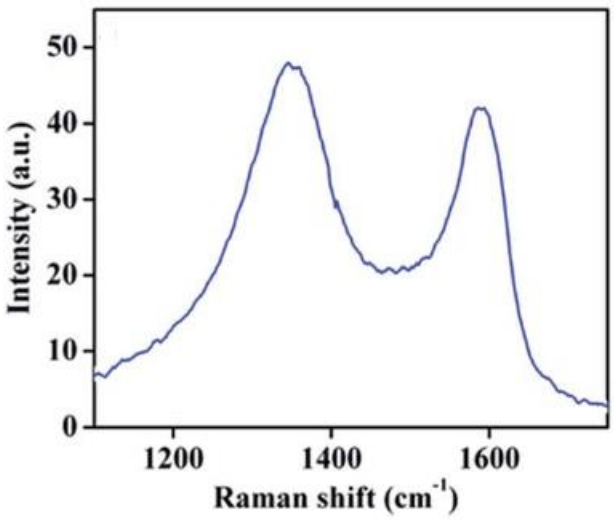

Figure 2.9 Raman spectrum of graphene [115].

Since Raman shifts are related to energy, it is usually expressed in terms of wavenumber which is the inverse of wavelength i.e. cm^{-1}. The equation of Raman shift can be expressed as follows [164]:

$$\nabla v = \left(\frac{1}{\lambda_0} - \frac{1}{\lambda_1}\right) \tag{2.13}$$

where ∇v is the Raman shift (cm^{-1}), λ_0 is the wavelength of incident laser, and λ_1 is the wavelength of scattered light. As the wavelength is expressed in a nanometer, so the above equation can be written as follows.

$$\nabla v\ (cm^{-1}) = \left(\frac{1}{\lambda_0(nm)} - \frac{1}{\lambda_1(nm)}\right) \times \frac{10^7 nm}{cm} \tag{2.14}$$

2.6.2 X-ray Diffraction

X-ray diffraction (XRD) is an important technique to get detailed information about the crystal structure of materials. Qualitative and quantitative information about

crystallinity (such as single crystalline, polycrystalline, and amorphous), phase, the lattice constant, and crystal plane of a material can be found from X-ray diffraction. When a beam of X-rays is incident on the crystal plane of a sample, the incident X-rays are scattered and diffracted by the atoms of the target material (Figure 2.10). Further, the diffracted X-rays undergo constructive or destructive interference based on the crystallinity of the material. The constructive interference of diffracted X-rays produces a diffraction pattern with an intensity depending on the type and orientation of atoms in the crystal structure.

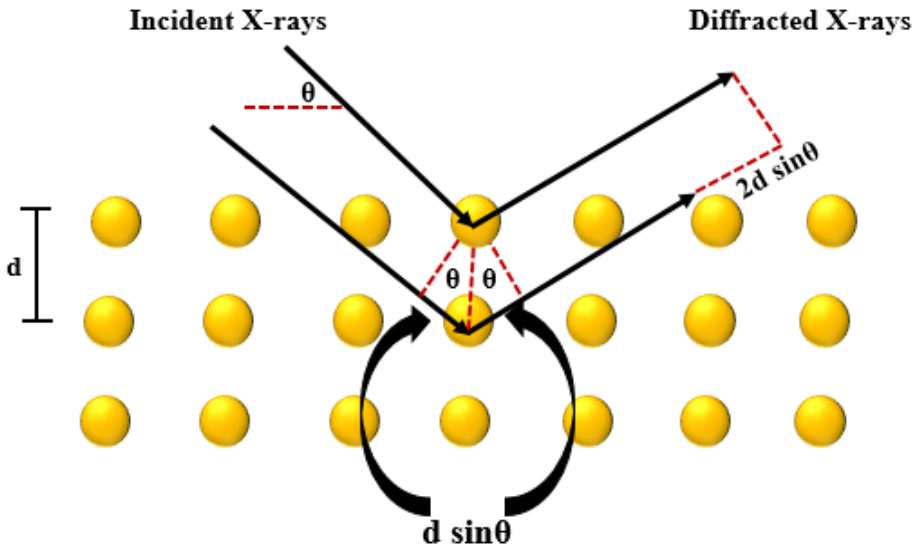

Figure 2.10 Schematic diagram of the principle of X-ray diffraction.

Bragg's law describes the constructive interference of diffracted X-rays by the equation below [165].

$$2d\sin\theta = n\lambda \qquad (2.13)$$

where d denotes the spacing between two crystal planes, θ is the angle between incident X-ray and the crystal plane, λ denotes the wavelength of the incident X-ray, 2dsinθ is the path difference between the incident and diffracted x-rays, and n is an integer.

2.6.3 Scanning Electron Microscopy

An electron microscopy for the imaging of a sample surface using a high energy electron beam is known as a scanning electron microscope (SEM). It is used to characterize the surface morphology of a material by detecting the emitted secondary electrons because of the interaction between high energy primary electrons and atom of the sample. It allows the imaging of the morphology of a sample with the magnification of up to 300,000x and resolution of 3 nm [166]. Figure 2.11 shows the schematic diagram of a typical scanning electron microscope. Here, an electron gun (cathode) which contains tungsten filament generates an electron beam by the high voltage. The generated electron beam is accelerated downward by the strong electric field between anode and cathode and these electron beams are known as primary electrons. The electrons are focused into an electron beam through a condenser lens and the scanning coils produce magnetic fields that cause back and forth deflection (scanning) of the condensed beams. Further, the primary electron beams are focused on the sample surface by the electromagnetic lens called the objective lens. After the incidence of primary electrons on the target sample, loosely bonded outer electrons of an atom are emitted which are called secondary electrons. These secondary electrons are collected by a secondary electron detector for imaging and gives information about the surface topography. On the other hand, when the primary electrons penetrate the depth of the sample, a few electrons are reflected due to elastic scattering which is called Back Scattered Electron (BSE). The elemental distribution of a material can be provided by these

BSE. In addition, characteristics X-rays are emitted when a primary electron removes an inner shell electron and eventually a high energy electron from outer shell jumps to fill that inner shell vacancy by releasing an x-ray. The energy of characteristics X-rays is measured by Energy Dispersive x-ray Spectroscopy (EDS) which gives information about elemental identity, elemental composition, and elemental mapping.

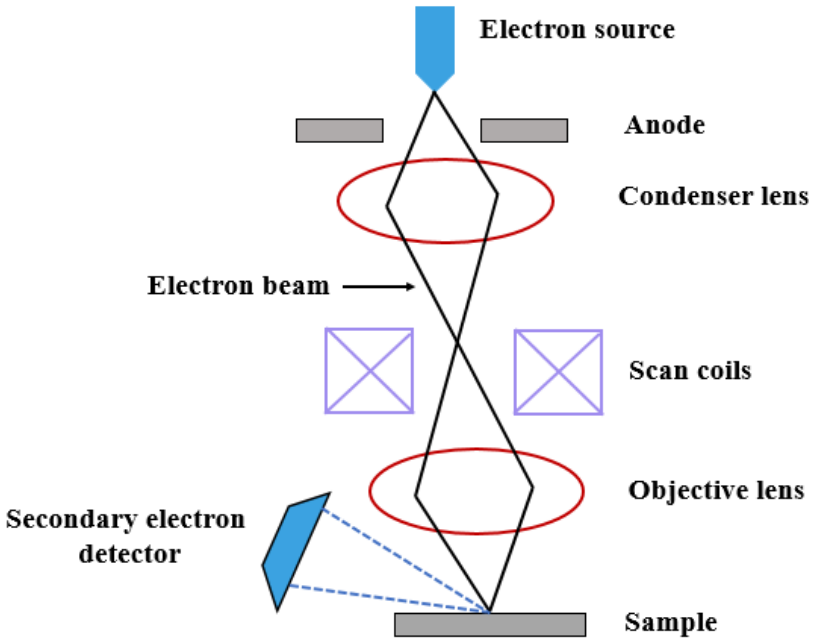

Figure 2.11 Schematic diagram of the principle of scanning electron microscopy.

2.6.4 Transmission Electron Microscopy

An electron microscopy to visualize and analyze a sample in the scale of a micrometer to a nanometer is known as transmission electron microscopy (TEM). It gives detailed information about the microstructure of a sample with high magnification and resolution images. It allows the imaging of the morphology of a sample with the magnification of up to 1,000,000x and resolution below 1 nm [166]. TEM provides

quantitative and qualitative analysis of morphology, crystal structure, crystallization, growth of layers, crystal orientation, crystal phases, lattice constraints, chemical composition, and defects in semiconductors of a sample. TEM works on the principle of an image created by the transmission of a high energy electron beam through a sample in a high vacuum which is captured by a detector. Here, the transmission of electrons strongly depends on the thickness, structure, and properties of the material including material density, elemental composition, etc. For instance, thin and porous material will allow more electrons to transmit while the thicker and dense material will allow a few electrons to transmit. The transmitted electrons are projected into a phosphor screen for imaging [166]. Figure 2.12 illustrates the schematic diagram of the TEM.

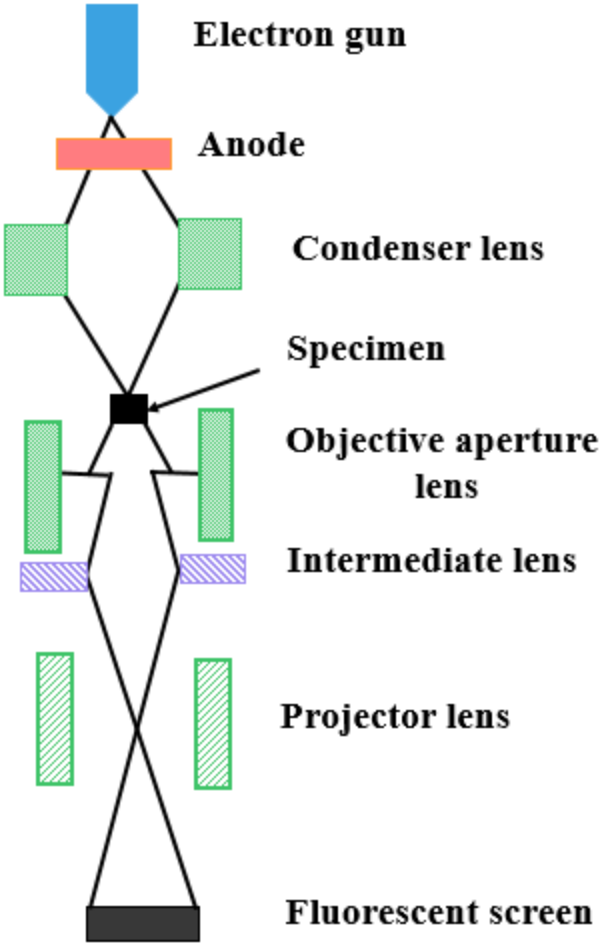

Figure 2.12 Schematic diagram of the principle of transmission electron microscopy

The thermally generated electrons from a tungsten filament cathode are accelerated toward the sample. Meanwhile, the condenser lens focused the electrons on a sample while part of it transmitted through the sample based on the thickness of the sample. After transmitting through the specimen, the electron beams will be refocused into an image on a phosphor screen by an objective lens. The contrast of the image is enhanced by the objective lens. Two other lenses including intermediate lens and projector lens enlarged the resulting image which further strikes on a phosphor screen. The striking image on the

phosphor screen produces light which allows users to visualize the image. If more electrons transmitted through the sample, it represents a lighter area on the TEM image and if fewer electrons transmit through the sample that area is represented by a dark area on the TEM image.

2.6.5 Fourier Transform Infrared Spectroscopy

Fourier Transform Infrared Spectroscopy (FTIR) is an analytical instrument that is used for the chemical identification of organic, inorganic, and polymeric materials [167]. In FTIR analysis, infrared radiation with a wavelength in the range of 100-10,000 cm^{-1} is sent through a sample where a portion of the incident light is absorbed and a portion is transmitted. Figure 2.13 shows a schematic diagram of the FTIR spectrometer. A beam of light from a coherent source is split into two parts by a beam splitter A part of the split beam is directed toward a moving mirror that moves at a constant velocity and another part is reflected in a fixed mirror. The recombined beam is passed through the sample and detected through a detector. The detected signal is finally interpreted as a spectrum representing a molecular fingerprint of the sample. Each molecule or chemical bond shows a unique fingerprint at a specific wavelength in the spectrum [167, 168].

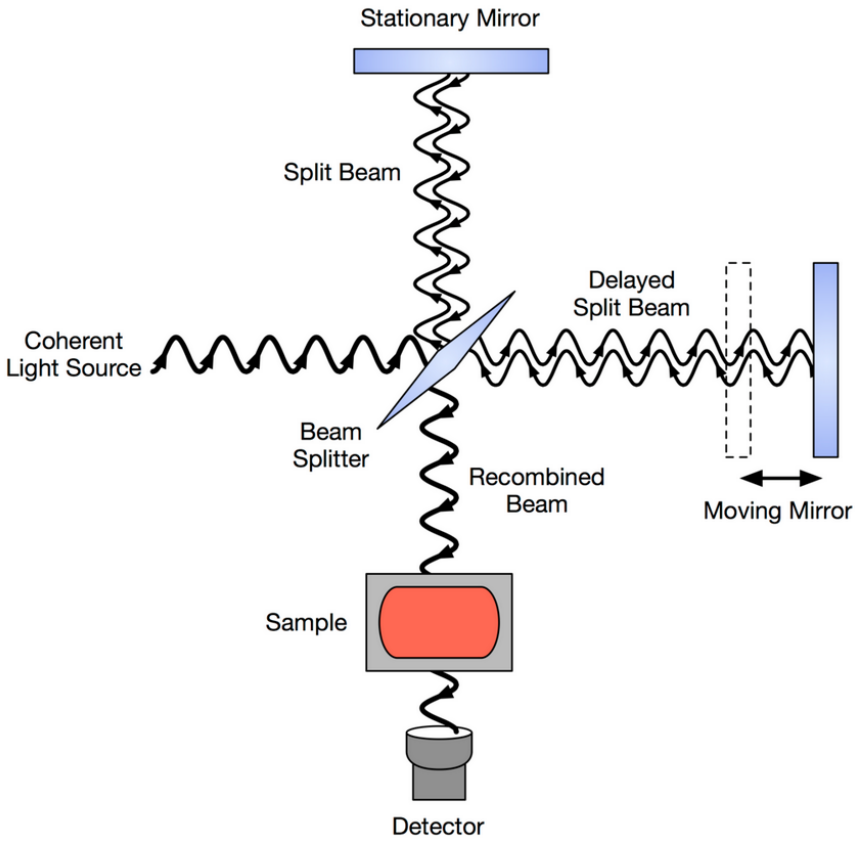

Figure 2.13 Schematic diagram of an FTIR spectrometer [168].

CHAPTER 3 EXPERIMENTAL PROCEDURES

3.1 Materials

Table 3.1 List of materials with Chemical Abstracts Service (CAS) number and vendor

Name	CAS #	Vendor
Sodium acetate (CH_3COONa), ≥99.0%	127-09-3	Sigma Aldrich
Acetic acid (CH_3COOH)	64-19-7	
N,N-Dimethylformamide (C_3H_7NO)	68-12-2	
Chromium (III) bromide hexahydrate ($Br_3Cr \cdot 6H_2O$), 99%	13478-06-3	
Thiourea (CH_4N_2S), ≥99.0%	62-56-6	
Graphene oxide powder ($C_xO_yH_z$)	796034	
Oxalic acid dihydrate ($C_2H_2O_4.2H_2O$), ≥99%	6153-56-6	
Silver Nanowires (AgNWs), 0.5% (isopropyl alcohol suspension)	7440-22-4	

Name	CAS #	Vendor
Potassium ferricyanide (III) ($C_6N_6FeK_3$), <10 μm, 99%	13746-66-2	Fisher Scientific
Lead chloride ($PbCl_2$), 98%	7758-95-4	
Cupric chloride ($CuCl_2$), 99.999%	7447-39-4	
Cadmium nitrate ($CdNO_3$), 99.997%	10022-68-1	
Sodium chloride (NaCl), ≥99.5%	7647-14-5	
Tin (II) chloride ($SnCl_2$), ≥99.99%	7772-99-8	
Silver nitrate ($AgNO_3$), ≥99.0%	7761-88-8	
Iron (III) chloride ($FeCl_3$), ≥99.99%	7705-08-0	
Nickel (II) chloride ($NiCl_2$), anhydrous, 99.99%	7718-54-9	
Ammonium tungsten oxide hydrate ($(NH_4)6W_{12}O_{39}\cdot xH_2O$)	12333-11-8	
Potassium chloride (KCl), 99%	7447-40-7	
Mercury (II) chloride ($HgCl_2$), 99%	7487-94-7	STREM chemicals

Platinum (Pt) electrode of 1.6 mm diameter was purchased from Bioanalytical Systems Inc., USA. The body of the Pt electrode is made of polytetrafluoroethylene (PTFE) with a Cu-Cr alloy as a contact. Glassy carbon electrode (GCE) with a diameter of 3.0 mm diameter was purchased from CH Instruments, Inc., Texas, USA. The reference electrode (Ag/AgCl) and counter electrode (platinum wire) were purchased from AMETEK Scientific Instruments, USA. A Fisher Science Education pH meter was purchased from Fisher Scientific, USA.

3.2 Fabrication of Electrochemical Sensors

3.2.1 Preparation of Graphene Oxide-Silver Nanowires Composite Dispersion

Figure 3.1a shows the GO powder as received. To prepare the GO dispersion, 6.0 mg of GO powder was weighed and added to 6.0 mL absolute ethanol. A homogenous dispersion of GO (1.0 mg mL^{-1}) was obtained by the ultrasonication of the above mixture for 2 hours at 25°C. The dispersion of GO was kept at room temperature (Figure 3.1b). Meanwhile, the suspension of silver nanowires (AgNWs) was magnetically stirred for 30 min under room temperature (Figure 3.1c). Then different weight ratios of GO and AgNWs composite were prepared by mixing AgNWs suspension into GO dispersion followed by stirring for another 20 min (Figure 3.1d). Three different weight ratios of GO-AgNWs composite such as GO:AgNWs = 1:1, GO:AgNWs = 1:2, GO:AgNWs = 1:0.5 were prepared to find the optimum weight ratio.

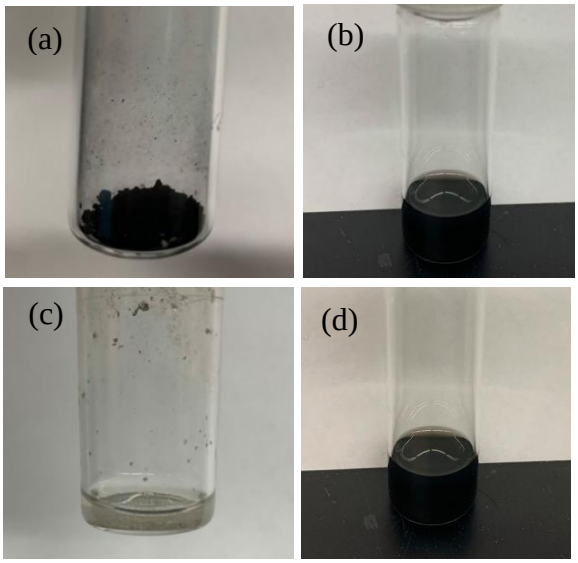

Figure 3.1 (a) GO powder (b) Dispersion of GO (c) AgNWs dispersion (d) GO-AgNWs dispersion obtained by centrifugation.

3.2.2 Hydrothermal Synthesis of 1T-WS_2 and 2H-WS_2 Microflowers

A simple hydrothermal method was exploited for the synthesis of 1T- WS_2 microflowers. Figure 3.2 shows the schematic diagram of the hydrothermal synthesis of 1T- WS_2. In the beginning, 0.7g of ammonium tungsten oxide hydrate and 0.7g of thiourea were weighed and their mixture was dissolved in 30 mL of deionized water under magnetic stirring for 30 min. Meanwhile, 0.9g of oxalic acid dihydrate was weighed and added in the above mixture as a catalyst. The resulting mixture was stirred for another 30 min to achieve a homogeneous solution. After that, the mixture was transferred to a 40 mL Teflon-lined stainless steel autoclave and kept in a preheated furnace at 220 °C for 48 h. After that, the autoclave was cooled down at room temperature. The black solution was washed with ethanol by centrifugation at 3000 rpm for at least three times and dried at 60°C overnight under vacuum to obtain the black powder of 1T-WS_2.

For the synthesis of 2H-WS_2, 0.7g of ammonium tungsten oxide hydrate, 0.7g of thiourea, and 2.0g of oxalic acid dihydrate were dissolved in 30 mL of deionized water under magnetic stirring for 30 min. After that, the mixture was transferred to a 40 mL Teflon-lined stainless steel autoclave and kept at 200 °C for 24 h and followed the same procedure as 1T-WS_2 for the collection of black powder of 2H-WS_2. A Teflon-lined stainless steel autoclave and a furnace 1400 are shown in Figure 3.3a-b.

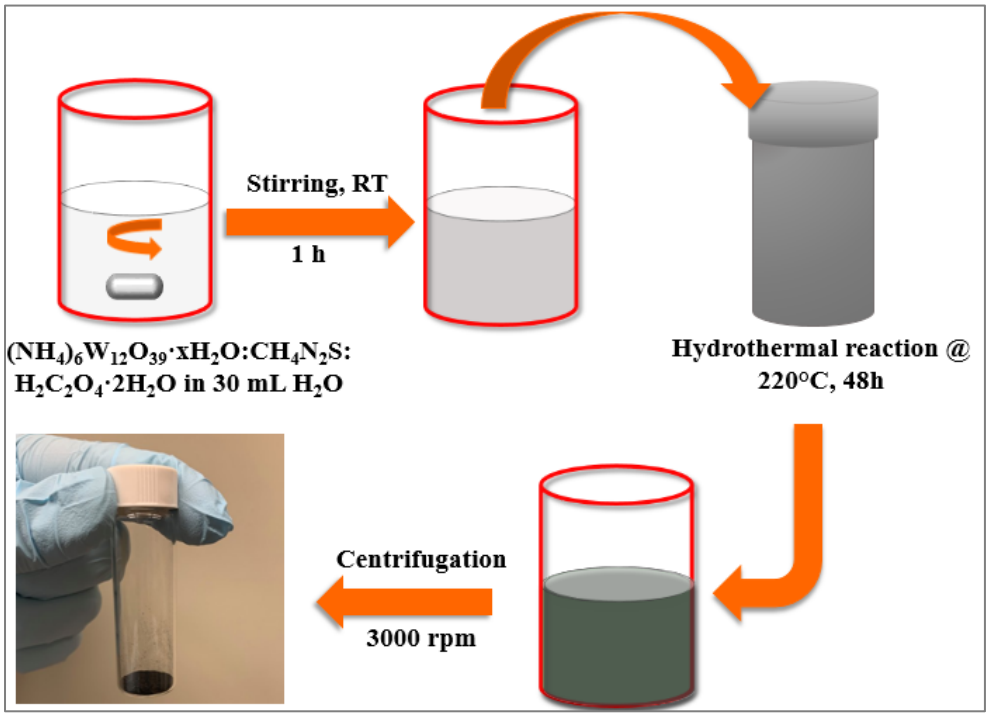

Figure 3.2 Schematic diagram of the hydrothermal synthesis of 1T-WS_2.

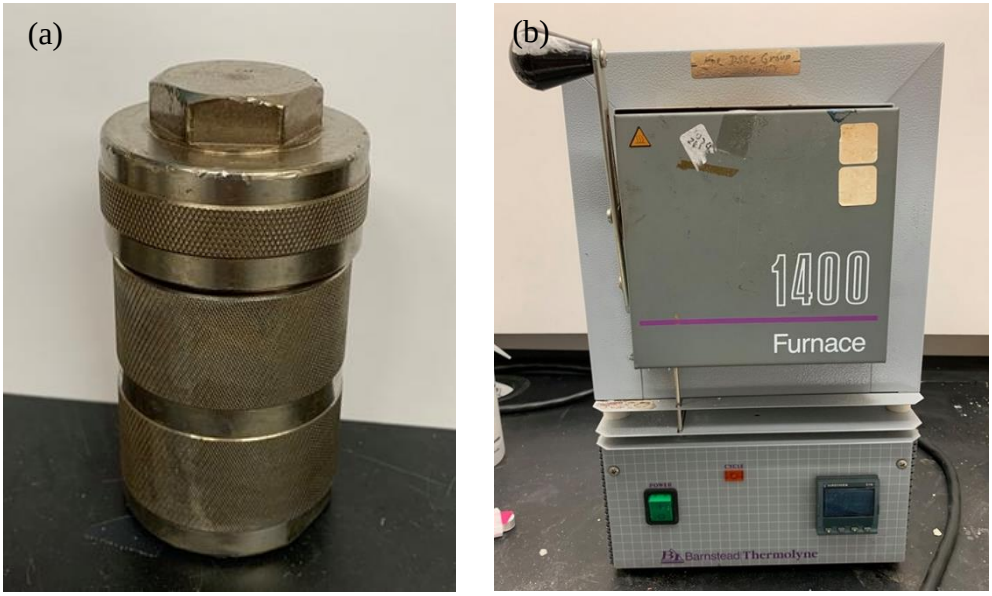

Figure 3.3 (a) Teflon lined stainless steel autoclave (b) A Barnstead Thermolyne furnace 1400.

3.2.3 Preparation of 1T-WS_2 Dispersion

In the beginning 2 mg, 4 mg, and 8 mg of WS_2 powder were weighed using a balance. Then different concentrations of WS_2 dispersion such as 0.5 mg mL^{-1}, 1 mg mL^{-1}, 2 mg mL^{-1} were prepared by dissolving 2 mg, 4 mg, 8 mg of WS_2 into 4 mL DMF. The resulting solutions were ultrasonically treated at room temperature for 1 hour to obtain a homogenous dispersion of WS_2. Figure 3.4a shows WS_2 powder synthesized using the hydrothermal method and Figure 3.4b shows the dispersion of 1 mg mL^{-1} WS_2 in DMF. Figure 3.5a and b show an ultrasonic cleaner bought from Kendal corporation.

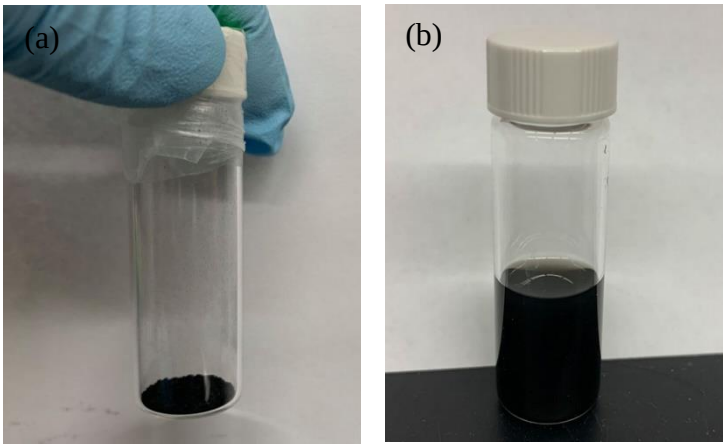

Figure 3.4 (a) WS_2 powder synthesized using hydrothermal method (b) Dispersion of 1 mg mL^{-1} WS_2 in DMF.

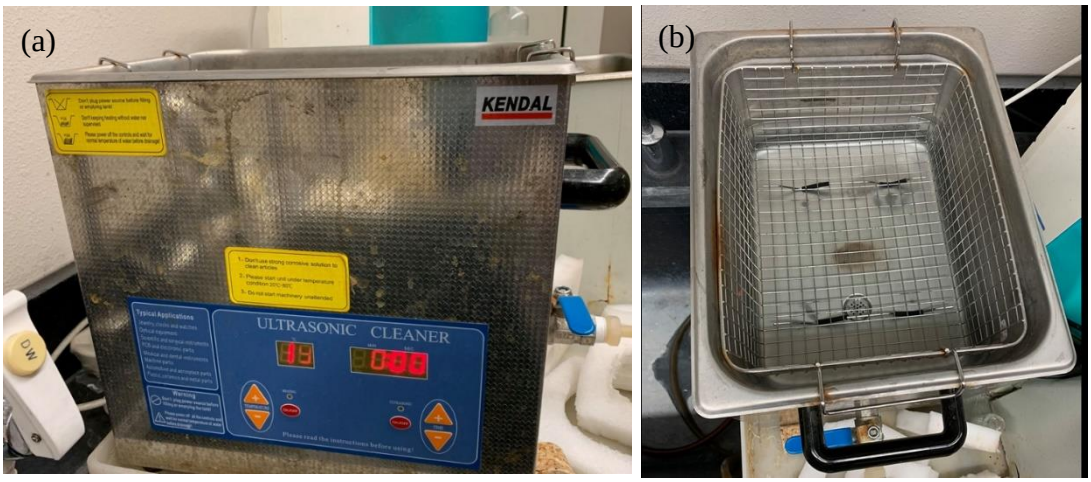

Figure 3.5 (a-b) An ultrasonic cleaner from Kendal corporation.

3.2.4 Fabrication of the GO-AgNWs Composite Modified Platinum Electrode

Figure 3.6a shows the as-received platinum electrode. A homogeneous slurry of alumina was prepared using three different alumina powders of 1.0 µm, 0.3 µm, and 0.05 µm size. Then Pt electrode was polished on a microfiber pad using alumina slurries to obtain a clean and shiny surface, rinsed with deionized water and ethanol, then dried with

nitrogen. A 5 µL dispersion of GO-AgNWs composite was drop-casted onto the Pt surface and dried under an ambient atmosphere (Figure 3.6b). The GO-AgNWs composite modified electrode was stored at 4 ^{o}C before testing.

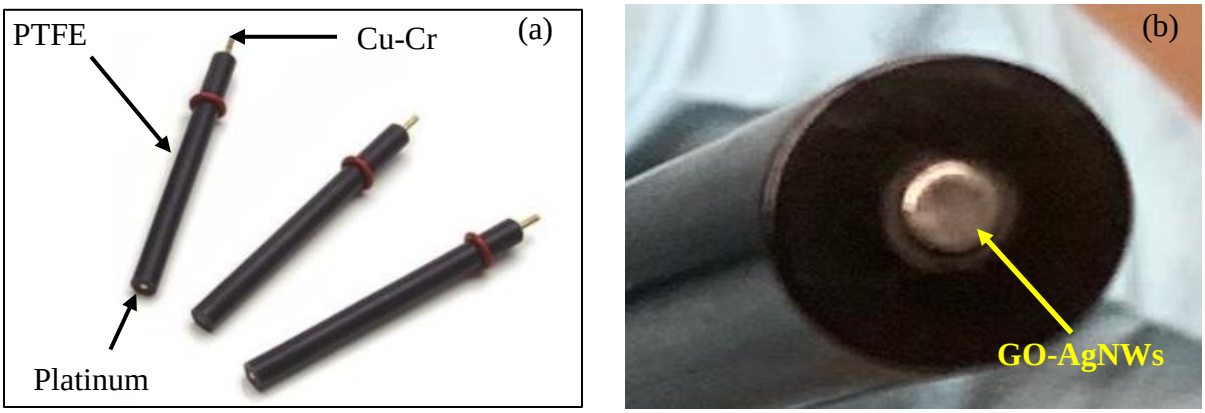

Figure 3.6 (a) Platinum electrode (b) Photographs of the as-prepared GO-AgNWs composite modified platinum electrode.

3.2.5 Fabrication of the 1T- WS_2 Modified Glassy Carbon Electrode

A homogenous dispersion of 1T-WS_2 into DMF was achieved by ultrasonic agitation for 1 h. Before the surface modification, the GCE was cleaned by polishing carefully with 1.0 µm, 0.3 µm, and 0.05 µm alumina powder on micro-cloth pads (Figure 3.7a) until a mirror shiny surface appeared, rinsing with ethanol followed by a deionized water rinse. Afterward, the electrode was dried under nitrogen [17]. A 5 µL of 1T-WS_2 dispersion was drop-cast on the surface of the clean GCE by a micropipette and the solvent was evaporated at 50^{o}C in a vacuum oven for 30 min to obtain the 1T-WS_2 modified GCE. Figure 3.7b shows an as prepared 1T-WS_2 modified GCE.

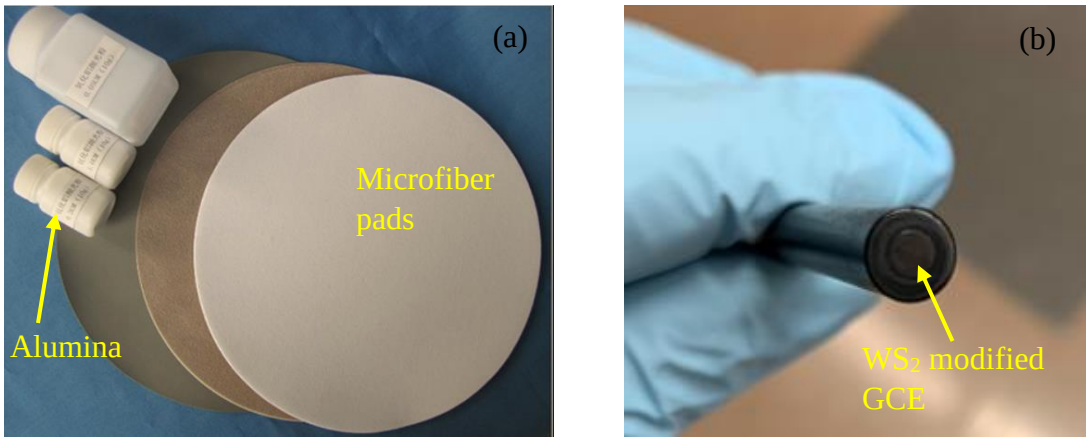

Figure 3.7 (a) Electrode polishing kits include alumina powders and microfiber pads (b) As-prepared 1T-WS_2 modified GCE.

3.2.6 Preparation of Electrolytes and Analytes

The electrochemical measurement for the detection of Hg^{2+} on GO-AgNWs modified electrode was carried out in 0.1 M KCl as the supporting electrolyte. To prepare 0.1 M KCl electrolyte, 298.2 mg of KCl was dissolved into 40 ml DI water, followed by centrifugation for 5 min. Figure 3.8a shows the prepared 0.1 M KCl electrolyte. To detect Hg^{2+} with 1T-WS_2 modified GCE, a 0.1 M acetate buffer solution was prepared by dissolving 328.12 mg of sodium acetate into 40 mL of deionized water. A stock solution of 0.1 M acetic acid was added into the above-mentioned sodium acetate solution the desired pH of the electrolyte was achieved. A Fisher science education pH meter was used to measure the pH of the electrolyte, while the pH meter was calibrated using standard PBS with pH 6.0. Deionized water was used to prepare all solutions unless specified otherwise. Figure 3.8b shows the prepared 0.1 M acetate buffer.

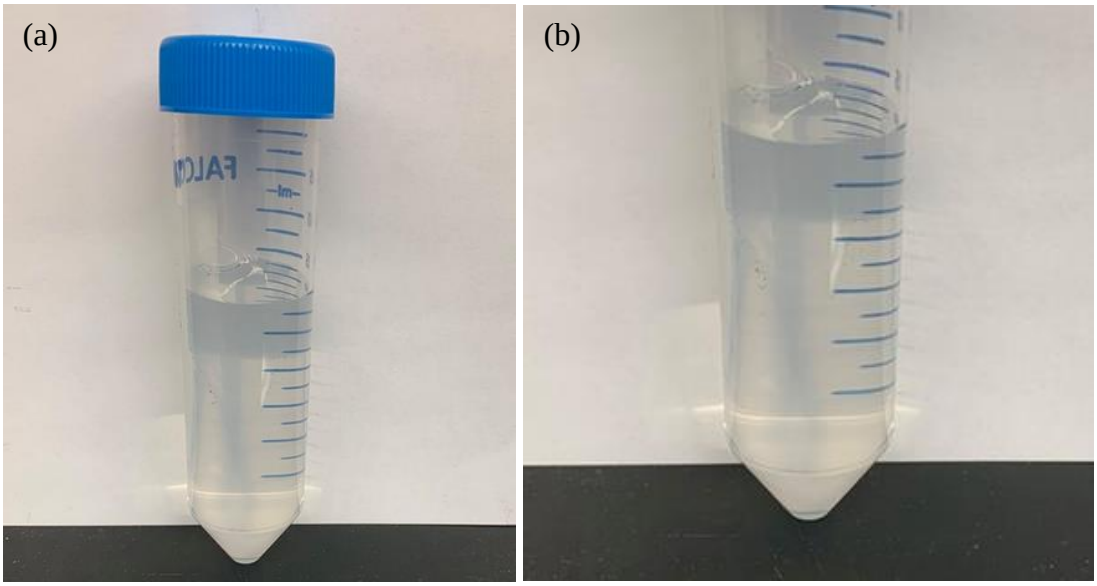

Figure 3.8 (a) As prepared 0.1 M KCl electrolyte (b) 0.1 M acetate buffer.

Different concentrations of stock solution of the analytes were prepared using equation (1).

$$m = CVM \qquad (3.1)$$

Where m = required mass of analyte (g), C = desired concentration of an analyte (M), V = desired final volume (L), M = formula weight of analyte (g/mol).

To achieve the desired concentration, the stock solution was diluted using the following formula.

$$M_1V_1 = M_2V_2 \qquad (3.2)$$

Where, M1 and V1 represent the molarity and volume of stock solutions, respectively, while M_2, V_2 represents the desired molarity and concentrations, respectively.

To calculate the molarity of an acid with a given concentration in wt %, the equation (3.3) was used.

$$[(\% \times d) / MW] \times 10 = \text{Molarity} \quad (3.3)$$

where, % = weight % (w/w); d = density (g/mL); MW = Molecular Weight (g/mol).

3.3 Electrochemical Characterization

3.3.1 Setup for Electrochemical Measurements

A three-electrode system comprised of GO-AgNWs composite modified platinum as a working electrode, Ag/AgCl (3 M KCl) as a reference electrode, and platinum wire as a counter electrode was used for all electrochemical measurements (Figure 3.9). A 20 mL electrochemical cell, 0.1 M KCl electrolyte, and different concentrations of Hg^{2+} were used throughout the electrochemical measurements [17].

For 1T-WS_2 modified GCE, the electrochemical experiments were performed on the same experimental setup except the working electrode made of 1T-WS_2 modified GCE and 0.1 M acetate buffer as an electrolyte.

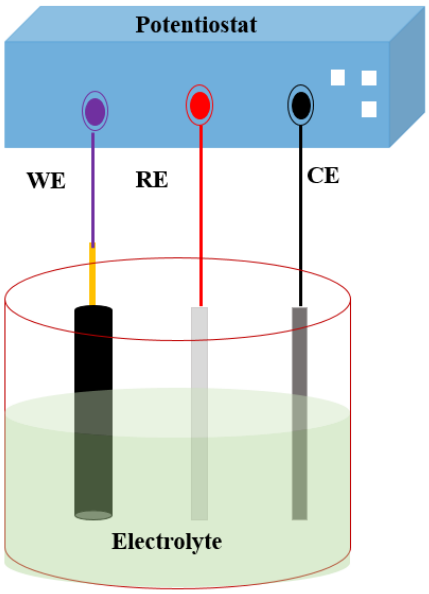

Figure 3.9 Schematic illustration of a three-electrode electrochemical cell.

3.3.2 Electrochemical Measurement Procedures

The electrochemical detection of Hg^{2+} was performed using SWASV in a three-electrode system at room temperature. For GO-AgNWs composite electrode, SWASV measurements were carried out in the presence of 0.1 M KCl and different concentrations of Hg^{2+} diluted into deionized water. The preconcentration (deposition) of mercury was conducted at - 0.4 V for 500 s under stirring. The stirring stopped at the end of the deposition time. The square wave voltammetry was recorded between 0 V to + 1.0 V with a frequency of 25 Hz, a step increment of 5 mV, and an amplitude of 25 mV [17]. Before the next cycle, the electrode was cleaned at + 1.0 V for 200 s to remove the residual Hg under stirring condition. A series of SWV scanning was also performed to confirm the complete removal of any residual mercury until the stripping peak current disappeared [105] [17].

Similarly, the 1T-WS_2 modified GCE was immersed into a 0.1 M acetate buffer solution containing different concentrations of Hg^{2+} under optimized experimental conditions. The preconcentration (deposition) of Hg^{2+} was conducted at - 0.4 V for 450 s. Then the stripping response was obtained using square wave voltammetry from - 0.4 V to + 0.7 V with a frequency of 15 Hz, a step increment of 4 mV, and an amplitude of 25 mV. Before the next cycle, the electrode was cleaned at + 0.7 V for 120 s to remove the residual Hg under stirring condition [137].

3.3.3 Cyclic Voltammetry and Electrochemical Impedance Spectroscopy

CV and EIS were carried out for measuring the electrochemical performance of the modified electrodes using a Versa STAT 3 electrochemical potentiostat with a three-electrode system. For cyclic voltammetry, the applied voltage at the working electrode was scanned from - 0.2 V to + 0.6 V at a scan rate of 50 mV/s. Each CV was recorded for at least 5 cycles. Figure 3.9 shows the schematic diagram of the electrochemical set up used for CV and EIS measurements. The EIS measurements were performed under 10 mV AC voltage with a frequency varied from 0.01 Hz and 100 kHz at 0 V of open-circuit voltage.

3.4 Materials and Device Characterization

3.4.1 Raman Spectroscopy

Raman spectrum was obtained using a HORIBA Scientific model LABRAM HR 800. The Raman spectrum was recorded by exciting a green laser (532.04 nm). Figure 3.10 shows the schematic diagram of a typical Raman spectrometer while Figure 3.11 shows the experimental setup for a LABRAM HR Raman spectrometer. Before measurement, the

camera is turned ON along with the white light source. The sample surface is focused by moving the horizontal position of the sample stage and vertical movement of the microscope and a spot on the sample surface is selected for imaging. To focus the sample, an objective lens with three different magnifications such as 10x, 50x, 100x was utilized. Two different optical gratings of 300 and 1800 were used along with and 0.2 filters were adjusted. Then the camera and white light source are turned OFF. After that, the green laser is turned ON and the range of Raman shift wavenumbers from 200 to 2000 cm^{-1} are selected for scanning and the Raman spectrum is recorded under dark to avoid the interference from room light.

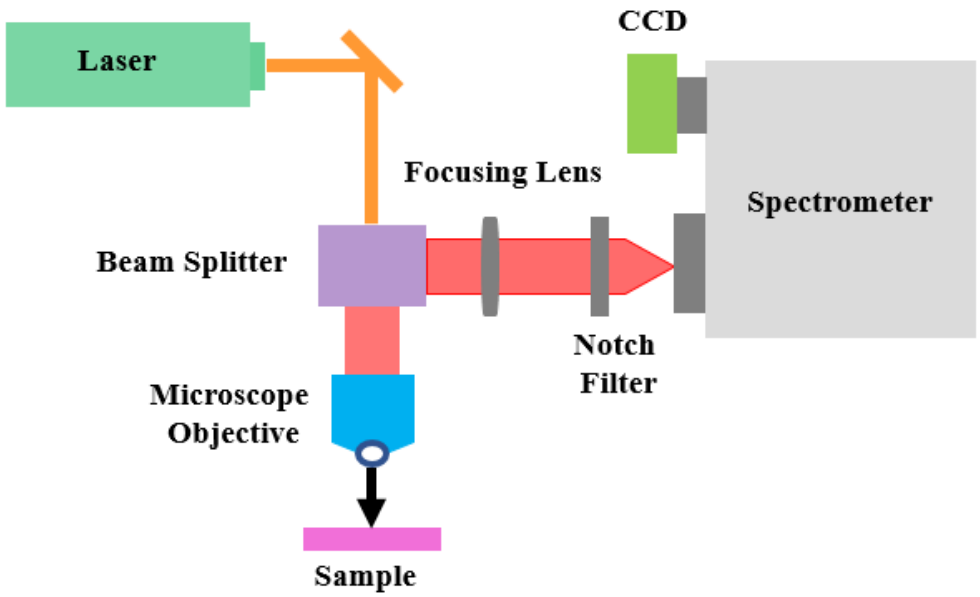

Figure 3.10 Schematic diagram of a typical Raman spectrometer.

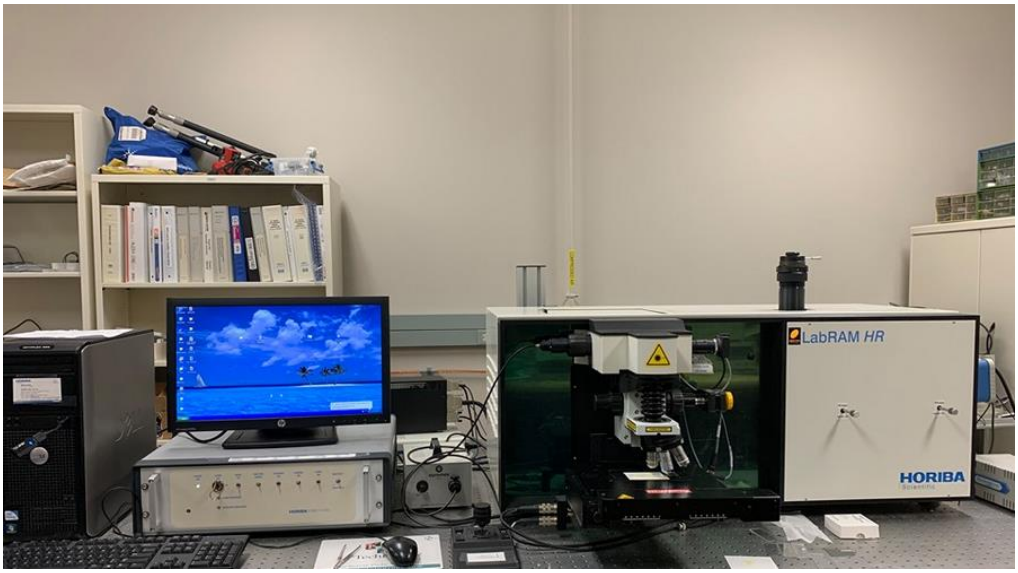

Figure 3.11 Experimental setup for a LABRAM HR Raman spectrometer.

3.4.2 X-ray Diffraction

To study the structural properties of AgNWs and WS_2 samples, a Rigaku SmartLab XRD was utilized with Cu Kα radiation at 40 kV and 44 mA. The diffraction angle (2θ) was scanned from 5° to 80° with a scan rate of 0.02° per second. Initially, the power button of the XRD instrument is turned ON and the X-ray generator tube voltage and current are ramped to 40 kV and 44 mA, respectively. The cavity of the glass sample plate is filled with WS_2 powder and the sample plate is mounted on the sample holder. For the measurement of thin film, a similar procedure was followed except a different optics and sample alignment was used. The thin film of AgNWs was prepared by spin coating of AgNWs dispersion on a glass substrate at 2000 rpm for 30 s with air drying for 20 min. Figure 3.12 shows the experimental set up for a Rigaku Smart Lab X-ray Diffractometer.

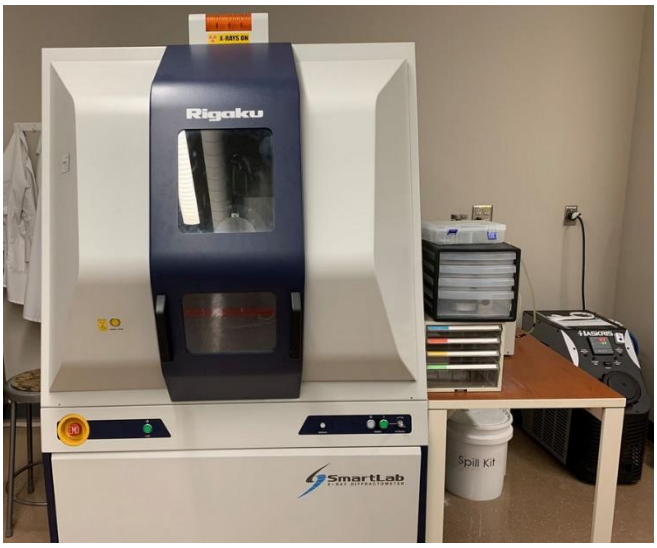

Figure 3.12 A Rigaku Smart Lab X-ray Diffractometer

3.4.3 Scanning Electron Microscopy

A Hitachi S-4700 SEM with EDS was used for the morphology and elemental characterization of test samples (Figure 3.13). The morphology of various samples was examined through SEM. To fabricate the sample for SEM, initially GO was spin-coated on a clean silicon wafer at 2000 rpm for 30 s and dried under air for 20 min. Similarly, AgNWs and GO-AgNWs composite dispersions were spin-coated on a silicon wafer and air-dried. To prepare the powder sample of 1T-WS_2, a very tiny amount of WS_2 powder was put on carbon tape and the excess amount was blown away with nitrogen. A 10 nm layer of gold was sputtered on top of GO, AgNWs and GO-AgNWs film. A high voltage of 5 kV, 10 kV, and 20 kV with a filament current of 134 mA was used for SEM imaging. Different magnifications of 5.0 k, 10.0 k, 25.0 k, 50.0 k were used for clear observation of the morphology. For EDS measurement, the same samples were used. The elemental mapping

was recorded using Aztec software (Oxford Instruments). In addition, the EDS spectrum shows the atomic percentage and weight percentage of each element.

Figure 3.13 Hitachi S-4700 scanning electron microscope.

CHAPTER 4 RESULTS AND DISCUSSION

4.1 Graphene Oxide-Silver Nanowires Composite Based Electrochemical Sensor for Hg^{2+} Detection

4.1.1 Sensing Mechanism of Hg^{2+} and Role of AgNWs

Figure 4.1 illustrates the steps in fabricating the electrochemical sensor and sensing mechanism for Hg^{2+} detection. The carboxylic group (-COOH) in GO can selectively bind Hg^{2+} ions due to its strong affinity towards Hg^{2+} by forming a stable R-COO-Hg^{2+}-COO-R linkage [120]. The Hg^{2+} ions were deposited (preconcentrated) onto the GO-AgNWs composite modified Pt electrode by an initially applied negative voltage (- 0.4 V for 500 s). Square wave voltammetry was carried out subsequently to oxidize (anodic stripping) the absorbed mercury [17]. The resulting current signal shows a peak which is proportional to the concentration of mercury ions. The peak potential is unique for mercury ions. The combination of peak potential and peak intensitiy are used to determine target mercury ions in water.

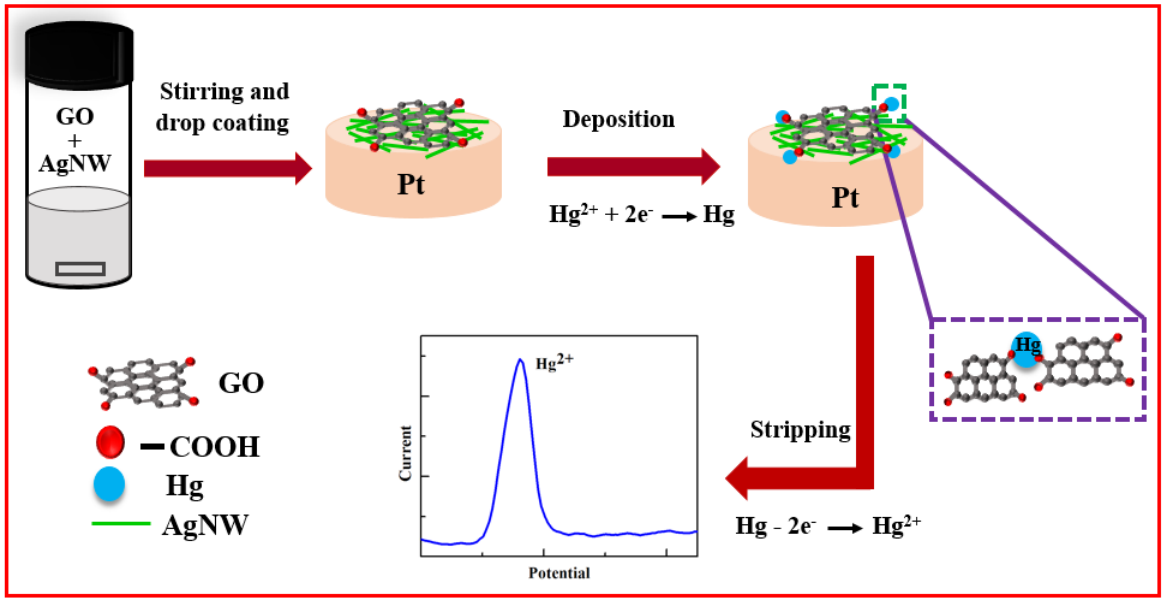

Figure 4.1 Sensing mechanism of GO-AgNWs composite modified electrochemical sensor for Hg^{2+} detection.

It is essential to get fast electron transport between the Pt electrode and Hg^{2+} to improve the sensitivity of electrochemical sensors. In this work, AgNWs have been employed to increase the conductivity of GO by making conduction pathways between GO sheets and Pt electrode. This phenomenon has been illustrated in Figure 4.2. Initially, the Hg^{2+} ions were deposited on the surface of GO by an initially applied negative voltage (-0.4V for 500s) and the negatively charged carboxylic group (-COOH) on GO. The AgNWs accelerate the conduction of necessary electrons for the deposition (reduction reaction) of Hg^{2+} ion. After that, the stripping of the adsorbed mercury was performed by square wave voltammetry where the AgNWs provide faster transport of released electrons from GO to the Pt electrode (shown by red arrows). The rapid charge (electron) transfer during the deposition and stripping of Hg^{2+} through AgNWs helps to achieve high sensitivity and lower LOD [17].

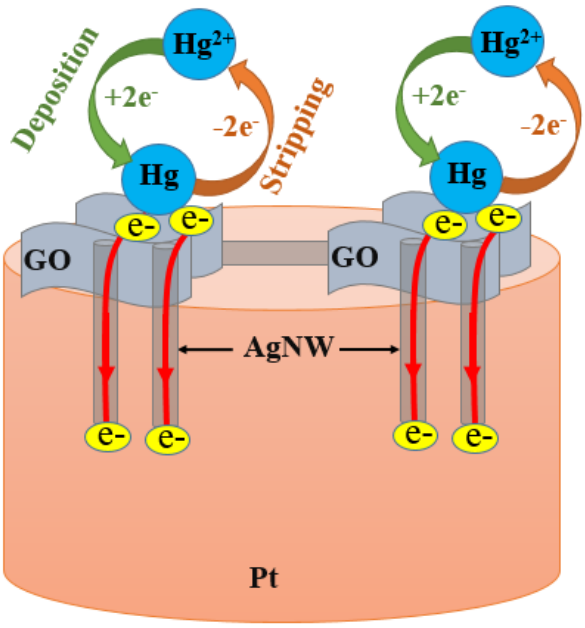

Figure 4.2 Electron transfer phenomenon through AgNWs from GO to Pt electrode during the deposition and stripping of Hg^{2+}.

4.1.2 Morphological and Structural Characteristics

The morphology of the GO and silver nanowires and their composite were analyzed through SEM. Figure 4.3 shows a low magnification (5.00 kx) SEM image of AgNWs, where AgNWs are overlapped each other and few of them are aggregated. Figure 4.4a-b shows high magnification images (25.00 kx and 50.00 kx) of AgNWs. It can be observed that the AgNWs are dispersed and separated from each other with a uniform diameter and length. The diameter and length of AgNWs are approximately 50-100 nm and 8-15 µm, respectively [17].

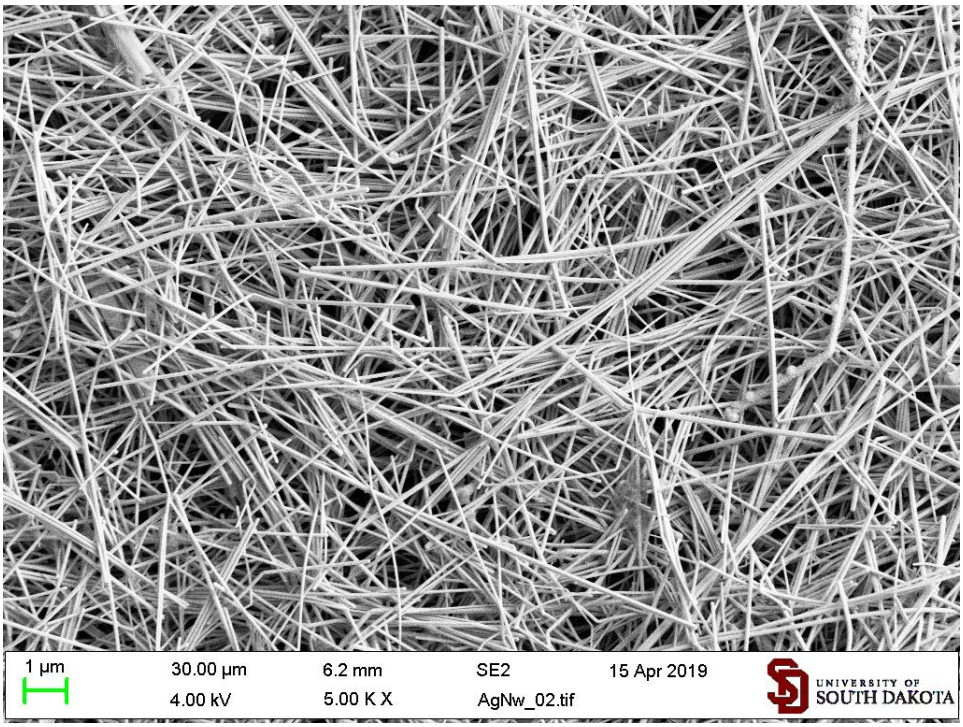

Figure 4.3 SEM images of AgNWs at low magnification (5.00 kx).

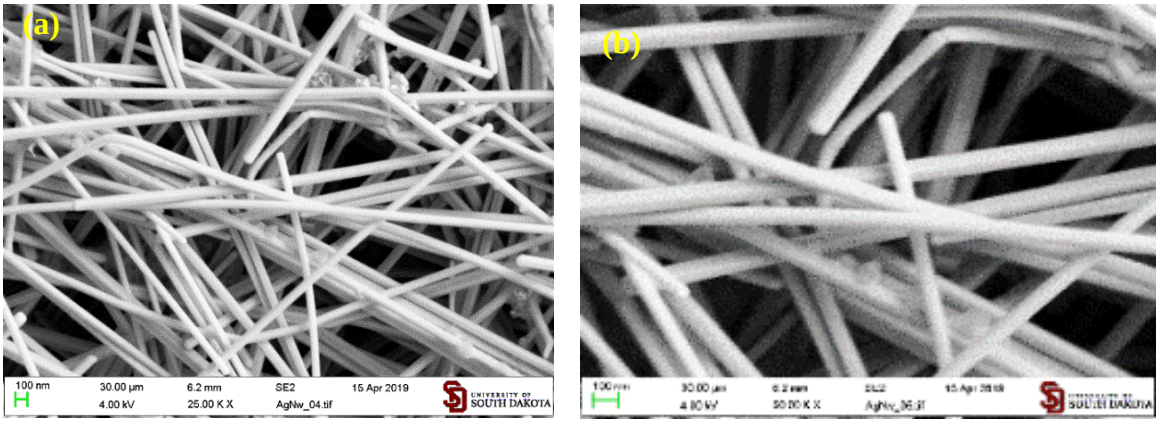

Figure 4.4 SEM images of AgNWs at high magnification (a) 25.00 kx (b) 50.00 kx.

The agglomeration of graphene sheets was observed on the SEM image of GO. A few thin wrinkles on the surface of GO sheets were also observed and shown in Figure 4.5. The reason for the can be ascribed to The π-π interactions between individual layers of graphene sheets can cause the agglomeration of GO [17]. The incorporation of AgNWs on

GO sheets produces a hybrid network which was observed in Figure 4.6. Here, AgNWs acts as a connecting bridge between GO sheets by forming a hybrid network and reduces the aggregation of GO sheets. The reason behind this phenomenon can be the electrostatic interaction between negatively charged GO sheets and positively charged AgNWs [17].

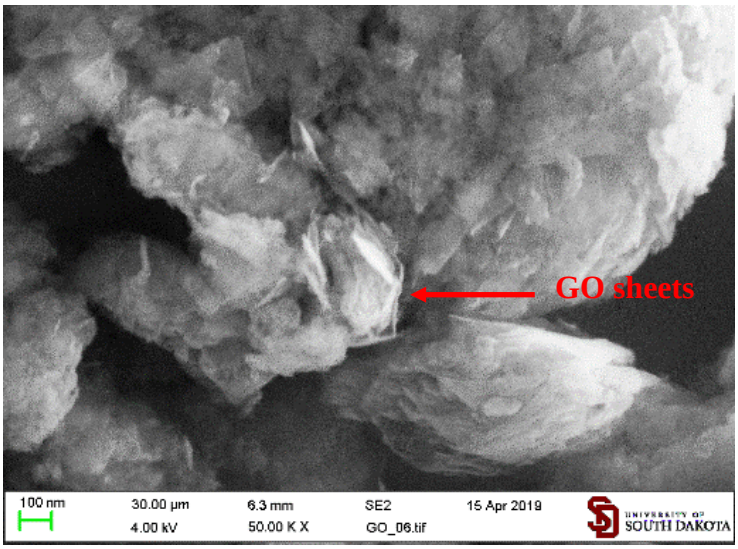

Figure 4.5 SEM images of GO sheets showing an agglomeration of nanosheets.

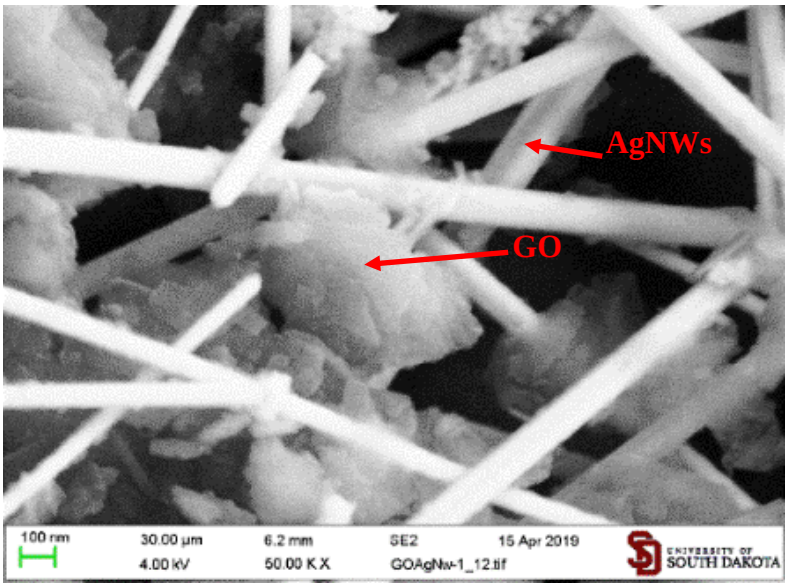

Figure 4.6 SEM images of a hybrid network of GO-AgNWs composite.

The elemental mapping of GO-AgNWs composite was investigated by conducting energy-dispersive X-ray spectroscopy (EDS). Figure 4.7b-d shows the corresponding mapping of GO-AgNWs composite. Homogenous distribution of C and O were observed on elemental mapping with Ag was distributed on nanowires that represents the formation of the composites. The EDS spectrum of GO-AgNWs composite was shown in Figure 4.8. It was found that the weight percentage of C, O, and Ag in the GO-AgNWs composites were 80.4%, 9.1%, and 10.5%, respectively, which represents the purity of GO-AgNWs composites [17].

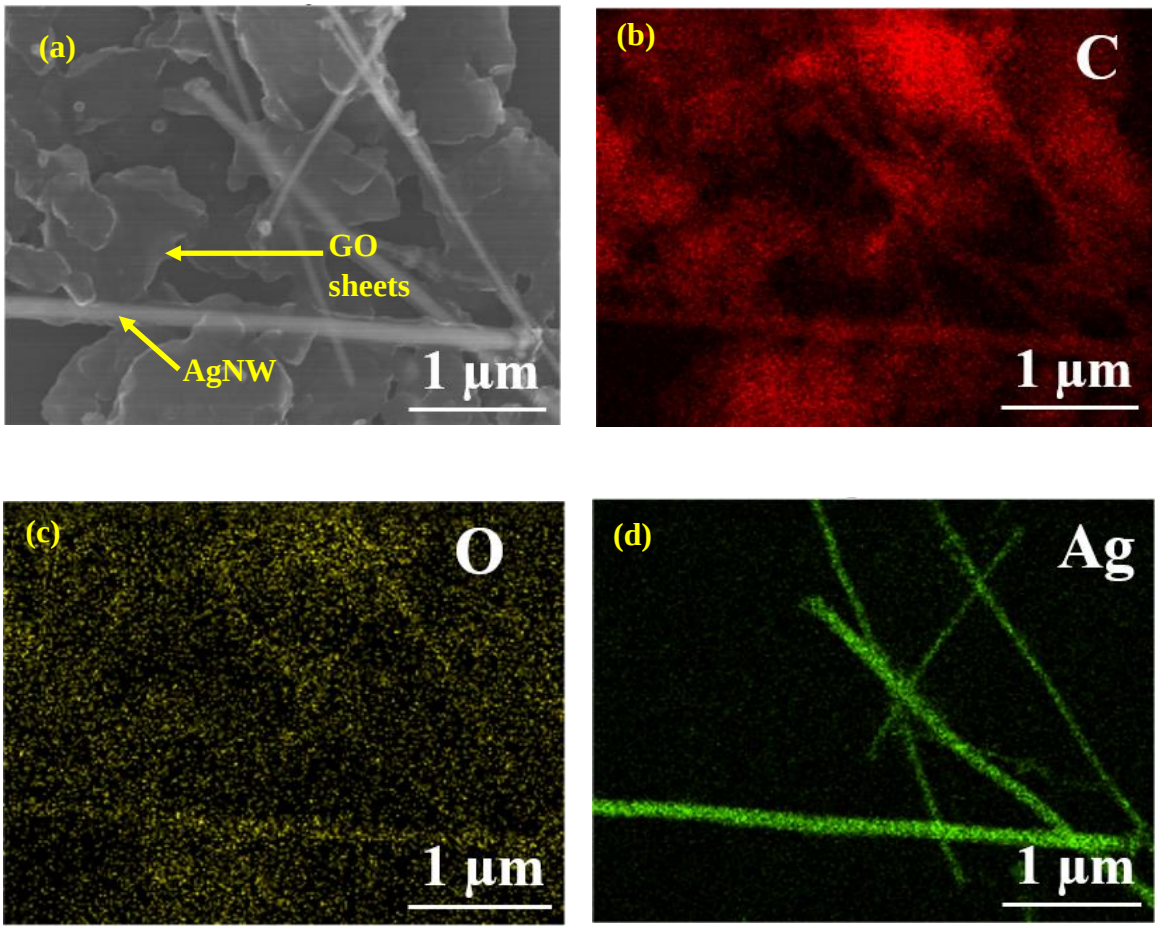

Figure 4.7 (a) SEM image of the GO-AgNWs composite and corresponding quantitative EDS element mapping of (b) C (c) O and (d) Ag.

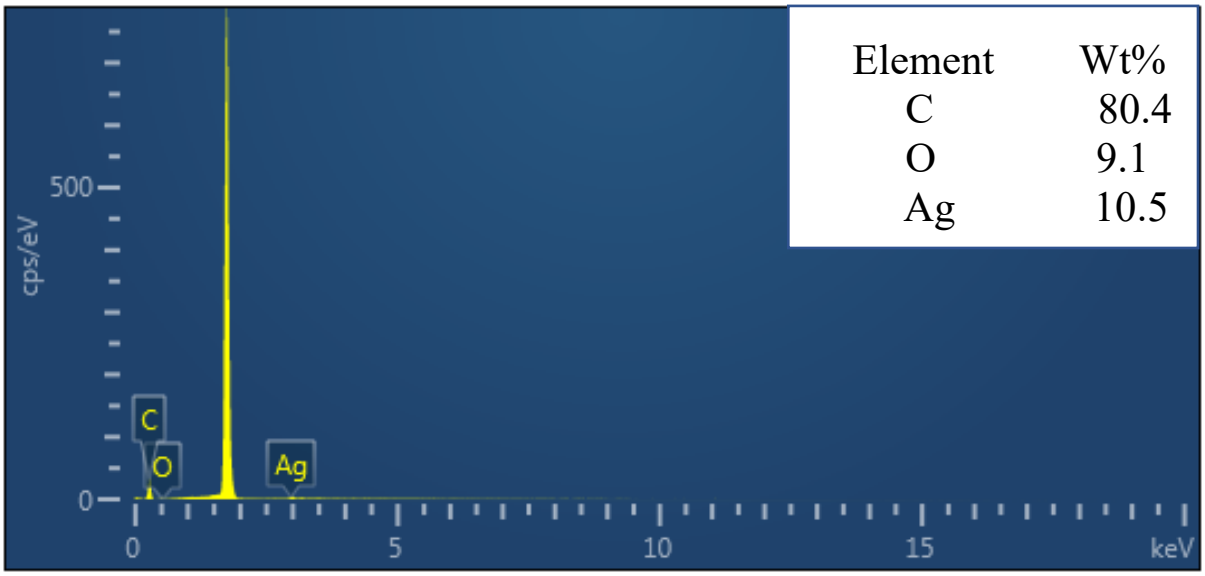

Figure 4.8 The EDS spectrum of the GO-AgNWs composite deposited on Si substrate.

Figure 4.9a-b shows low magnification and high magnification TEM images of GO sheets. Single-layer or few layers of exfoliated graphene sheets can be observed on the TEM images of GO. The observed edges on the GO sheets demonstrate the flexible and ultra-thin nature of graphene sheets. The light-colored and homogenous areas on GO sheets indicate the single-layer graphene sheet, while the relatively dark areas on GO sheets indicate the multiple graphene sheets due to the agglomeration [169, 170]. Figure 4.9 c-d shows the low magnification and high magnification TEM images of the GO-AgNWs composite. An overlapping of AgNWs on GO sheets was observed which formed a hybrid network of GO-AgNWs and AgNWs may provide conducting path for electrons through the GO sheets [17].

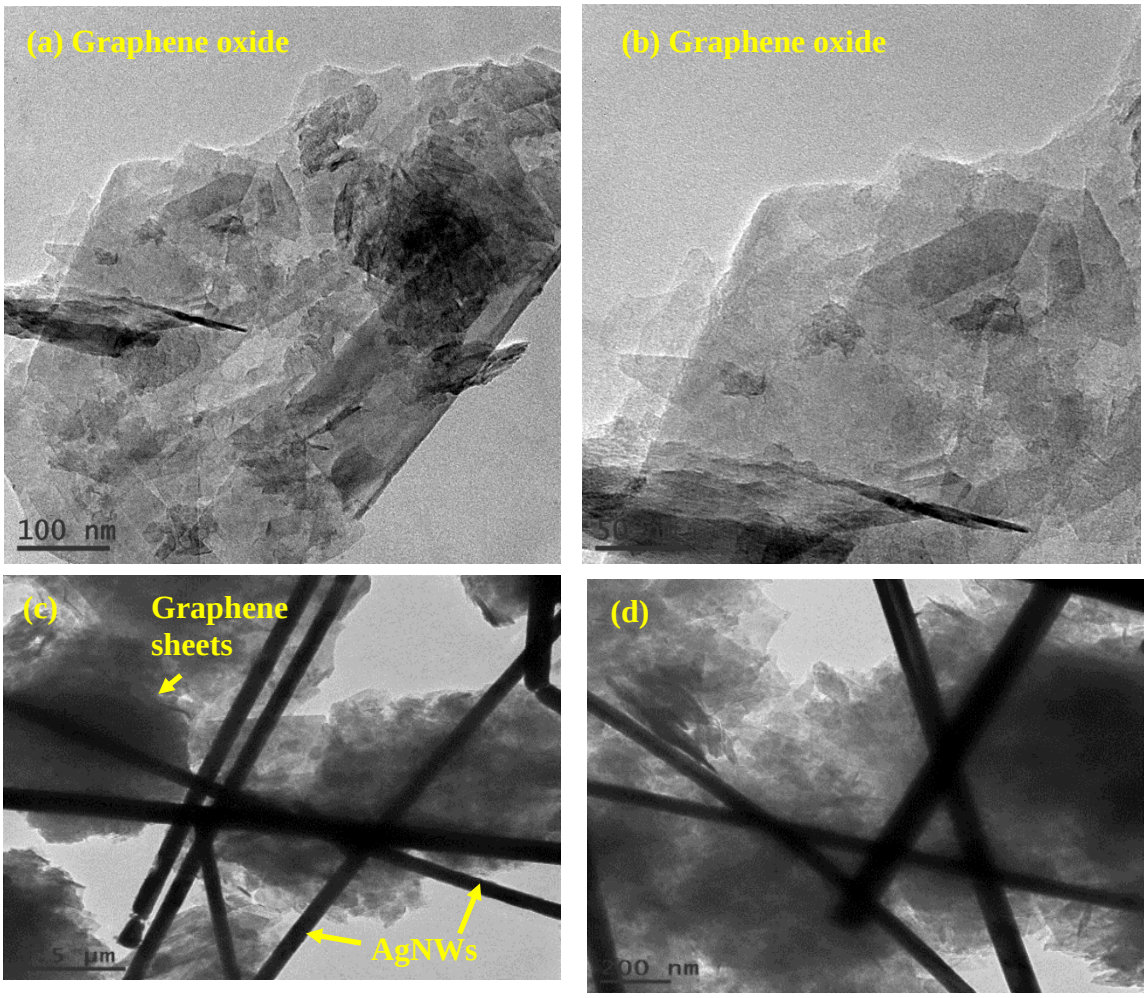

Figure 4.9 TEM image of the GO (a) low magnification image (b) high magnification image (c) Low magnification and (d) high magnification images of GO-AgNWs composite.

The interaction between GO and AgNWs was explained by the zeta potential measurement. Zeta potential measures the surface charge of nanoparticles in the colloidal dispersion. The value of zeta potential varies from + 100 mV to - 100 mV. A negative zeta potential implies negatively charged particles and a positive zeta potential implies positively charged particles. The stability of a colloidal solution can be estimated from the magnitude of the zeta potential [171] [17].

GO sheets become negatively charged due to the oxygen-containing functional groups including carboxyl (-COOH) and hydroxyl (-OH). This is supported by the zeta potential measurement of - 26.39 mV (Figure 4.10a) which represents the negatively charged GO sheets. On the other hand, the zeta potential for AgNWs was found as + 0.64 mV (Figure 4.10b), which represents the positively charged AgNWs. An electrostatic interaction will occur between negatively charged GO sheets and the positively charged AgNWs, which results in the formation of a stable colloidal dispersion of GO-AgNWs composite [172] [17].

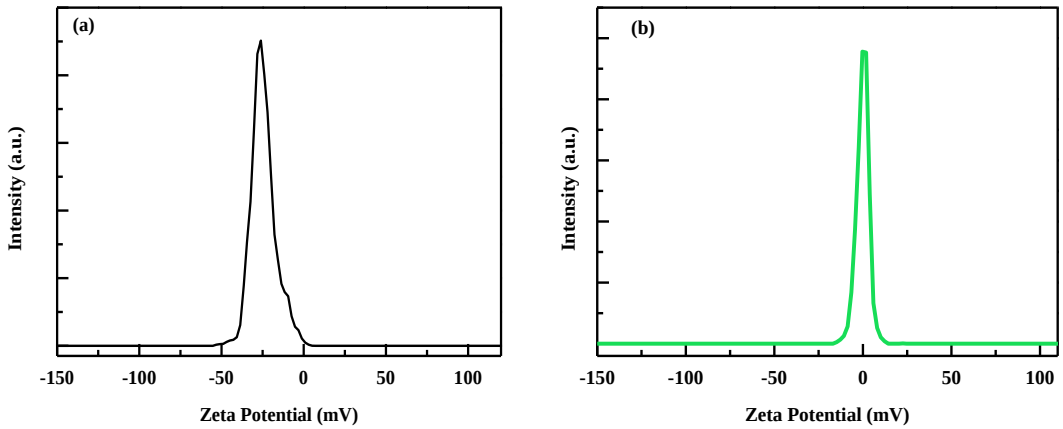

Figure 4.10 The zeta potentials of (a) GO and (b) Ag NWs dispersions in deionized water.

The structural characterization of GO, AgNW, and GO-AgNWs composite was carried out by performing Raman spectroscopy shown in Figure 4.11. Two characteristic peaks were observed on the Raman spectra of GO which are corresponding to the D band and G band, respectively. The D bands at 1343.36 cm^{-1} and 1567.26 cm^{-1} can be attributed to the sp^3 hybridized carbon and first-order scattering of the E_{2g} phonon of the sp^2 carbon lattice, respectively [115, 162, 163]. A prominent peak for AgNWs was observed at 987.63

cm^{-1}. The observation of all the corresponding peaks on the Raman spectra for GO and AgNWs confirms the successful formation of GO-AgNWs composite [17].

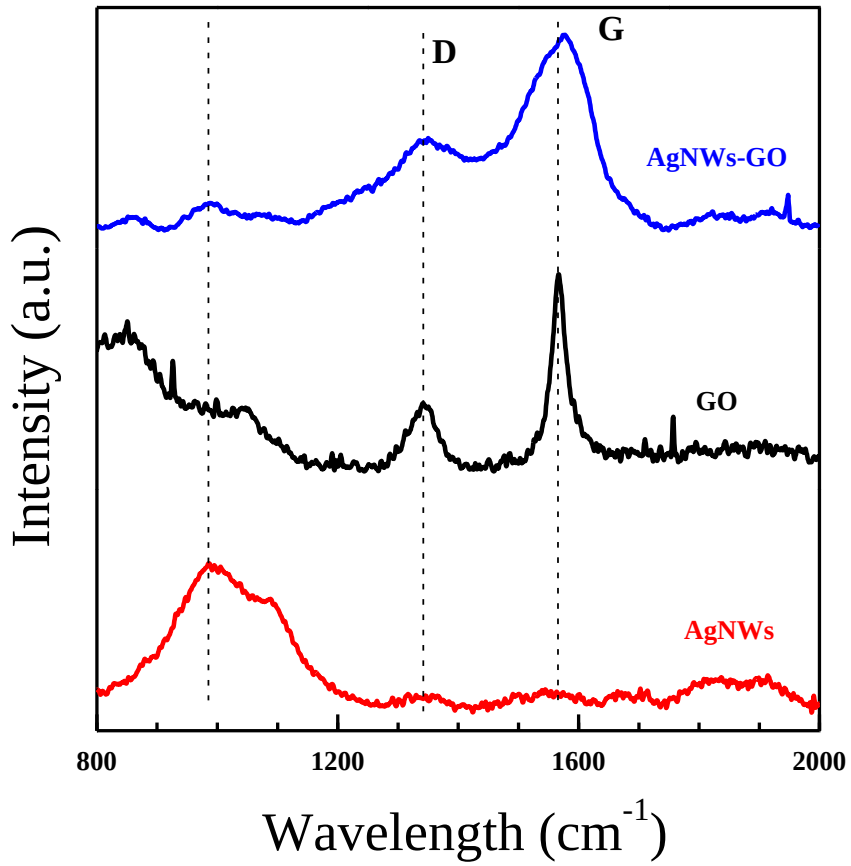

Figure 4.11 Raman spectra of GO, AgNW, and GO-AgNWs composite.

X-ray diffraction (XRD) was performed to analyze the crystal structure with a thin film of AgNWs deposited on a glass slide. The corresponding XRD for AgNWs was shown in Figure 4.12. Two characteristics diffraction peaks observed at 38.2 and 44.4 confirms the formation of AgNWs and can be ascribed to the (111) and (200) planes of face-centered cubic silver, respectively, which is supported by previous reports [173, 174] [17].

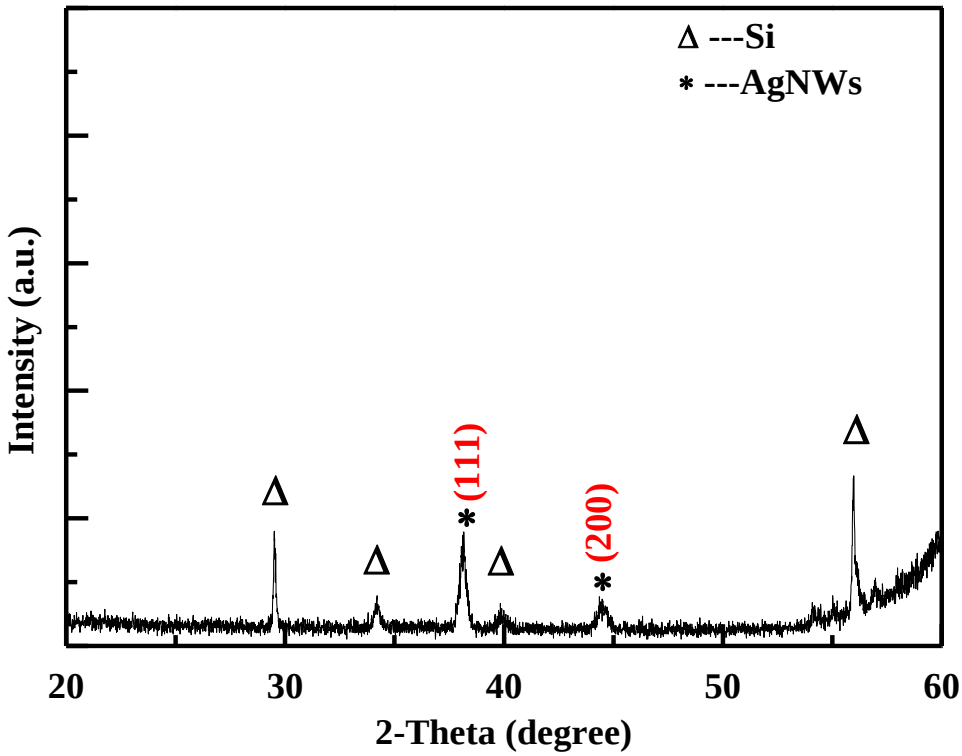

Figure 4.12 XRD patterns of AgNWs.

4.1.3 Electrochemical Characterization of Different Electrodes

The electron transfer properties of GO, AgNW, and GO-AgNWs composite modified Pt electrodes were studied by EIS. Figure 4.13 shows the EIS results for GO, AgNW, and GO-AgNWs composite modified Pt electrodes. It can be seen that Nyquist plots contained a semicircle at higher frequencies corresponding to the electron-transfer-limited process and a straight line at lower frequency indicating the diffusion-limited process [153]. The diameter of the semicircle represents the charge transfer resistance (R_{ct}) of the electrode-electrolyte interface. The semicircle for GO-AgNWs composite modified Pt electrode (curve iii) exhibited a R_{ct} value of 460.3 Ω, which is much lower than the GO electrode only with ~ 812.6 Ω (curve i). This implies that the presence of AgNW in GO-

AgNWs composite enables the enhancement of electron transfer kinetics which is expected to improve sensor response. The AgNWs modified Pt electrode (curve ii) had a R_{ct} value of 396.3 Ω.

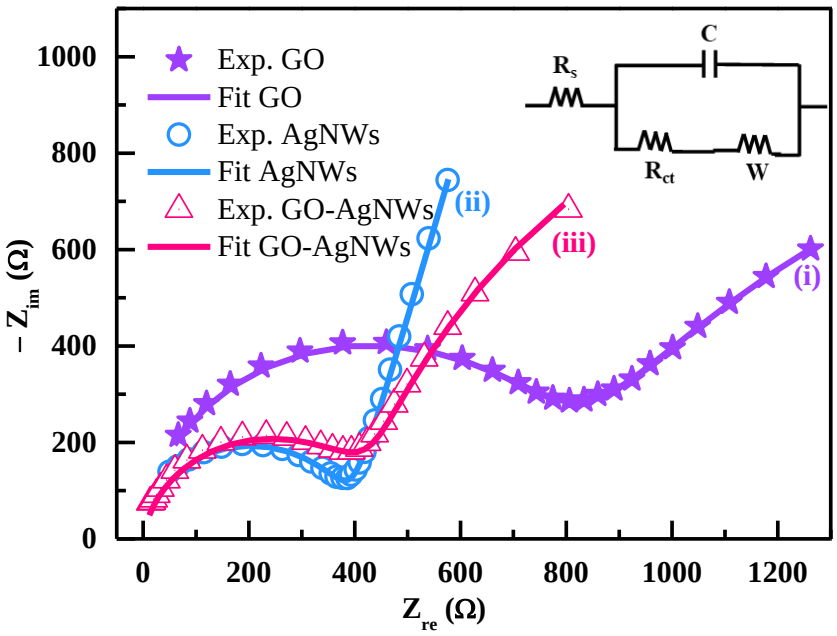

Figure 4.13 Nyquist plots for different electrodes in 5 mM $K_3Fe(CN)_6$ aqueous solution containing 0.1 M KCl (i) GO modified Pt, (ii) AgNWs modified Pt, and (iii) GO-AgNWs composite modified Pt electrode. The inset is the equivalent circuit used to model impedance data.

Figure 4.14 reveals the cyclic voltammograms of different modified electrodes in 5.0 mM $K_3[Fe(CN)_6]$ containing 0.1 M KCl solution. On bare GO, a pair of weak redox peaks (10μA) was observed, indicating the sluggish electron transfer rate at the electrode-electrolyte interface [175]. This can be attributed to the low conductivity of GO due to the presence of different oxygen-containing functional groups which block the diffusion of $Fe(CN)_6^{3-/4-}$ to the electrode surface and hinder the electron and mass transfer [7]. The

AgNWs modified electrode showed the highest peak current of around 31 µA, which can be attributed to the high conductivity of AgNWs. The anodic and cathodic peak current of about 22 µA for the GO-AgNWs composite modified Pt electrode was higher than GO only modified electrode and less than AgNWs modified electrode [17]. AgNWs may provide the necessary conduction pathways on the electrode surface, accelerating the electron transfer process [17].

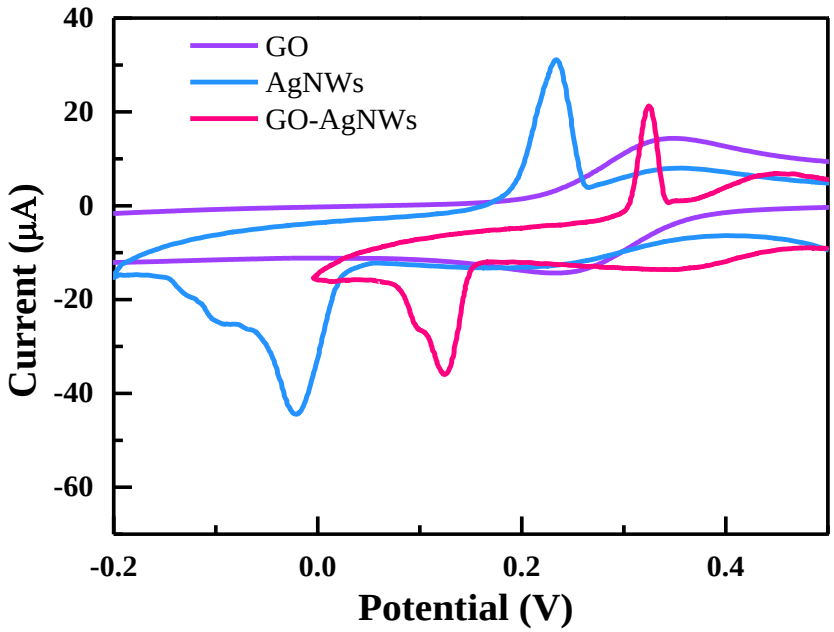

Figure 4.14 CV of different modified electrodes in 5.0 mM $K_3[Fe(CN)_6]$ solution containing 0.1 M KCl.

Figure 4.15 shows the square wave voltammetry response for GO, AgNWs, and GO-AgNWs composite modified Pt electrodes. There was no stripping peak current in the AgNWs modified Pt electrode. A small stripping peak at around + 0.16 V was observed for the GO modified Pt electrode because the carboxylic group (-COOH) in GO can selectively bind Hg^{2+} ions as R-COO-Hg^{2+}-COO-R [113]. The stripping peak current of

the GO-AgNWs composite modified Pt electrode was enhanced nearly 3.5-fold (about 60 μA) of that of the GO modified Pt electrode, indicating the synergistic effect of AgNWs and GO [17].

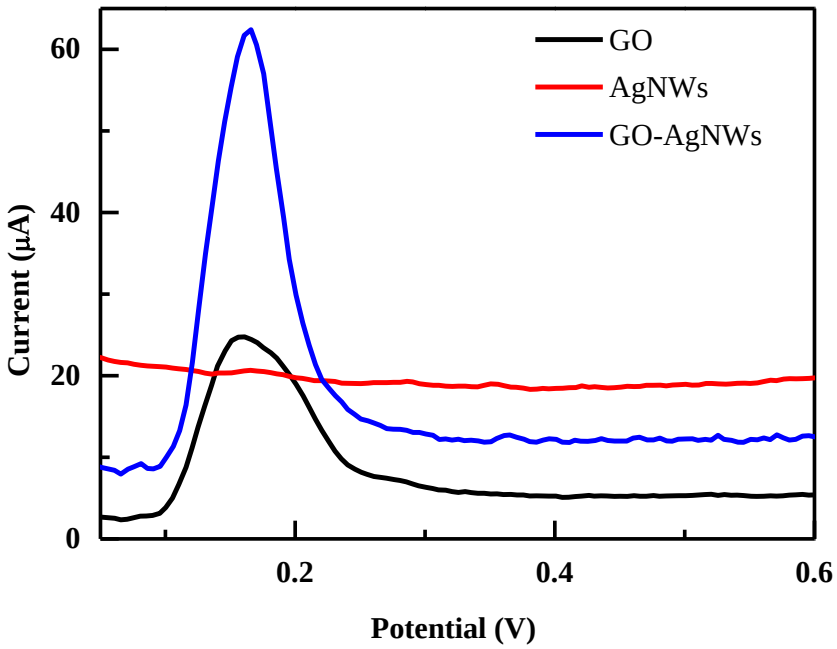

Figure 4.15 SWASV responses for Hg^{2+} determination at GO, AgNWs, and GO-AgNWs modified Pt electrodes.

4.1.4 Optimization of Experimental Conditions

To get a high performance stripping analysis of Hg^{2+}, the experimental parameters including deposition potential and time were optimized. Figure 4.16 showed the influence of deposition potential on the stripping peak current responses for Hg^{2+}. Starting from - 0.1 V vs Ag/AgCl, the stripping peak current showed a significant increase as the deposition potential decreased to -0.40 V. The maximum stripping peak current was observed at -0.40 V, indicating the most reduction of Hg^{2+}. However, the stripping peak current was reduced

when the deposition potentials were more negative than - 0.40 V. This phenomenon can be attributed to the increase of hydrogen evolution at more negative potentials [176]. Therefore, a deposition potential of - 0.40 V was chosen as optimum for Hg^{2+} [17].

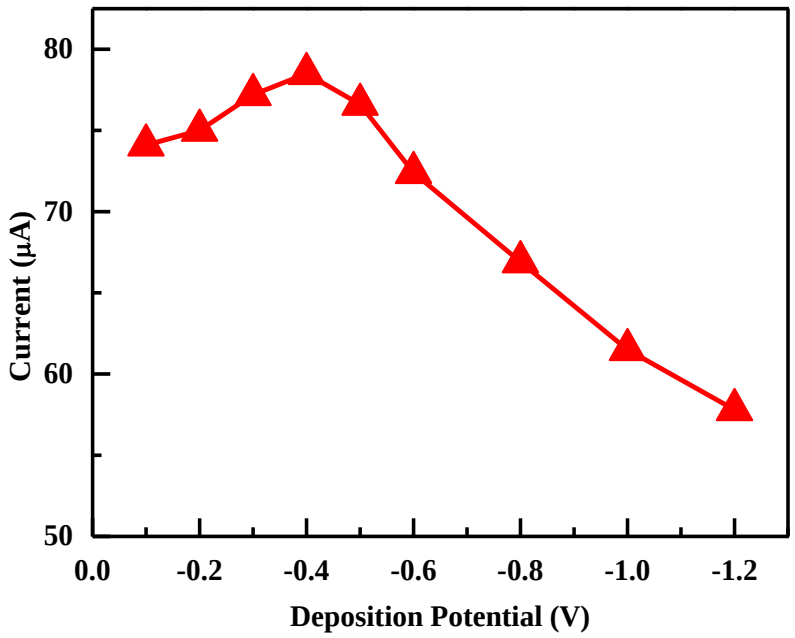

Figure 4.16 The effect of deposition potential on the stripping peak current for 1μM Hg^{2+} at GO-AgNWs composite modified Pt electrode.

The accumulation of metal ions onto the electrode surface is affected by the amount of deposition time, which can further affect the stripping peak currents for the detection of Hg^{2+}. The effect of deposition time in the range of 50-700 s on the stripping peak current responses for Hg^{2+} was studied. Figure 4.17 depicts the stripping peak currents of Hg^{2+} as a function of deposition time at - 0.40 V for the GO-AgNWs composites modified Pt electrode. The stripping peak current increased rapidly during the deposition time from the 30 s to the 200 s. After that, the stripping peak current increased gradually from 300 s to 500 s until it reaches steady. At deposition time greater than 500 s, the stripping peak

current became saturated, which was probably due to saturation of available active sites for the Hg^{2+} deposition on the GO-AgNWs composite modified Pt electrode surface. Therefore, the optimized deposition time of 500 s was chosen for all the experiments [17].

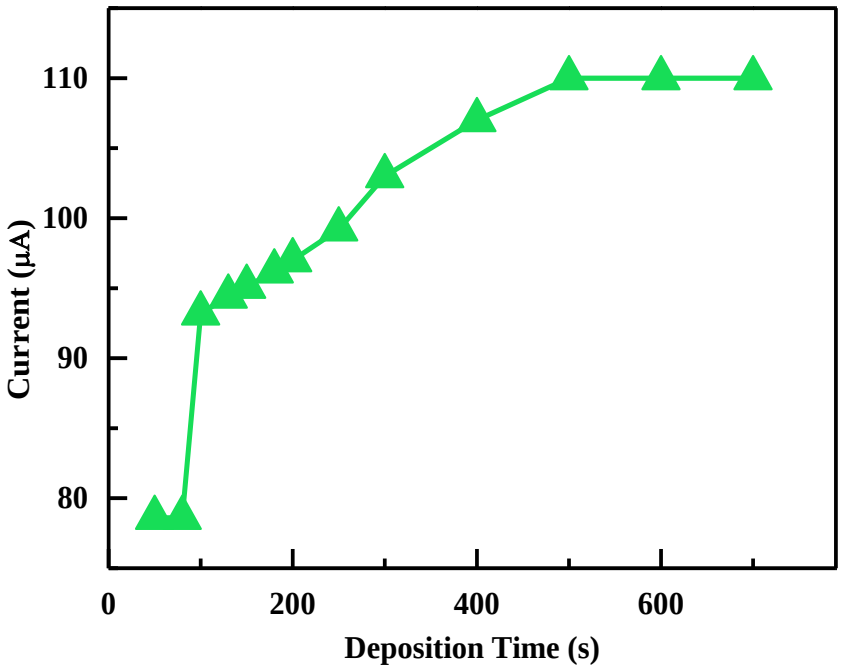

Figure 4.17 The effect of deposition time on the stripping peak current for 1μM Hg^{2+} at GO-AgNWs composite modified Pt electrode.

The effect of different weight ratios of GO to AgNWs in the composite on sensing performance of detecting Hg^{2+} is shown in Figure 4.18. The peak current towards 50 nM Hg^{2+} was maximum (~59 μA) for the optimized weight ratio of 1 (GO:AgNW = 1:1). It can be attributed to the formation of a hybrid network between AgNWs and graphene sheets, which is also supported by SEM and TEM. On the other hand, the peak current significantly decreased to ~ 45 μA for the weight ratio of 0.5 (GO: AgNWs = 1:2). The associated reason may be the increase of inter-nanowire junction resistance between

AgNWs due to the aggregation. When the weight ratio was increased to 2 (GO: AgNWs = 1:0.5), the peak current of ~52 µA was obtained which is attributed to the lack of sufficient electron conduction pathways. Therefore, the weight ratio of 1 was found to be optimum [17].

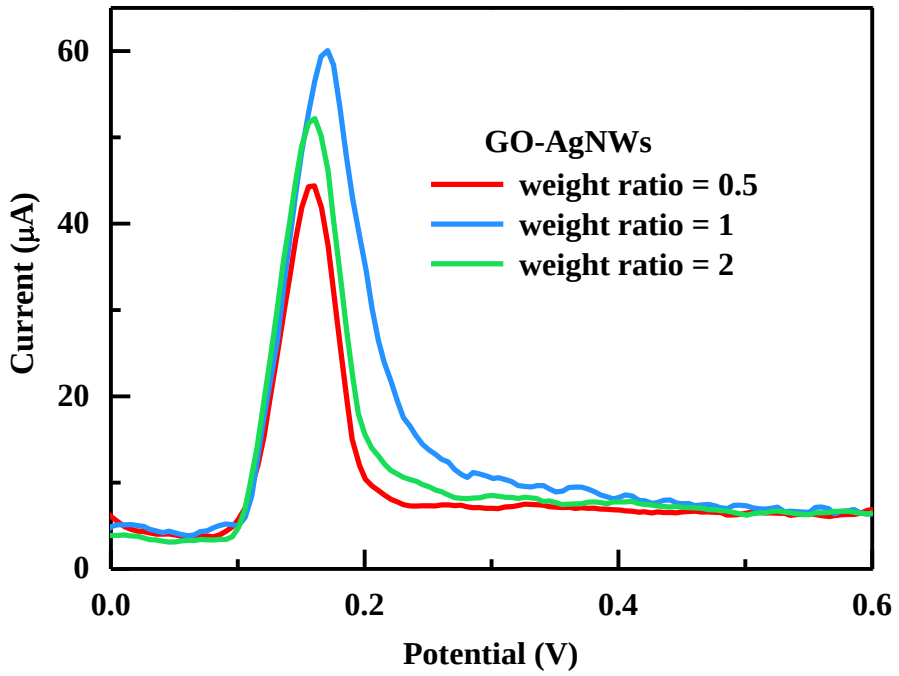

Figure 4.18 SWASV responses for Hg^{2+} determination at three different weight ratios of GO-AgNWs composite modified Pt electrodes.

4.1.5 Detection of Hg^{2+} Using GO-AgNWs Composite Modified Electrodes

Figure 4.19a illustrates the SWASV responses of the GO-AgNWs composite modified Pt electrode at various Hg^{2+} concentrations in 0.1 M KCl under the optimized deposition potential of - 0.4 V and time at 500 s. The stripping peak currents increased with the increase of Hg^{2+} concentration. The peak current vs Hg^{2+} concentration followed a linear relationship over the range 1.0-70 nM with a correlation coefficient of 0.9947 (Figure

4.19b). The sensitivity of the sensor was ~ 0.29 µA/nM according to the slope of the linear curve. The detection limit (3σ/s, where σ and s are standard deviation and sensitivity, respectively) of the GO-AgNWs composite modified Pt toward Hg^{2+} was calculated to be ~ 0.1 nM, which is very well below the World Health Organization defined limit in drinking water [17].

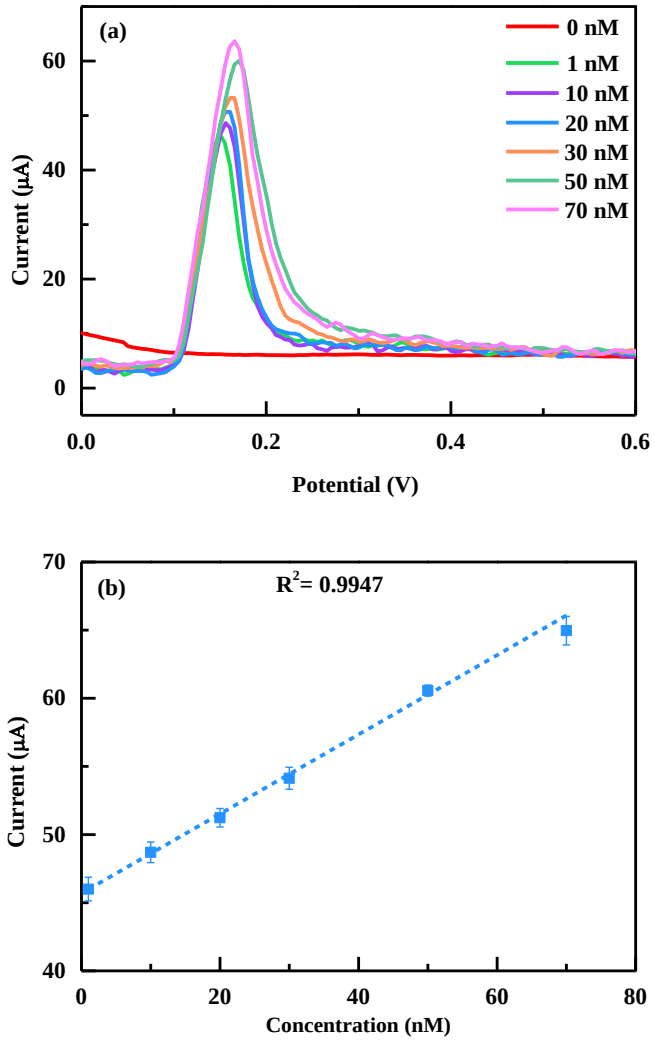

Figure 4.19 (a) SWASV response of the GO-AgNWs composite modified Pt electrode for Hg^{2+} with different concentrations (b) The plot of the stripping peak current vs Hg^{2+}

concentration. The error bars represent the standard deviation for the mean of three replicate tests.

4.1.6 Selectivity, Repeatability, Reproducibility, and Stability

The possible interferences arising from various heavy metal ions including Pb^{2+}, Cd^{2+}, Cu^{2+}, Na^{+}, and Ag^{+} were studied under the optimum deposition potential and time to evaluate the selectivity of the GO-AgNWs composite modified Pt sensor. Figure 4.20 displays the stripping response of the Hg^{2+} sensor in the presence of a 10-fold concentration of each interfering agent in the solution for the target analyte. It was observed that the stripping peak current for 50 nM Hg^{2+} was almost the same, indicating that these metal ions had no significant interference effect on the detection of Hg^{2+}. It is well known that many metal ions can complex with the carboxylic group (-COOH). When two metal ions, both having affinity to -COOH group, the metal ion having higher reduction potential will be preferably reduced on the surface of GO by the -COOH group [81]. Thus, Hg^{2+} with its higher standard reduction potential (+ 0.85 V) shows more tendency to reduce over interfering Pb^{2+} (- 0.13 V), Cd^{2+} (- 0.40 V), Cu^{2+} (+ 0.34V), Na^{+} (- 2.71 V), and Ag^{+} (+ 0.80 V) [81]. Hence, the interfering ions will find it more difficult to bond with -COOH group and fewer of these ions will be adsorbed. This implies that Hg^{2+} will be easily adsorbed and reduced by -COOH of GO in the presence of interfering ions [17]. Since the standard reduction potential of Hg^{2+} (+ 0.85 V) is close to that of Ag^{+} (+ 0.80 V), a very small interference from Ag^{+} ion on the response of Hg^{2+}+Ag^{+} was observed. SWASV response of the GO-AgNWs composite modified Pt electrode for Hg^{2+}, $Ag^{+,}$ and Hg^{2+}/Ag^{+} mixture are shown in Figure 4.21. The selectivity of the sensor was tested for different metal ions shown in Figure 4.22. As observed, the sensor did not show obvious responses

to the interfering species studied that can be attributed to the strong affinity of -COOH toward Hg^{2+}.These results indicate the high selectivity of the sensor to Hg^{2+}.

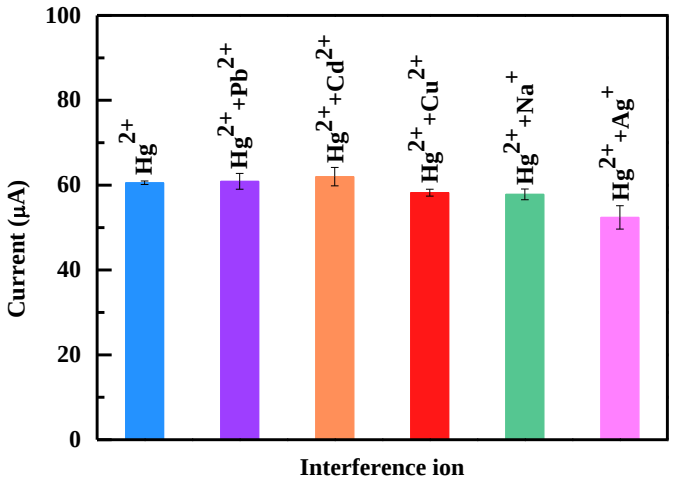

Figure 4.20 Interference effects of different metal ions on the stripping signals of Hg^{2+} at GO-AgNWs composite modified Pt electrode (50.0 nM Hg^{2+} and 500 nM each for Pb^{2+}, Cd^{2+}, Cu^{2+}, and Na^{+}). The error bars represent the standard deviation for the mean of three replicate tests.

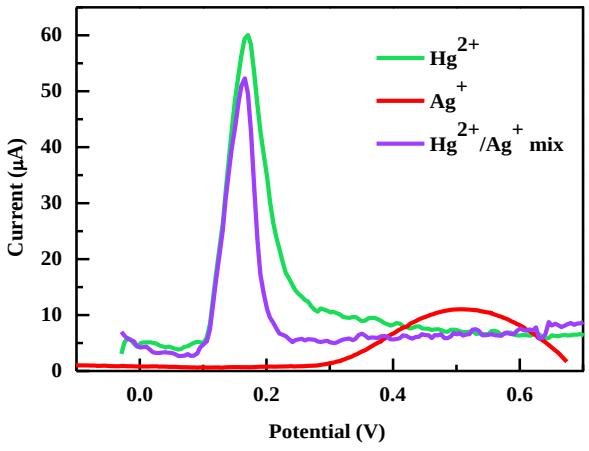

Figure 4.21 The SWASV response of the GO-AgNWs composite modified Pt electrode for Hg^{2+}, Ag^{+}, and Hg^{2+}/Ag^{+} mixture.

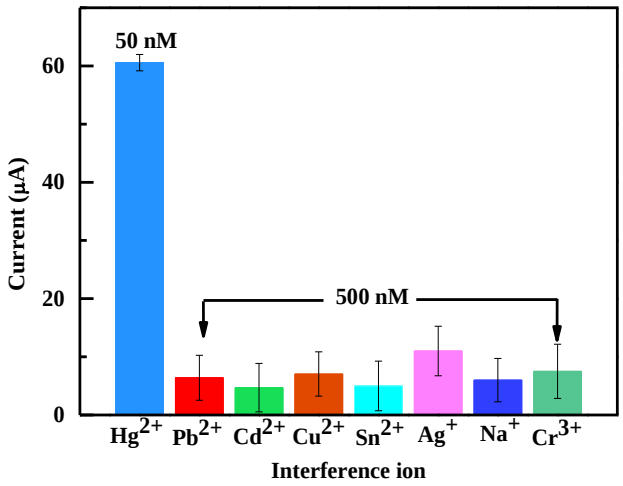

Figure 4.22 Selectivity test of GO-AgNWs composite modified Pt electrode against different metal ions. The concentration of Hg^{2+} was 50 nM and the others were 500 nM. The error bars represent the standard deviation for the mean of three replicate tests.

Repeatability of the sensor was studied after ten replicate tests for 10 nM Hg^{2+} under the optimum deposition potential and time with a single GO-AgNWs composite modified Pt sensor. As seen in Figure 4.23, the obtained stripping peak current towards Hg^{2+} for every test was almost identical except for a slight upward drift in the current. The reason for the slight drift may be the same sensor surface was not retained after stripping and deposition. In addition, different experimental conditions such as temperature, vibration, etc., may cause drift. However, the low Relative Standard Deviation (RSD) of peak current (3.01%) demonstrates the good repeatability of the sensor [17].

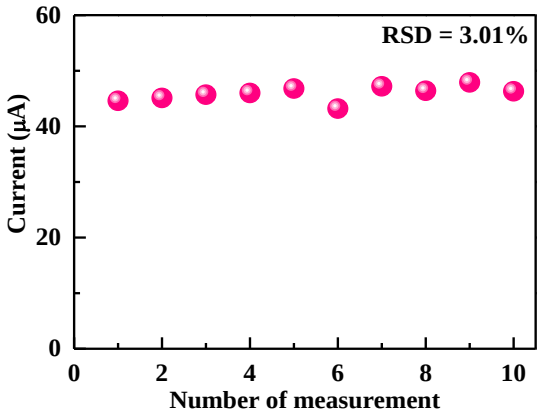

Figure 4.23 Repeatability study of GO-AgNWs composite modified Pt sensor in 0.1 M KCl containing 10 nM Hg^{2+} under optimum deposition potential and time. Data are obtained from every SWASV response.

The reproducibility of the GO-AgNWs composite modified Pt sensor was also tested with three different sensors prepared independently by the same procedure. Under the optimum deposition potential and time, the sensors were employed to detect 10 nM Hg^{2+} using SWASV. Figure 4.24 represents the SWASV response of the sensors, where the inset shows a histogram plot for peak current to different sensors tested. Three replicate tests were performed for each sensor. The low RSD of peak current (2.0%) demonstrates the good reproducibility of the sensor. The good repeatability and reproducibility of the GO-AgNWs composite modified Pt sensor make it promising for electrochemical detection of Hg^{2+} [17].

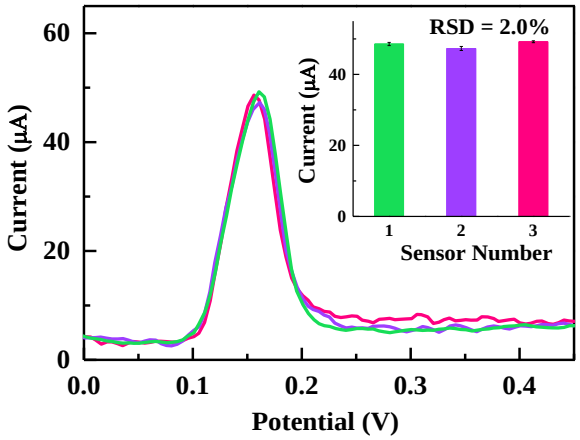

Figure 4.24 Reproducibility test carried out at 10 nM Hg^{2+} for three GO-AgNWs composite modified sensors. The inset shows a histogram plot for peak current for the three sensors. Error bars are obtained from three replicate tests.

To study the short-term stability of the GO-AgNWs composite modified Pt electrode, CV was performed over 10 cycles. Figure 4.25 shows the CV curves of the 1st, 5^{th}, and 10^{th} cycles. The overlapping of the three CV curves indicates that the GO-AgNWs composite modified Pt electrode shows good short-term stability. No depletion or falling-off the GO-AgNWs composite modified electrode was observed as is evident in Figure 4.26, which shows the photographs of the electrode after Hg^{2+} detection for 10 min as well as 20 min. This confirms that the GO-AgNWs composite is very stable with excellent adhesion property during the electrochemical measurement for Hg^{2+} detection [17].

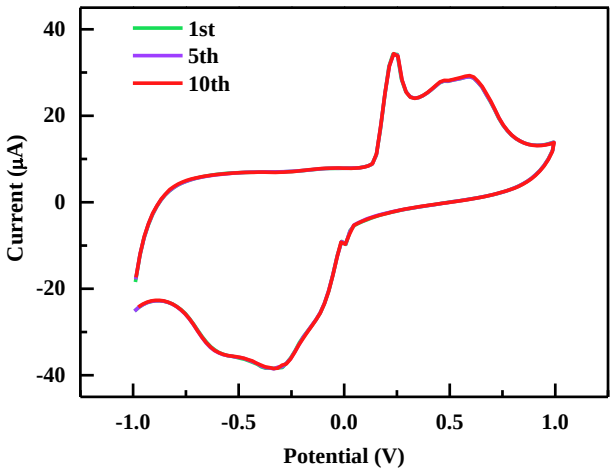

Figure 4.25 The CV curves showing the stability of the fabricated GO-AgNWs composite modified Pt electrode.

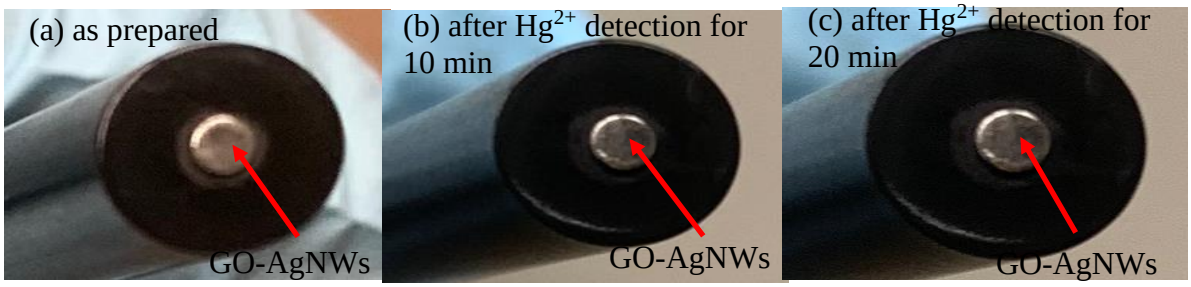

Figure 4.26 Photographs of the GO-AgNWs composite modified Pt electrode (a) as-prepared (before electrochemical detection) (b) after Hg^{2+} detection for 10 min (c) after Hg^{2+} detection for 20 min.

4.1.7 Analysis of Real Sample

The feasibility of the GO-AgNWs composite modified Pt sensor for real sample analysis was evaluated by determining Hg^{2+} in tap water. Tap water was collected from Daktronics Engineering Hall, South Dakota State University, SD, USA. Tap water was diluted with 0.1M KCl in a ratio of 1:9, without any further sample treatment [177]. The

tap water samples were spiked with different known concentrations of Hg^{2+} and then analyzed with SWASV. No response of Hg^{2+} was found in tap water without spiking which indicated that the concentration of the target Hg^{2+} was well below the detection limit or no target Hg^{2+} existed in the tap water. From Table 4.1, the high recovery percentage suggests that the GO-AgNWs composite modified Pt sensor has an excellent capability for accurate detection of Hg^{2+} in tap water [17].

Table 4.1 Determination of Hg^{2+} in real water samples using GO-AgNWs composite modified Pt sensor (n = 3).

Sample	Concentration of Hg^{2+}		Recovery (%)
	Add (nM)	Found (nM)	
Tap water 1	1.0	0.9	90.0
Tap water 2	10.0	8.7	87.0
Tap water 3	70.0	69.0	98.6

Comparison of sensing performance among different electrochemical Hg^{2+} sensors in terms of LOD and LDR are summarized in Table 4.2, demonstrating that the GO-AgNWs composite modified Pt sensor is a promising candidate for ultrasensitive detection of Hg^{2+}. Based on different methods including electrochemical, fluorometric, luminescent,

etc., the GO-AgNWs composite modified Pt sensor showed lower LOD compared to previously reported works [33, 34, 82, 115, 126, 177, 178], where the lowest reported LOD was 0.000001 nM [81]. The GO-AgNWs composite modified Pt sensor demonstrated higher LDR than these previous works [113, 116, 127, 178, 179].

The GO-AgNWs composite modified Pt sensor exhibited better LOD and LDR than other reports on graphene nanocomposites[180, 181] and nanoporous AuNPs [178]. The reported LODs in some previous works [33, 126, 177] are above the safety limit of Hg^{2+} in drinking water (5 nM) defined by the WHO, while the GO-AgNWs composite modified Pt sensor met this safety limit. Some reports including DNA-MoS_2/AuNPs [130], DNA-rGO [182], Oligonucleotide-WS_2 nanosheet [127], GQD-AuNPs/GCE [113], AgNPs/GCE [179], AuNPs-rGO [116] had lower and comparable LODs but lower LDRs. The following works L-Cys-rGO/GCE [115], DNA-WS_2 nanosheet [82], Graphene Aerogel-MOF [34] met the safety limit with high LDRs, however, had higher LODs than our work. Only a few reports including MoS_2/GCE [81], N-doped rGO/MnO_2/GCE [119] had better LODs and LDRs than our work. Further, the MoS_2/GCE [81] showed the LODs of 0.000001 nM, however, this LOD value is far away from their achieved LDRs. The reported LDR for Au/Ag/Au/CS–GO [128] is above the safety limit of Hg^{2+} in drinking water [17].

Table 4.2 Comparison of sensing performance among different electrochemical Hg^{2+} sensors.

Modifications	LOD (nM)	LDR (nM)	Method	References

GO-AgNWs/Pt	**0.10**	**1-70**	**Electrochemical**	**This work**
Nanoporus AuNPs/ITO	0.15	5-50	Electrochemical	[178]
rGO-Au/CPE	2.04	5-40	Electrochemical	[181]
$MnFe_2O_4$-Cysteine/GCE	208	1400-3000	Electrochemical	[177]
AgNPs/GCE	0.028	0.1-10	Electrochemical	[179]
AuNPs-rGO	0.0075	0.05-5	Electrochemical	[116]
L-Cys-rGO/GCE	4.958	0-1600	Electrochemical	[115]
DNA-WS_2 nanosheet	3.3	6-650	Fluorometric	[82]
Graphene Aerogel-MOF	2	5-3000	Electrochemical	[34]
DNA-MoS_2/AuNPs	0.1	0.1-10	FET	[130]
DNA-rGO	0.1	0.1-10	Electrochemiluminescence	[182]

rGO-AgNPs	20	100-10,0000	UV-vis absorption spectroscopy	[126]
MoS_2/GCE	0.000001	0.1-20,000	Electrochemical	[81]
Oligonucleotide-WS_2 nanosheet	0.10	0.5-20	Fluorometric	[127]
GO-DNA	0.356	0-0.05	Fluorometric	[180]
GQD-AuNPs/GCE	0.02	0-1	Electrochemical	[113]
CNFs/AuNPs	30	100-1200	Electrochemical	[33]
Au/Ag/Au/CS–GO	-	500-25,000	Surface plasmon resonance	[128]
N-doped rGO/MnO_2/GCE	0.0414	10-200	Electrochemical	[119]

GO: graphene oxide; AuNPs: gold nanoparticles; ITO: indium tin oxide; CPE: carbon-paste electrode; AgNPs: silver nanoparticles; GCE: glassy carbon electrode; L-Cys: L-cysteine; rGO: reduced graphene oxide; MoS_2: molybdenum disulfide; WS_2: tungsten

disulfide; GQD: graphene quantum dot; CNFs: carbon nanofibers; CS: chitosan; AgNW: silver nanowire; MOF: metal-organic framework; FET: field-effect transistor;

4.2 1T-WS_2 Microflower Based Electrochemical Sensor for Hg^{2+} Detection

4.2.1 Structural and Morphological Characteristics

The crystal structure of the 1T-WS_2 was investigated by XRD analysis. Figure 4.27 shows the XRD pattern for the as-prepared 1T-WS_2. In contrast to the (002) characteristic peak for bulk 2H-WS_2 at 14.36°, the XRD patterns showed a new $(002)_{new}$ characteristic peak at 9.40°. A second third order diffraction peak $(004)_{new}$ and $(006)_{new}$ peaks in the range of 16°-30° were observed, which are consistent with that of previous reports [85, 137, 183].

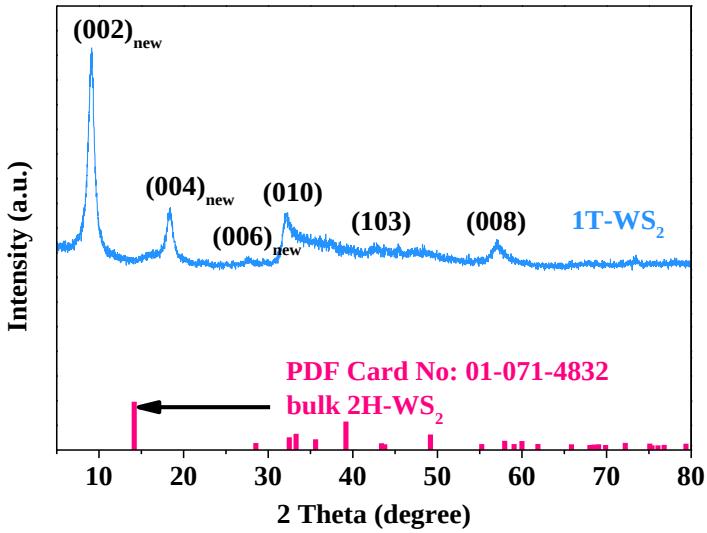

Figure 4.27 The XRD patterns for hexagonal 1T-WS_2 in contrast with the peak lines of bulk 2H-WS_2 from the Powder Diffraction File (PDF) card.

The Raman spectrum of the 2H-WS_2 and 1T-WS_2 structure is shown in Figure 4.28. Two prominent peaks observed at 356.72 cm^{-1} and 400.43 cm^{-1} can be attributed to the in-

plane (E^1_{2g}) and out-of-plane (A_{1g}) modes of the 2H-WS_2 [85]. On the other hand, several new sharp peaks observed at 132.24 cm^{-1}, 186.42 cm^{-1}, 261.82 cm^{-1}, and 325.13 cm^{-1} equivalents to J_1, J_2, A_g, and J_3 peaks, respectively, confirms the formation of 1T-WS_2 [85, 183, 184]. The appearance of these new peaks in the low-frequency region can be ascribed to the presence of a zigzag-chain superlattice [85]. The absence of the characteristic peak for (E^1_{2g}) mode in the Raman spectrum of 1T-WS_2 reveals the formation of 1T phase dominated WS_2 which is well supported by the literature [184].

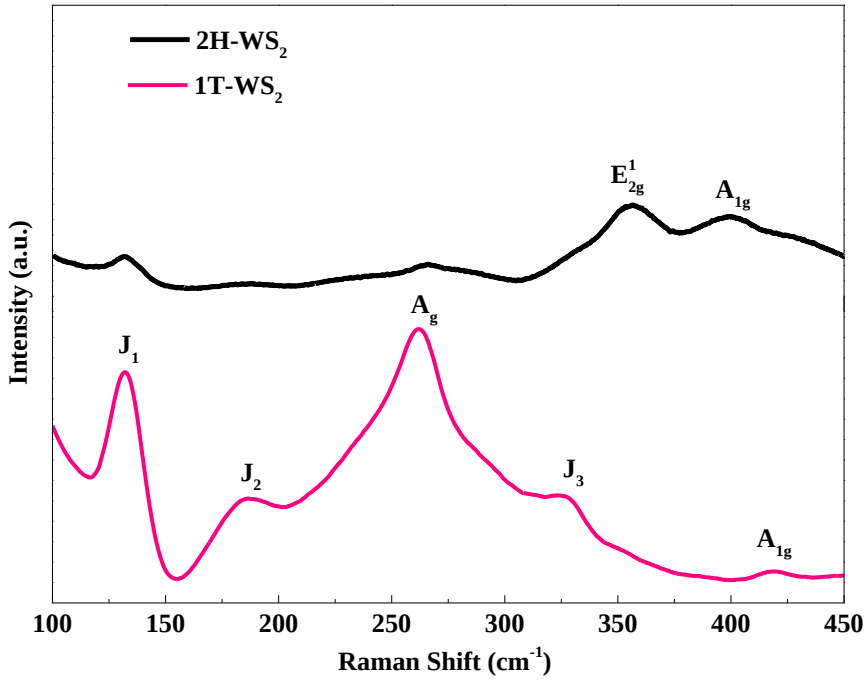

Figure 4.28 Raman spectra of 2H-WS_2 and 1T-WS_2 sample.

Figure 4.29a-b shows the FESEM image of the as-synthesized 1T-WS_2 microflowers with the magnified view shown in Figure 4.29c. These images show the formation of uniform flower-like WS_2 nanostructures with a diameter from 3 to 5 µm. Each microflower is composed of hundreds of self-assembled curved WS_2 nanopetals or

nanosheets which are tens of nanometers in thickness (Figure 4.29c). Moreover, these nanopetals can form relatively open and porous nanostructures which may provide enhanced loading and rapid diffusion opportunity for Hg^{2+} ions [137].

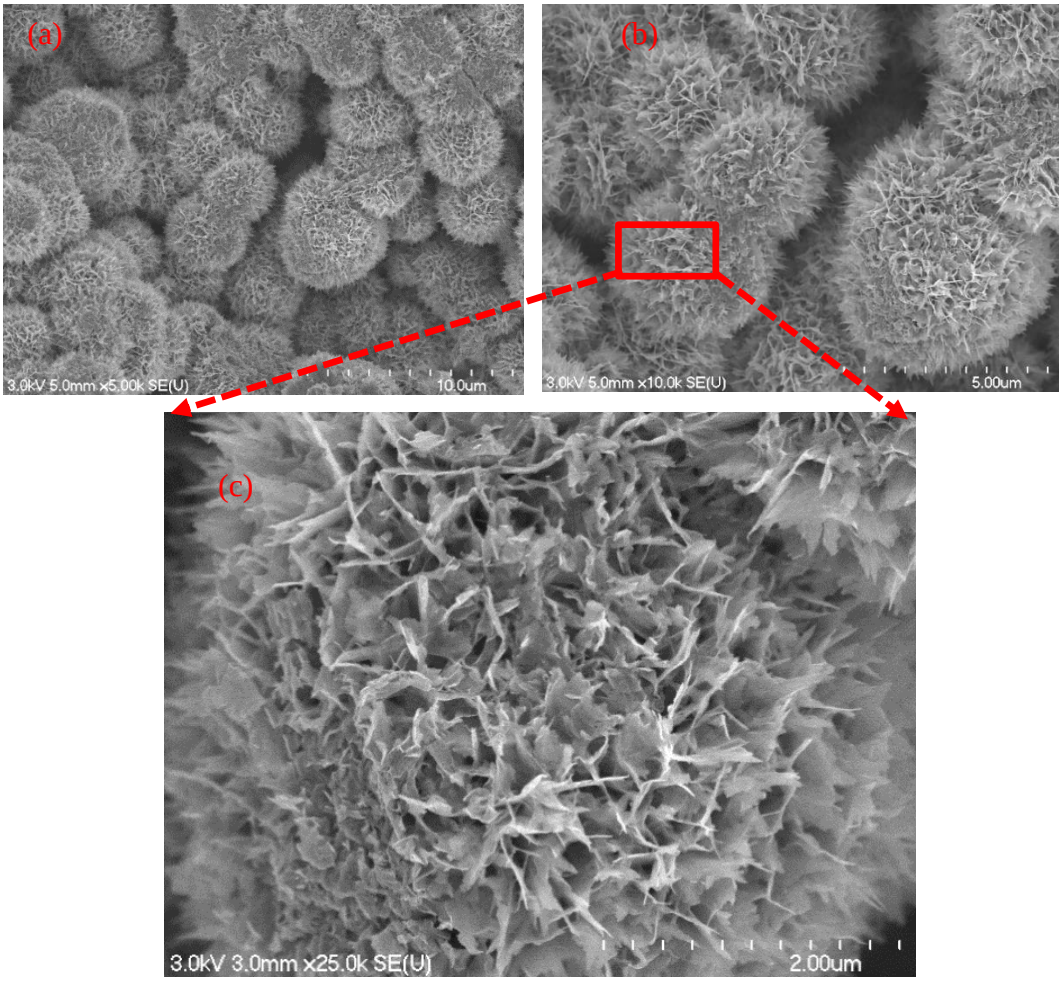

Figure 4.29 (a-b) FESEM images of 1T-WS_2 microflowers (c) high magnification image of WS_2 microflowers.

The morphology and microstructure of 1T-WS_2 were analyzed by TEM. The TEM images (Figure 4.30a-b) further confirmed the flower shape of 1T-WS_2 and showed obvious ripples and corrugations indicating the flexible and ultrathin nature of the WS_2 microflowers. The light-colored and homogenous areas can be attributed to the regions of

stacking single layer or few layers WS_2 nanosheets [185]. The less transparent regions are stacking of the multiple WS_2 nanosheets. Figure 4.30c-d shows the high-resolution TEM images taken from the edge of the WS_2 microflower. It can be observed that the microflowers have a layered structure with an interlayer distance of ~ 0.82 nm (Figure 4.30d), corresponding to the $(002)_{new}$ plane for 1T-WS_2 [137].

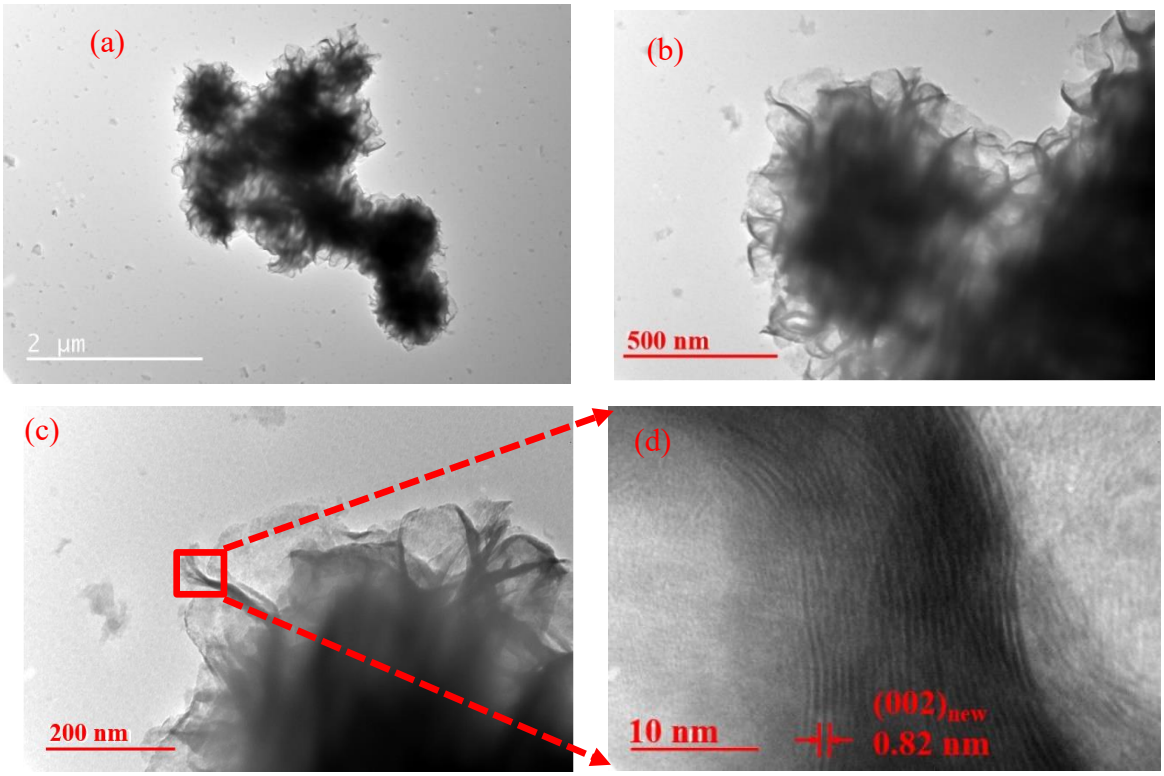

Figure 4.30 (a-b) TEM images of 1T-WS_2 microflowers (c-d) high magnification images of WS_2 microflowers.

The elemental composition of the 1T-WS_2 powder was analyzed by EDS. Figure 4.31 shows the elemental mapping of tungsten (W) and sulfur (S) together. Two main elements of W and S were observed in the samples, indicating a high purification of the synthesized 1T-WS_2. The weight percentage of W and S in the 1T-WS_2 was 71.1% and 28.9%, while the atomic percentage of that was 30.1% and 69.9%, respectively [137].

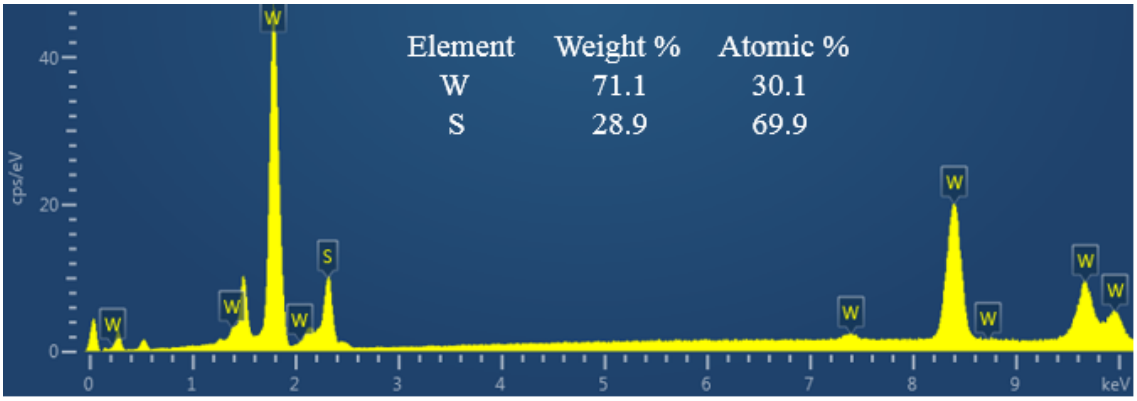

Figure 4.31 EDS spectrum of 1T-WS_2.

Based on the obtained experimental results and the previously reported synthesis techniques, a formation mechanism for flower-like WS_2 has been proposed which involves a three-stage growth process including fast nucleation, aggregation of nanosheets, and self-assembly of flower-like structure. A schematic diagram is given in Figure 4.32 to demonstrate the formation mechanism of flower-shaped WS_2. Here, $(NH_4)_6H_2W_{12}O_{40}.xH_2O$ and CSN_2H_4 were selected as the source for tungsten and sulfur, respectively. During the whole process, thiourea ($C_2H_2O_4.2H_2O$) will act as a nucleation catalyst [183]. In the first stage, more H_2S would be produced from the hydrolysis of thiourea (equation 4.1) and more WS_2 nuclei could be formed through subsequent chemical reactions (equation 4.2-4.4). Under hydrothermal treatment, the WS_2 nuclei would aggregate to form small WS_2 nanosheets based on their favorable crystal growth. Finally, the thin WS_2 nanosheets would be self-assembled and corrugated into flower shape due to the reduced surface energy [186]. According to the previous work, the formation of flower shape WS_2 involves the following suggested chemical reactions:[183, 186-188] [137]

$$CSN_2H_4 + 2H_2O \rightarrow 2NH_3 + CO_2 + H_2S \quad (4.1)$$

$$(NH_4)_6H_2W_{12}O_{40} \rightarrow 6NH_3 + 12WO_3 + 4H_2O \quad (4.2)$$

$$WO_3 + 3H_2S + H_2O \rightarrow WO_2 + SO_4^{2-} + 2H^+ \quad (4.3)$$

$$WO_2 + 2H_2S \rightarrow WS_2 + 2H_2O \quad (4.4)$$

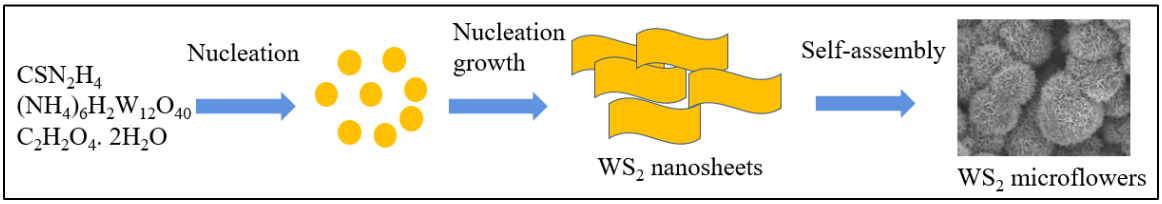

Figure 4.32 Schematic diagram of the formation mechanism of flower-like WS_2 microstructures.

4.2.2 Electrochemical Characterization and Optimization of the Experimental Conditions

The CV results for 1T-WS_2 modified GCE, 2H-WS_2 modified GCE, and bare GCE are shown in Figure 4.33a. The 1T-WS_2 modified GCE showed higher anodic and cathodic peak currents than 2H-WS_2 modified GCE and bare GCE which is ascribed to the excellent electronic conductivity of 1T-WS_2. Further, the electron transfer properties were studied by conducting EIS. The 1T-WS_2 modified GCE exhibited a charge transfer resistance (R_{ct}) value of 3.12 kΩ which is much lower than the 2H-WS_2 modified GCE with 13.75 kΩ and bare GCE with 16.09 kΩ (Figure 4.33b). This suggests that the metallic 1T-WS_2 can enhance the conduction pathway for electron transfer kinetics when anchored on the surface of GCE. In contrast, the semiconducting nature of 2H-WS_2 causes sluggish electron transfer between GCE and redox couple. These EIS results are well agreed by the CV observations [137].

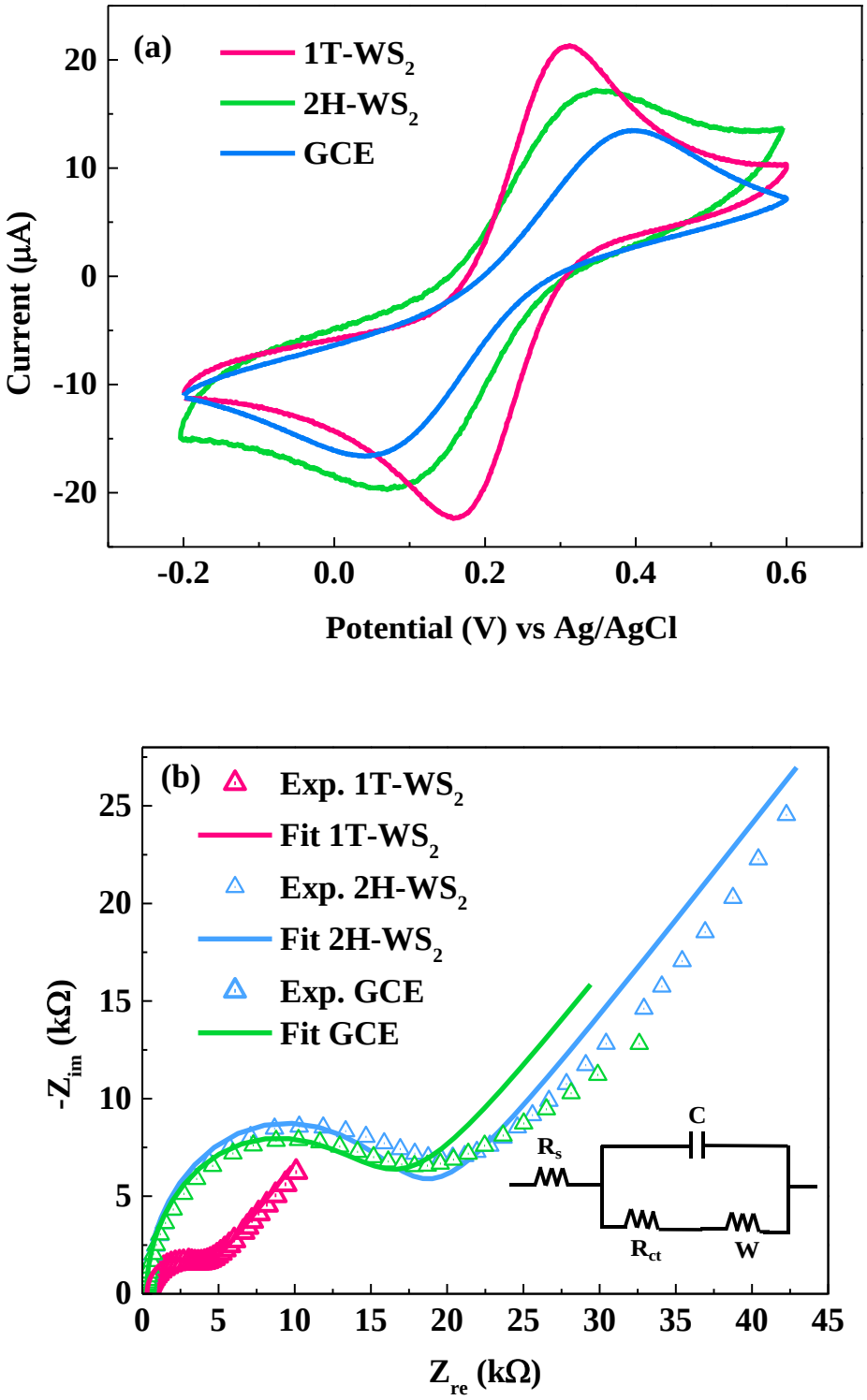

Figure 4.33 (a) CV of 1T-WS_2 modified GCE, 2H-WS_2 modified GCE, and bare GCE (b) Nyquist plots of 1T-WS_2 modified GCE, 2H-WS_2 modified GCE, and bare GCE in 5.0

mM $K_3[Fe(CN)_6]$ solution containing 0.1 M KCl. The inset shows the equivalent circuit used to fit the impedance data.

To achieve the utmost sensing performance for the 1T-WS_2 modified GCE, the experimental parameters including deposition potential, deposition time, pH of the buffer, and concentration of 1T-WS_2 were optimized in 0.1 M acetate buffer containing 1 mM Hg^{2+}. For the optimization of deposition potential, the effect of various deposition potential (from + 0.1 V to - 1.2 V) on stripping peak currents was studied as shown in Figure 4.34a. The stripping peak current increased with lowering the potential from + 0.1 V and reached a maximum value at - 0.4 V. While further lowering the deposition potential up to -1.2 V, the stripping peak current decreased and might be due to hydrogen evolution which hinders the deposition of Hg^{2+} ions onto the electrode surface [105] [137].

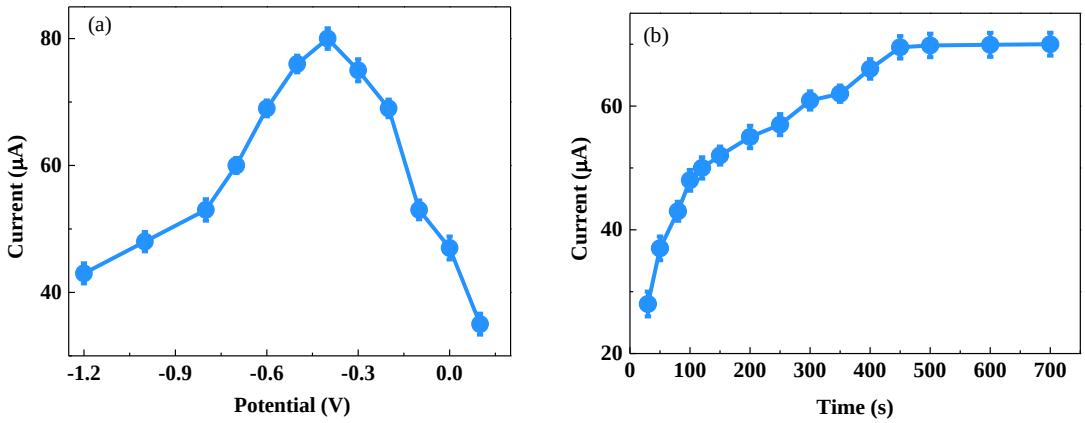

Figure 4.34 Optimization of the experimental conditions: Effects of (a) deposition potential (b) deposition time on the current responses of the 1T-WS_2 modified GCE for 1 mM Hg^{2+}. Data were presented as mean ± s.d. (n = 3).

The amount of accumulating Hg^{2+} ions onto the electrode surface is influenced by the deposition time, which further affects the stripping peak currents of the Hg^{2+} detection. For the optimization of deposition time, the effect of various deposition time (from 30 s to 700 s) on the stripping peak currents was studied as shown in Figure 4.34b. Initially, the stripping peak currents increased with the deposition time due to the increased amount of Hg^{2+} ions on the electrode surface and remained steady after 450 s. This indicates the saturation of available active sites on the 1T-WS_2 modified GCE surface after 450 s [34] [137].

For the optimization of the concentration of 1T-WS_2, the effect of various concentrations (from 0.5 to 2.0 mg mL^{-1}) on the stripping peak currents for 0.8 µM of Hg^{2+} was studied as shown in Figure 4.35a. With the increase of 1T-WS_2 concentration from 0.5 to 1.0 mg mL^{-1}, higher peak currents were observed which can be attributed to the increase in the conductivity of 1T-WS_2 leading to a faster electron transfer rate. The maximum value of the peak current was obtained at 1.0 mg mL^{-1}. However, a further increase in concentration to 2.0 mg mL^{-1} led to a decrease in the peak current which may be due to a higher thickness of 1T-WS_2, thus creating an aggregation of 1T-WS_2 and impeding the electron transfer rate. Therefore, to obtain a highly sensitive response, the optimized concentration of 1T-WS_2 was found to be 1.0 mg mL^{-1} [137].

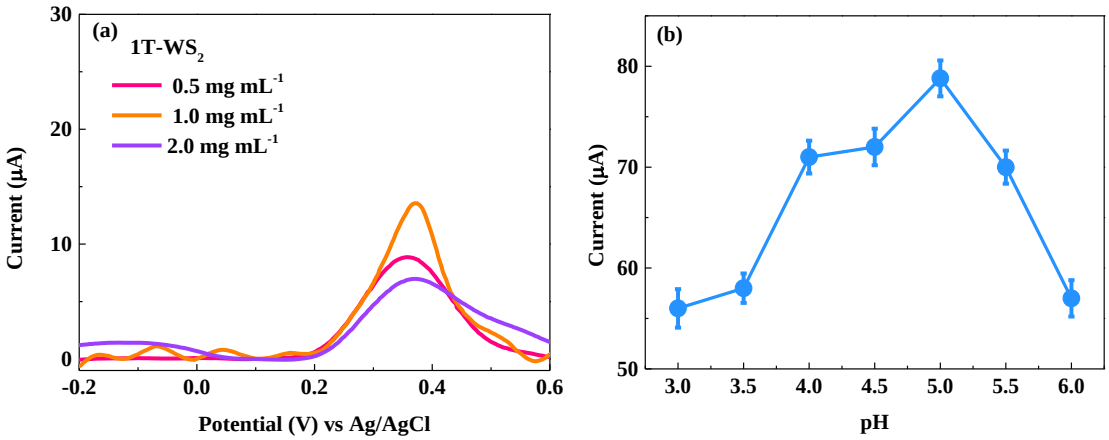

Figure 4.35 (a) SWASV response of the different concentrations of 1T-WS_2 modified GCE for 0.8 µM Hg^{2+} (b) Optimization of the experimental conditions: Effects of pH of the buffer on the current responses of the 1T-WS_2 modified GCE for 1 mM Hg^{2+}. Data were presented as mean ± s.d. (n = 3).

Furthermore, the influence of the pH of the buffer on the stripping response of Hg^{2+} was analyzed in the range of 3.0-6.0 as shown in Figure 4.35b. The maximum stripping peak current for Hg^{2+} was observed at pH 5.0. The lower stripping peak currents at lower pH (pH<5) can be attributed to the protonation of sulfur (S^{2-}) groups which weakens the absorption ability of Hg^{2+} on the 1T-WS_2 modified GCE [189]. When the pH was further increased (pH >5), the stripping peak currents reduced indicating hydrolysis of Hg^{2+} ions, which hinders the deposition of Hg^{2+} ions on the 1T-WS_2 modified GCE [7]. All the remaining measurements were performed under the optimized experimental conditions of deposition potential (- 0.4 V), deposition time (450 s), pH of the buffer (5.0), and concentration of 1T-WS_2 (1.0 mg mL^{-1}) unless otherwise stated [137].

4.2.3 Analytical Performance of the 1T-WS_2 Modified Electrodes

SWASV response of the 1T-WS_2 modified GCE was performed for different concentrations of Hg^{2+}. Figures 4.36a-c showed that the stripping responses toward Hg^{2+} increased with an increase in the concentration from 1.0 nM to 1 mM. The peak intensities increased linearly with increasing concentration of Hg^{2+}. The well defined and stable stripping peaks were observed for Hg^{2+} at + 0.38 V (Figure 4.36a). Four LDRs were found for the sensing of Hg^{2+} on 1T-WS_2 modified GCE. The first LDR was obtained over the low concentration range of 1.0 nM-90 nM with a sensitivity of 15.9 µA/µM (inset of Figure 4.36a). Similarly, the second and third LDRs were found over the moderate concentration range of 0.1-0.4 µM and 0.5-1.0 µM with a sensitivity of 2.54 µA/µM and 13.84 µA/µM, respectively (inset of Figure 4.36b). The fourth LDR was found over the high concentration range of 0.1-1.0 mM with a sensitivity of 0.04646 µA/µM (inset of Figure 4.36c). As observed, the sensitivity decreases at moderate and high concentration ranges. At low concentrations of Hg^{2+}, many S^{2-} sites are available to interact with Hg^{2+}, leading to higher sensitivity than the moderate and high concentrations of Hg^{2+}. However, with increasing the concentration of Hg^{2+}, the number of S^{2-} sites for detecting Hg^{2+} decreases, leading to a lower sensitivity at moderate and high concentrations of Hg^{2+} [190]. The LOD of the 1T-WS_2 modified GCE toward Hg^{2+} was calculated to be 0.0798 nM or 79.8 pM based on the 3σ method (where σ is the standard deviation for 10 blank samples), which is very well below the recommended guidelines of the WHO and the US EPA for the value of Hg^{2+} in drinking water [137].

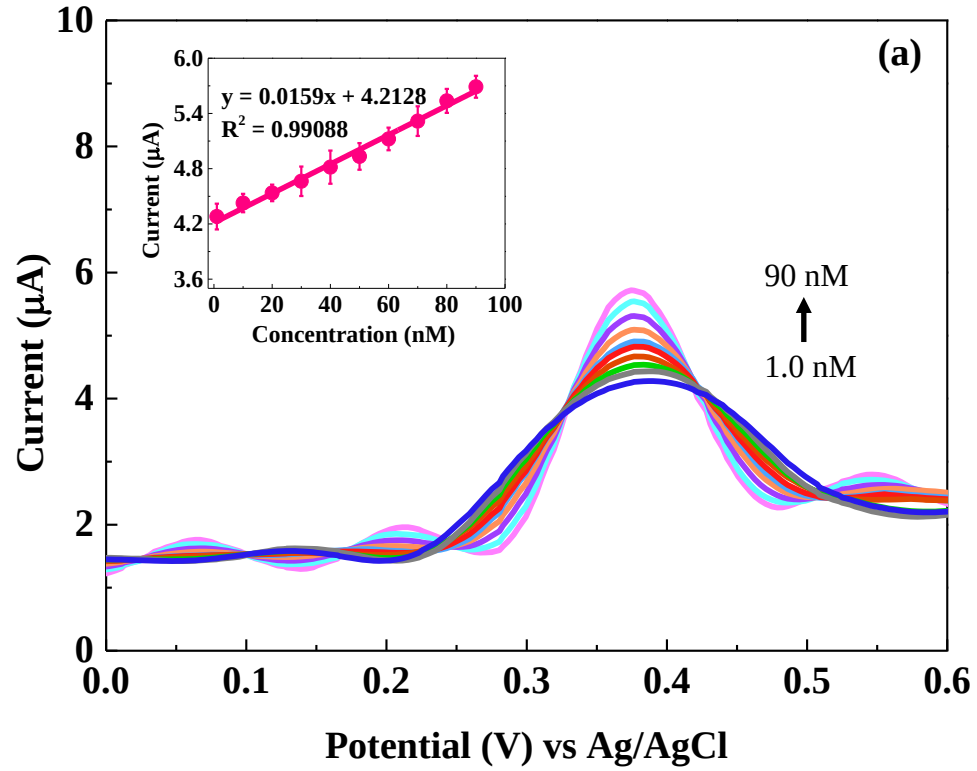

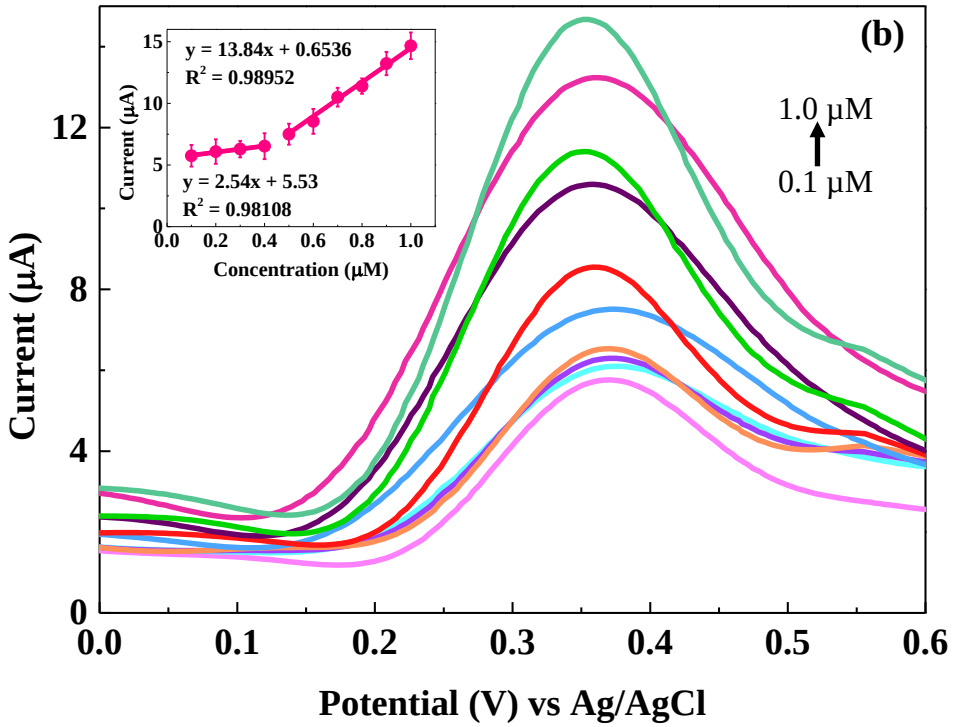

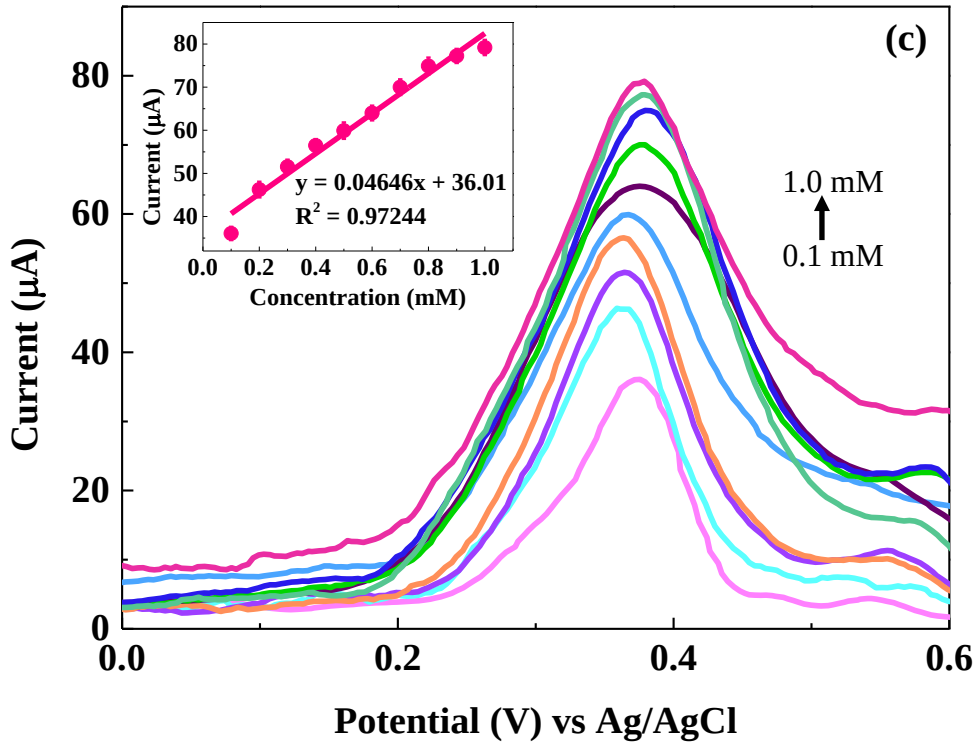

Figure 4.36 SWASV responses of the 1T-WS_2 modified GCE with increasing concentrations of Hg^{2+} in the range of (a) 1.0-90 nM (b) 0.1-0.4 µM and 0.5-1.0 µM (c) 0.1-1.0 mM. Data are presented as mean ± s.d. (n = 3).

The LOD and LDR of various modified electrodes for Hg^{2+} detection are compared in Table 4.3. Based on different methods including electrochemical, fluorescence, electrochemiluminescence, etc., the 1T-WS_2 microflowers modified GCE developed in this work showed better LOD and LDR than the previous reports on DNA-WS_2 nanosheet [82], Oligonucleotide-WS_2 [127], DNA-rGO [182], Nanoporous Au-Thymine [178], DNA-MoS_2/AuNPs [130]. Furthermore, the developed sensor showed higher LDR compared to these previous works on AgNPs [179], AuNPs-rGO [116], and N-doped rGO/MnO_2 [119]. In addition, 1T-WS_2 microflowers modified GCE exhibited a lower LOD and LDR than some of the previous reports on N-doped WS_2 nanosheets [133], Graphene Aerogel-MOF

[34], $MnFe_2O_4$-Cysteine[177], CNFs/AuNPs [33], where the lowest LOD of 0.000001 nM was reported by Aswathi *et al* [81]. Thus, the above comparisons suggest that the 1T-WS_2 microflowers modified GCE developed in this work exhibit comparable performance parameters to the previous reports and the obtained LOD (0.0798 nM) is well below the US EPA and the WHO recommended level of Hg^{2+} in drinking water [137].

Table 4.3 Comparison of the sensing performance of various modified electrodes for the detection of Hg^{2+}.

Modifications	LOD (nM)	LDR (nM)	Method	References
1T-WS_2 nanoflowers	**0.0798**	**1-1000 nM, 0.1-1.0 mM**	**Electrochemical**	**This work**
Nanoporous Au-Thymine	0.15	5-50	Electrochemical	[178]
$MnFe_2O_4$-Cysteine	208	1400-3000	Electrochemical	[177]
DNA-WS_2 nanosheet	3.3	6-650	Fluorescence	[82]

AgNPs	0.028	0.1-10	Electrochemical	[179]
AuNPs-rGO	0.0075	0.05-5	Electrochemical	[116]
Graphene Aerogel-MOF	2.0	5-3000	Electrochemical	[34]
DNA-MoS_2/AuNPs	0.1	0.1-10	FET	[130]
MoS_2 flakes	0.03	0.03-1000	FET	[129]
MoS_2 nanosheets	0.000001	0.1-20,000	Electrochemical	[81]
Oligonucleotide-WS_2 nanosheets	0.10	0.5-20	Fluorescence	[127]
DNA-rGO	0.10	0.1-10	Electrochemiluminescence	[182]
N-doped rGO/MnO_2	0.0414	10-200	Electrochemical	[119]
CNFs/AuNPs	30	100-1200	Electrochemical	[33]

N-doped WS_2 nanosheets	20	10-5000	Fluorescence	[133]

Abbreviations: WS_2: tungsten disulfide; AgNPs: silver nanoparticles; AuNPs: gold nanoparticles; rGO: reduced graphene oxide; MOF: metal-organic framework; MoS_2: molybdenum disulfide; CNFs: carbon nanofibers; FET: field-effect transistor.

4.2.4 Selectivity, Repeatability, Reproducibility, and Stability

Several potential heavy metal ions including Cu^{2+}, Fe^{3+}, Ni^{2+}, Pb^{2+}, Cr^{3+}, K^{+}, Na^{+}, Ag^{+}, Sn^{2+}, and Cd^{2+} as interference were tested to demonstrate the selectivity of the 1T-WS_2 modified GCE as shown in Figure 4.37. At 100 μM, the interfering metal ions showed significantly poorer stripping response as compared to that for Hg^{2+}. The corresponding SWASV responses for interference metal ions showed no obvious peak in the potential range of - 1.0 to + 0.7 V (Figure 4.38). These results confirm that the 1T-WS_2 modified GCE exhibits an excellent selectivity toward Hg^{2+}. This can be attributed to the higher standard reduction potential of Hg^{2+} over other interfering metal ions and strong affinity of Hg^{2+} towards S^{2-}.[81] To further test the cross selectivity of the 1T-WS_2 modified electrode, Hg^{2+} and other heavy metal ions were mixed. A similar stripping response was observed for the mixture of Hg^{2+} and other ions that reveals no significant interference from other ions. These results verify the cross selectivity of the 1T-WS_2 modified electrode. It is known that for two metal ions both having affinity to S^{2-}, the metal ion having higher reduction potential will get preferably reduced by the S^{2-} on the surface of 1T-WS_2 [81]. Thus, Hg^{2+} with its higher standard reduction potential (+ 0.85 V) shows more tendency to

reduce over interfering Cu^{2+} (+ 0.34 V), Fe^{3+} (+ 0.77 V), Ni^{2+} (- 0.25 V), Pb^{2+} (- 0.13 V), Cr^{3+} (- 0.74 V), K^{+} (- 2.92 V), Na^{+} (- 2.71 V), Ag^{+} (+ 0.80 V), Sn^{2+} (- 0.14 V), and Cd^{2+} (- 0.40 V) [81] [137].

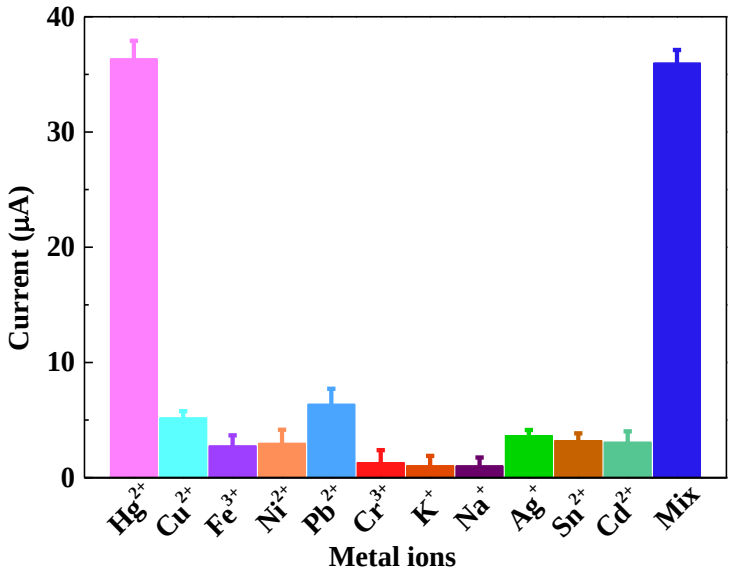

Figure 4.37 Electrochemical responses of 1T-WS_2 modified GCE to different heavy metal ions relative to the signal of Hg^{2+}. The concentration of Hg^{2+} and the interfering metal ions was 100 µM.

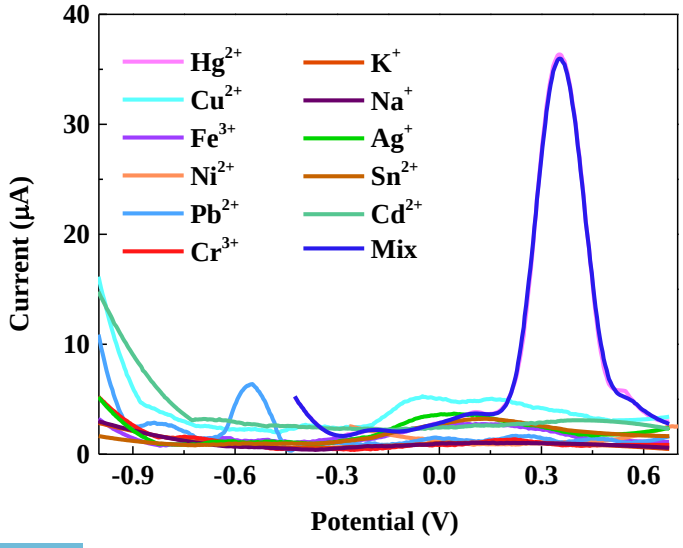

Figure 4.38 The SWASV response of the 1T-WS_2 modified GCE for heavy metal ions including Hg^{2+}, Cu^{2+}, Fe^{3+}, Ni^{2+}, Pb^{2+}, Cr^{3+}, K^{+}, Na^{+}, Ag^{+}, Sn^{2+}, Cd^{2+}, and the mixture of Hg^{2+} with other ions.

Repeatability of the sensor was investigated after six replicated tests for 100 µM Hg^{2+} with a single 1T-WS_2 modified GCE. The identical stripping responses toward Hg^{2+} were observed for every test as shown in Figure 4.39. The low RSD of 1.46% for the responses from the six tests confirms the good repeatability of the sensor. [137].

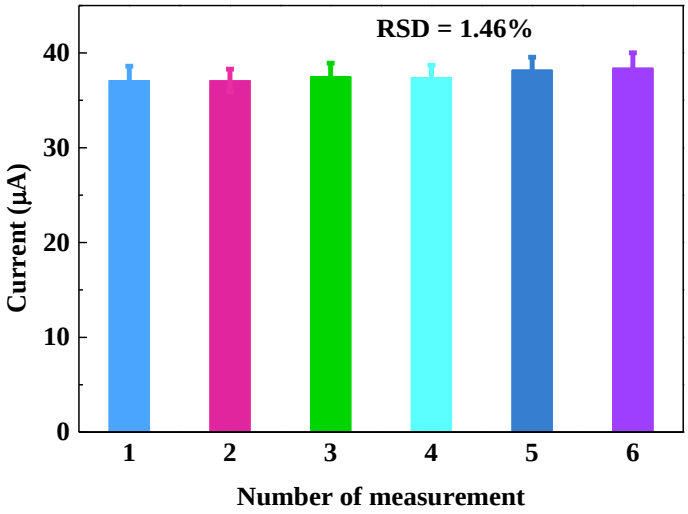

Figure 4.39 Repeatability of the 1T-WS_2 modified GCE for six replicated tests. Data are presented as mean ± s.d. (n = 3).

The reproducibility of the 1T-WS_2 modified GCE was also tested by preparing four identical 1T-WS_2 modified GCEs. The sensors were employed to detect 80 µM Hg^{2+}. Figure 4.40 represents the stripping responses for the four 1T-WS_2 modified GCEs, where the inset shows a histogram plot for peak current for different sensors tested. The low RSD

for four electrodes (0.87%) confirms the good reproducibility of the as-fabricated electrochemical sensor [137].

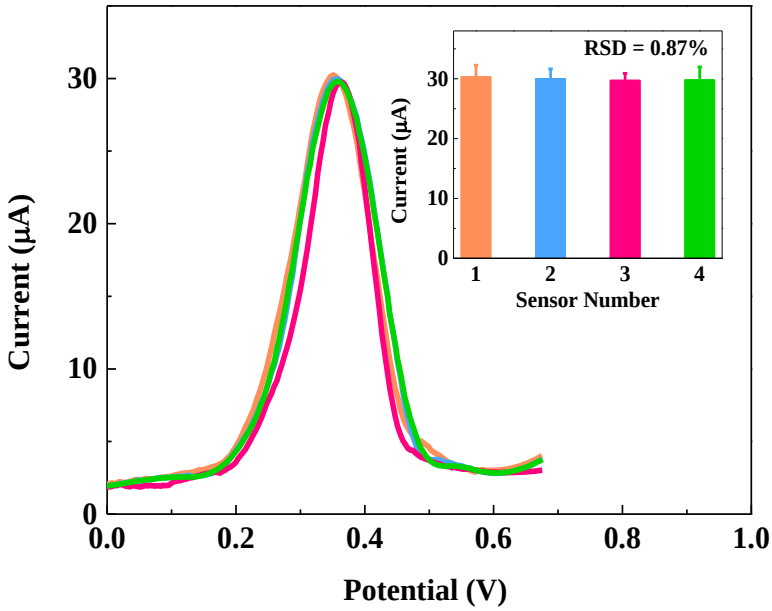

Figure 4.40 Reproducibility of the 1T-WS_2 modified GCE. The inset shows a histogram plot for peak current for the four sensors. Data are presented as mean ± s.d. (n = 3).

Figure 4.41 shows the stability of the 1T-WS_2 modified GCE. The stability of the 1T-WS_2 modified GCE was evaluated by measuring the stripping response up to 32 days with an interval of three days. Meanwhile, the electrode was stored at room temperature. The 1T-WS_2 modified GCE showed current response retention of 93.23% on the 20^{th} day and 79.34% on the 32^{nd} day. This result demonstrates the good stability of the 1T-WS_2 modified GCE. The photographs in Figure 4.42 shows there is no depletion or separation of the 1T-WS_2 films after 32 days. This confirms that 1T-WS_2 shows excellent adhesive and stable properties [137].

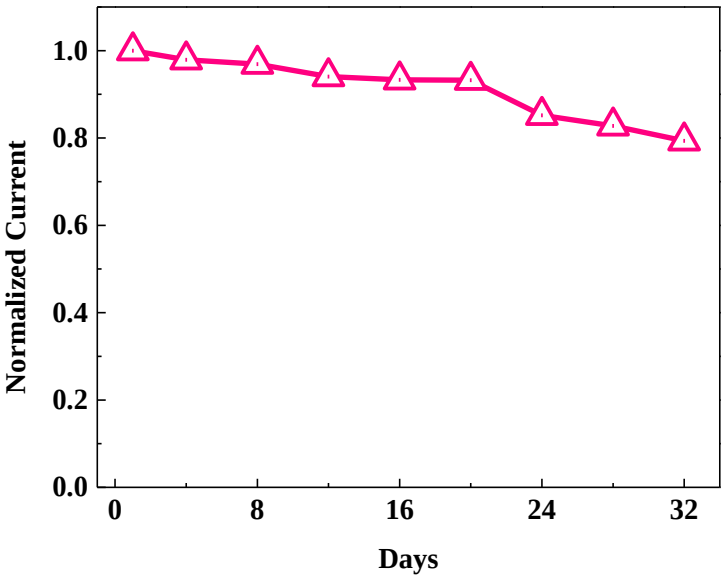

Figure 4.41 Stability of the 1T-WS_2 modified GCE in response to 1 mM Hg^{2+} over 32 days.

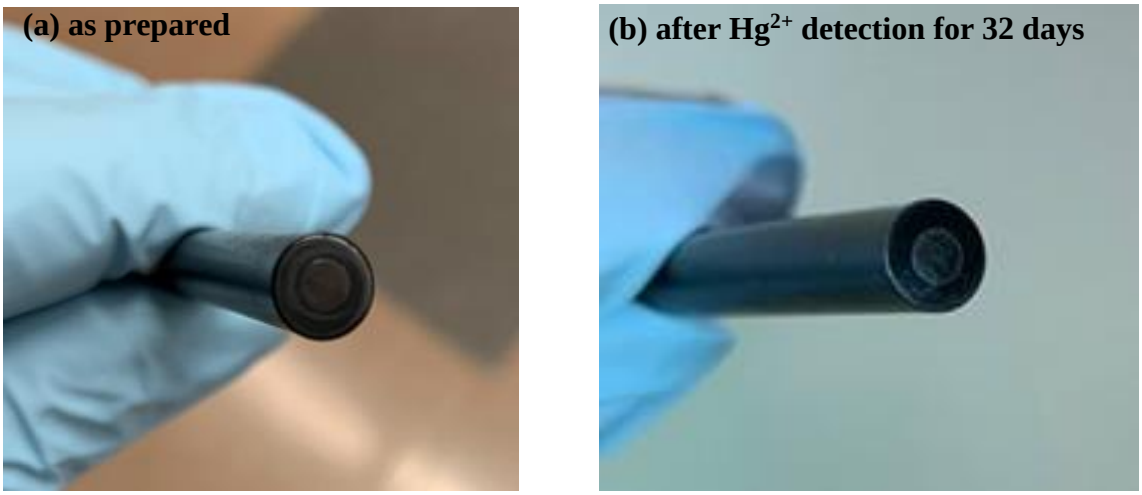

Figure 4.42 Photographs of the 1T-WS_2 modified GCE (a) as-prepared (b) after Hg^{2+} detection for 32 days.

4.2.5 Analysis of Real Sample

The applicability of the 1T-WS_2 modified GCE was evaluated by determining the concentration of Hg^{2+} in real samples including tap water. Tap water was collected from

Daktronics Engineering Hall, South Dakota State University, SD, USA. Before detection, tap water was diluted with 0.1 M acetate buffer in a volume ratio of 1:9, without any further sample treatment [177]. No response of Hg^{2+} was found in tap water without spiking which indicated that the concentration of the target Hg^{2+} was well below the detection limit or no target Hg^{2+} existed in the tap water. Then, standard solutions of Hg^{2+} (70 nM, 1.0 µM, and 100 µM) were spiked into tap water and further analyzed with SWASV. Table 4.4 is a summary of the obtained results. The recovery was 96 - 99.6% for Hg^{2+}. The obtained high recovery percentage suggests that the 1T-WS_2 modified GCE is feasible for accurate detection of Hg^{2+} in tap water [137].

Table 4.4 Determination of Hg^{2+} in tap water using 1T-WS_2 modified GCE.

Sample	Concentration of Hg^{2+}		Recovery (%) = found / add × 100
	Add (µM)	Found (µM)	
Tap water	0.0	Not detected	-
	0.07	0.068	97.1
	1.0	0.96	96.0
	100.0	99.6	99.6

4.2.6 Sensing Mechanism of Hg^{2+} and Evidence of WS_2-Hg interaction

Figure 4.43 illustrates the sensing mechanism of 1T-WS_2 modified GCE for Hg^{2+} ions. Initially, the Hg^{2+} ions are strongly adsorbed and deposited onto 1T-WS_2 by forming

the Hg-S complex as indicated by equations 4.5-4.7 [81]. In this deposition process, Hg^{2+} ions are reduced on the surface of 1T-WS_2 where Hg^{2+} ions act as strong oxidizing agents and S^{2-} acts as a reducing agent [131]. Here, the metallic 1T-WS_2 provides a pathway for the conduction of electrons. Fast charge transport through metallic 1T-WS_2 facilitates achieving high sensitivity, wide LDR, and lower LOD. During stripping, oxidation of metallic Hg occurs as indicated in the reversible redox reaction (4.7).

$$Hg^{2+} + 2e^- \longrightarrow Hg \qquad (4.5)$$

$$S^{2-} - 2e^- \longrightarrow S \qquad (4.6)$$

$$Hg^{2+} + S^{2-} \longleftrightarrow Hg - S \qquad (4.7)$$

The interaction between S^{2-} of WS_2 and Hg^{2+} was explained by analyzing Raman spectroscopy and Fourier-transform infrared spectroscopy (FTIR). Before the analysis, the $HgCl_2$ solution was added into WS_2 dispersions and dried [137].

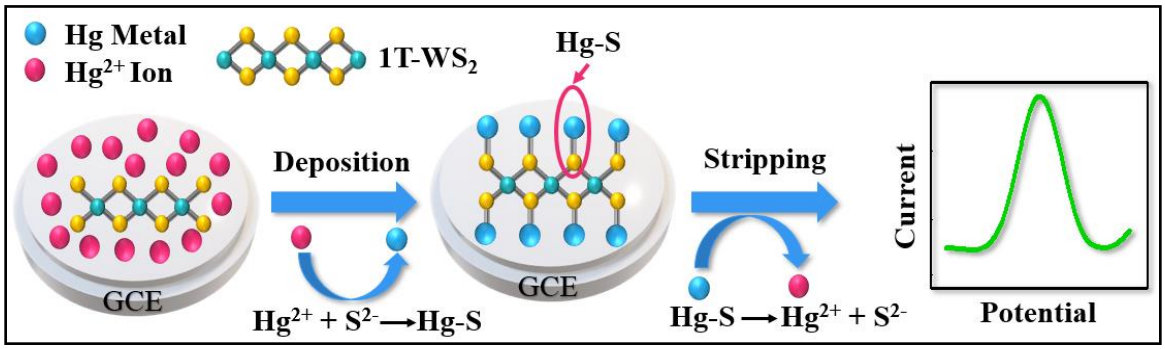

Figure 4.43 Schematic diagram of the sensing mechanism of Hg^{2+} using 1T-WS_2.

The Raman spectra for WS_2-Hg and WS_2 were measured and shown in Figure 4.44a. A red shift of A_{1g} mode was observed after the incorporation of Hg in WS_2 (inset of Figure 4.44a). The S-Hg interactions induced a local strain that caused a 3.22 cm^{-1} red shift

in the A_{1g} mode [81, 191, 192]. Thus, the results suggest an interaction between S^{2-} of WS_2 and Hg^{2+} [137].

Further, the FTIR spectra for WS_2-Hg and WS_2 was recorded in the range of 500 - 3500 cm^{-1} and shown in Figure 4.44b. The differences between the two spectra were observed in the region of 700-1100 cm^{-1} (inset of Figure 4.44b). A significant shift of the characteristics S-S bond for WS_2-Hg was observed at 946.32 cm^{-1} from 939.23 cm^{-1} of WS_2 [188]. The shift of S-S bond is an indication of the electrostatic interaction between S^{2-} and Hg^{2+}, which can affect the W-S and S-S bonding strength due to the formation of S-Hg covalent bond [81]. Thus, the FTIR spectra reveal S-Hg interaction [137].

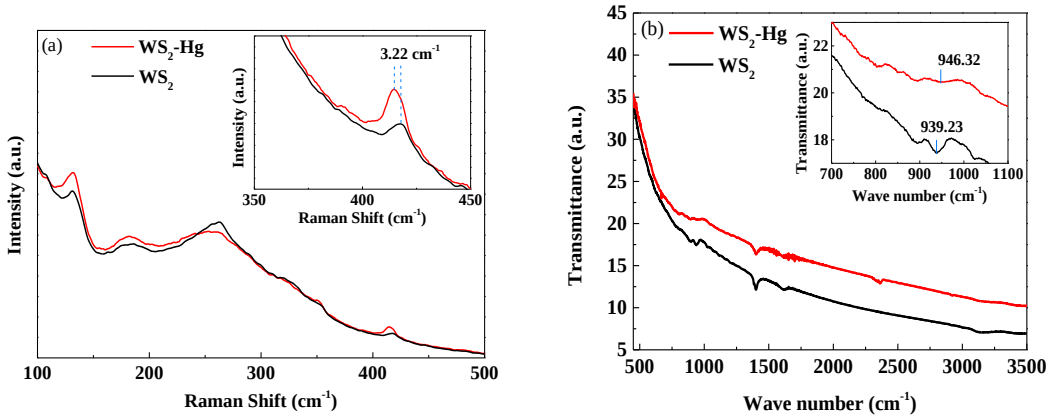

Figure 4.44 Experimental results showing S-Hg interaction (a) Raman spectra and (b) FTIR spectra of WS_2 and WS_2-Hg.

CHAPTER 5 SUMMARY AND CONCLUSIONS

5.1 Summary

Heavy metal contaminants are a threat to public health and other living organisms due to their toxicity and nonbiodegradability. The accumulation of a trace amount of heavy metals including Hg, Pb, Cd, As, etc., in the human body through drinking water and food chain can cause life-threatening diseases including such as arrhythmia, cardiomyopathy, kidney and respiratory failure, central nervous defects, pulmonary diseases, etc. Hg is one of the harmful pollutants and heavy metals that is produced by the natural, domestic, and industrial sources such as pesticides, energy storage, mining, coal combustion, power plants, thermometers, and cosmetics. To regulate the heavy metal uptake in our body, the WHO and the EPA have defined guideline values of heavy metals in drinking water.

Various traditional methods have been established for the quantitative detection of heavy metals in water and environmental samples. Among them, AAS, fluorescence spectroscopy, UV-vis spectrometry, ICP-MS, etc., are widely used for monitoring heavy metals. Although these conventional techniques have enabled efficient detection of heavy metals, they still suffer from many disadvantages such as high cost, low sensitivity, complex operation, bulky instrumentation, slow response, time-consuming, inconvenient for on-site testing, lack of portability, need the knowledge of chemistry and expert personal. To overcome the limitations of conventional techniques, electrochemical sensors have received significant attention in the field of heavy metal sensing due to its simplicity, cost-effectiveness, excellent sensitivity, low limit of detection, portability, and on-site analysis.

The sensing materials play a vital role in the efficient accumulation of target analytes as well as the performance of the electrochemical sensors. 2D materials are promising for different applications in the field of sensors, transistors, energy storage devices due to their intriguing properties. Among them, graphene has become a potential candidate for biosensors, electronic sensors, gas sensors, and electrochemical heavy metal ion sensors due to unique properties including higher electron mobility, high electrical conductivity, good thermal conductivity, large surface area, and excellent electrocatalytic activities. The layer structure and high surface area of graphene facilitate physical and chemical adsorption of different analytes through van der Waals interaction, electrostatic interaction, and covalent bonding. Further, various nanostructure materials including metal nanoparticles, metal nanorods, nanowires, metal oxide nanoparticles, conducting polymers, etc., have been introduced with graphene to form composites for improving the sensing performance due to their synergistic effects.

GO contains different functional groups on its surface including -COOH and C= O group at the edges and -OH and C-O-C on the basal plane. The presence of various oxygen-containing functional groups makes GO as a promising candidate for electrochemical sensing of Hg^{2+} by immobilizing Hg^{2+}. Recently, graphene or GO-based composites such as rGO-AuNPs, ionic liquid functionalized GO, 5-methyl-2-thiouracil (MTU)-AuNPs-GO, cysteamine-GO, L-Cysteine-rGO, SnO_2-rGO, and graphene quantum dots-AuNPs showed promises for electrochemical detection of Hg^{2+}. Unfortunately, most of them suffer from lower sensitivity, narrow detection range, and high detection limits. One possible reason is the poor conductivity of GO [17].

The development of an electrochemical sensor with excellent sensitivity and selectivity toward Hg^{2+} is needed to protect public health. It is essential to get faster electron transport between an electrode and the target analyte (Hg^{2+}) to improve the sensitivity of electrochemical sensors. AgNWs can provide faster electron transport between the electrode and electroactive analytes and hence, can improve the sensitivity of electrochemical sensors. With this into consideration, this work presents the incorporation of AgNWs to form a composite with GO and enhance the conductivity of GO by providing a faster electron transport pathway. The use of GO-AgNWs composite utilizes the advantages of the GO (large surface area, binding affinity towards Hg^{2+}) together with AgNWs (high conductivity). Here, a simple solution addition method was utilized to prepare GO-AgNWs composite. GO-AgNWs composite modified electrochemical sensors have been fabricated with a simple drop-cast method. The structure and morphology of GO-AgNWs composite were characterized using Raman spectroscopy, XRD, SEM, and TEM. The electrochemical characteristics of the GO-AgNWs composite modified electrodes were characterized using CV, EIS, and SWASV. Under optimum experimental conditions, the resulting sensor could detect Hg^{2+} with excellent sensitivity of ~ 0.29 µA/nM. The achieved linear response towards Hg^{2+} detection was in the range of 1-70 nM. Further, the detection limit of the GO-AgNWs composite modified electrode towards Hg^{2+} was ~ 0.1 nM. Therefore, our sensor can detect 5 nM Hg^{2+} which is the safety limit defined by the WHO and even less. The sensor has an excellent selective response to Hg^{2+} against other interfering heavy metal ions such as Pb^{2+}, Cd^{2+}, Cu^{2+}, Sn^{2+}, Ag^{+}, Cr^{3+}, and Na^{+}. The sensor exhibits high repeatability and reproducibility. The sensor is employed for the

detection of Hg^{2+} in tap water samples with an outstanding performance, suggesting it is a very promising platform for on-site monitoring of Hg^{2+} in water.

Inspired by graphene-based electrochemical sensors, 2D TMDs have recently attracted much attention because of large specific surface area, excellent electrical conductivity, and remarkable catalytic properties. Among them, WS_2 is one of the emerging TMDs that has two phases with different electronic structures and other properties. For instance, WS_2 with a 1T phase (octahedral O_h) is metallic, while the 2H phase (trigonal prismatic D_{3h}) is semiconducting. High conductivity and presence of sulfur groups (S^{2-}) having an affinity toward Hg^{2+} have made 1T-WS_2 a promising material for electrochemical sensing of Hg^{2+}. Some studies have also demonstrated the applicability of 2H-WS_2 for Hg^{2+} detection. Recently, Zuo et al. demonstrated a dual-color fluorescent biosensor using 2H-WS_2 nanosheets with Hg^{2+} and Ag^{+} specific DNA probes. The obtained LDRs for Hg^{2+} and Ag^{+} were 6.0-650.0 nM and 5.0-1000.0 nM with the LODs of 3.3 nM and 1.2 nM, respectively. Li and coworkers demonstrated a fluorescent sensor for Hg^{2+} using 2H-WS_2 nanosheets with T7 exonuclease. However, owing to limited fluorescence quenching ability of 2H-WS_2, these sensors suffer from narrow LDRs and high LODs. WS_2 based electrochemical sensors for Hg^{2+} are still suffering from low sensitivity, selectivity, and wide LDRs.

This work also focuses on the electrochemical detection of Hg^{2+} using metallic 1T-WS_2 microflowers. The flower-like WS_2 microstructure provides a high electroactive surface area for enhanced loading and rapid diffusion opportunity for Hg^{2+} ions. The metallic phase of 1T-WS_2 enhances the electrochemical properties by providing a fast-heterogeneous electron transfer rate. Moreover, the presence of abundant active sites on

both edge and basal planes of the 1T-WS_2 will further improve the electrocatalytic performances. Owing to the high electroactive surface area, good conductivity, fast heterogeneous electron transfer rate, and abundant active sites, the exploitation of 1T-WS_2 microflowers for electrochemical sensing of Hg^{2+} leads to wide LDRs with excellent sensitivity and selectivity.

Here, microflower structured metallic 1T-WS_2 was synthesized by a simple hydrothermal method and was further explored for Hg^{2+} detection. 1T-WS_2 microflowers modified electrochemical sensors have been fabricated with a simple drop-cast method. The structure and morphology of 1T-WS_2 microflowers were characterized using Raman spectroscopy, XRD, SEM, TEM. The electrochemical characteristics of the 1T-WS_2 modified electrodes were characterized using CV, EIS, and SWASV. The sensor showed excellent sensitivities of ~ 15.9 µA/µM, 2.54 µA/µM, 13.84 µA/µM, and 0.04646 µA/µM for Hg^{2+} with LDRs of 1-90 nM, 0.1-0.4 µM, 0.5-1.0 µM, and 0.1-1.0 mM, respectively. In addition to this, the LOD of the sensor toward Hg^{2+} is 0.0798 nM or 79.8 pM, which is well below the acceptable limit of Hg^{2+} in water defined by WHO and EPA. The sensor exhibits excellent selectivity for Hg^{2+} against other heavy metal ions including Cu^{2+}, Fe^{3+}, Ni^{2+}, Pb^{2+}, Cr^{3+}, K^{+}, Na^{+}, Ag^{+}, Sn^{2+}, and Cd^{2+}. The thus obtained excellent sensitivity and selectivity with wide LDRs can be attributed to the high conductivity, large surface area microflower structured 1T-WS_2, and the complexation of Hg^{2+} ions with sulfur (S^{2-}). In addition to good repeatability, reproducibility, and stability, this sensor shows the practical feasibility of Hg^{2+} detection in tap water suggesting a promising device for real applications.

5.2 Conclusions

In the first project, a GO-AgNWs composite modified high-performance Hg^{2+} sensor was successfully developed. The GO-AgNWs composite greatly facilitates faster electron-transfer kinetics and leads to improved sensing of Hg^{2+}. The outcomes reveal that the GO-AgNWs composite modified sensor is highly sensitive to Hg^{2+} in the range of 1 - 70 nM and the LOD is ~ 0.1 nM. Due to the formation of R-COO-Hg^{2+}-COO-R linkage, the sensor showed a strong affinity to Hg^{2+}, while other heavy metal ions had no interference. Moreover, the sensor exhibited excellent repeatability, reproducibility, and applicability for the determination of Hg^{2+} in tap water.

In the second project, 1T-WS_2 microflowers were hydrothermally synthesized and XRD, Raman spectroscopy, SEM, and TEM were utilized to verify its structural and morphological characteristics. Electrochemical characterization using CV and EIS exhibited that the 1T-WS_2 modified GCE greatly facilitated faster electron transport because of the metallic phase of WS_2. Stripping responses under the optimized experimental conditions demonstrated that the as-prepared 1T-WS_2 modified GCE can be successfully employed to detect Hg^{2+} with ultra-trace sensitivity and wide LDRs. The estimated LOD for Hg^{2+} was 79.8 pM which is well below the acceptable limit of Hg^{2+} in drinking water. Because of the strong affinity of S^{2-} toward Hg^{2+}, selective detection of Hg^{2+} was achieved against other metal ions. The reason for the superior sensing performance can be attributed to the excellent electronic conductivity, large surface area, and microflower structure of 1T-WS_2 with strong interactions between the S^{2-} groups of WS_2 and Hg^{2+}. The high recovery between 96% to 99.6% also demonstrated that the sensor can be used for determining Hg^{2+} in tap water with high accuracy and reliability. All the

results suggest that the 1T-WS_2 modified GCE has the potential to be an efficient approach for on-field detection of Hg^{2+} in real samples.

5.3 Future Work

The developed sensor work could be extended to make it field deployable. These sensors could be fabricated on screen printed electrodes to make it portable for on-field analysis of heavy metals. Simultaneous and rapid detection of multiple heavy metals including Hg^{2+}, Pb^{2+}, Cd^{2+}, and As^{+} with high sensitivity is still challenging due to lack of effective sensing material and devices. To address these problems, different nanomaterials including L-cysteine can be immobilized on GO surface for simultaneous detection of Hg^{2+}, Pb^{2+}, Cd^{2+}, As^{+} with a single sensor. To enhance the sensitivity and selectivity, specific enzyme or biomolecules can be incorporated into GO composites. For rapid detection, electrochemical FET-based sensors can be developed using microfabrication. The FET-based sensor devices would provide simultaneous detection of multiple heavy metals within a few seconds.

REFERENCES

[1] M. B. Gumpu, S. Sethuraman, U. M. Krishnan, and J. B. B. Rayappan, "A review on detection of heavy metal ions in water–an electrochemical approach," *Sensors and Actuators B: Chemical,* vol. 213, pp. 515-533, 2015.

[2] A. Ambrosi, C. K. Chua, A. Bonanni, and M. Pumera, "Electrochemistry of graphene and related materials," *Chemical reviews,* vol. 114, no. 14, pp. 7150-7188, 2014.

[3] N. Tekaya, O. Saiapina, H. B. Ouada, F. Lagarde, H. B. Ouada, and N. Jaffrezic-Renault, "Ultra-sensitive conductometric detection of pesticides based on inhibition of esterase activity in Arthrospira platensis," *Environmental pollution,* vol. 178, pp. 182-188, 2013.

[4] F. Ge, M.-M. Li, H. Ye, and B.-X. Zhao, "Effective removal of heavy metal ions Cd2+, Zn2+, Pb2+, Cu2+ from aqueous solution by polymer-modified magnetic nanoparticles," *Journal of Hazardous Materials,* vol. 211-212, pp. 366-372, 2012/04/15/ 2012.

[5] B. Bansod, T. Kumar, R. Thakur, S. Rana, and I. Singh, "A review on various electrochemical techniques for heavy metal ions detection with different sensing platforms," *Biosensors and Bioelectronics,* vol. 94, pp. 443-455, 2017.

[6] L. Zhu, L. Xu, B. Huang, N. Jia, L. Tan, and S. Yao, "Simultaneous determination of Cd(II) and Pb(II) using square wave anodic stripping voltammetry at a gold nanoparticle-graphene-cysteine composite modified bismuth film electrode," *Electrochimica Acta,* vol. 115, pp. 471-477, 2014.

[7] Y. Wei *et al.*, "SnO2/reduced graphene oxide nanocomposite for the simultaneous electrochemical detection of cadmium (II), lead (II), copper (II), and mercury (II): an interesting favorable mutual interference," *The journal of physical chemistry C,* vol. 116, no. 1, pp. 1034-1041, 2011.

[8] S. Ekino, T. Ninomiya, and M. Susa, "The chemical form of mercury in fish," *Science,* vol. 303, no. 5659, pp. 763-764, 2004.

[9] J. S. Lee, M. S. Han, and C. A. Mirkin, "Colorimetric detection of mercuric ion (Hg2+) in aqueous media using DNA-functionalized gold nanoparticles," *Angewandte Chemie International Edition,* vol. 46, no. 22, pp. 4093-4096, 2007.

[10] L. Patrick, "Lead toxicity part II: the role of free radical damage and the use of antioxidants in the pathology and treatment of lead toxicity," *Alternative medicine review,* vol. 11, no. 2, 2006.

[11] N. Ercal, H. Gurer-Orhan, and N. Aykin-Burns, "Toxic metals and oxidative stress part I: mechanisms involved in metal-induced oxidative damage," *Current topics in medicinal chemistry,* vol. 1, no. 6, pp. 529-539, 2001.

[12] A. B. Kobal *et al.*, "The impact of long-term past exposure to elemental mercury on antioxidative capacity and lipid peroxidation in mercury miners," *Journal of Trace Elements in Medicine and Biology,* vol. 17, no. 4, pp. 261-274, 2004.

[13] M. Valko, H. Morris, and M. Cronin, "Metals, toxicity and oxidative stress," *Current medicinal chemistry,* vol. 12, no. 10, pp. 1161-1208, 2005.

[14] H. Gong and X. Li, "Y-type, C-rich DNA probe for electrochemical detection of silver ion and cysteine," *Analyst,* vol. 136, no. 11, pp. 2242-2246, 2011.

[15] M. Hashemi, S. Ghavami, M. Eshraghi, E. P. Booy, and M. Los, "Cytotoxic effects of intra and extracellular zinc chelation on human breast cancer cells," *European journal of pharmacology,* vol. 557, no. 1, pp. 9-19, 2007.

[16] S. Selvaraj, S. Krishnaswamy, V. Devashya, S. Sethuraman, and U. M. Krishnan, "Investigations on membrane perturbation by chrysin and its copper complex using self-assembled lipid bilayers," *Langmuir,* vol. 27, no. 21, pp. 13374-13382, 2011.

[17] M. T. Rahman *et al.*, "Graphene Oxide–Silver Nanowire Nanocomposites for Enhanced Sensing of Hg2+," *ACS Applied Nano Materials,* vol. 2, no. 8, pp. 4842-4851, 2019.

[18] K. Huang, B. Li, F. Zhou, S. Mei, Y. Zhou, and T. Jing, "Selective solid-phase extraction of lead ions in water samples using three-dimensional ion-imprinted polymers," *Analytical chemistry,* vol. 88, no. 13, pp. 6820-6826, 2016.

[19] S. Bian *et al.*, "One-pot synthesis of sulfur-doped graphene quantum dots as a novel fluorescent probe for highly selective and sensitive detection of lead (II)," *Rsc Advances,* vol. 6, no. 74, pp. 69977-69983, 2016.

[20] B. Zhang *et al.*, "Facile and green fabrication of size-controlled AuNPs/CNFs hybrids for the highly sensitive simultaneous detection of heavy metal ions," *Electrochimica Acta,* vol. 196, pp. 422-430, 2016.

[21] Y. Zhou, S. Wang, K. Zhang, and X. Jiang, "Visual detection of copper (II) by azide-and alkyne-functionalized gold nanoparticles using click chemistry," *Angewandte Chemie,* vol. 120, no. 39, pp. 7564-7566, 2008.

[22] M. A. R. Laskar, M. T. Rahman, A. A. Maruf, and Q. Qiao, "Instantaneous Colorimetric Visual Detection of Toxic Lead (II) ions," *Bulletin of the American Physical Society,* 2020.

[23] H. Bagheri, A. Afkhami, M. Saber-Tehrani, and H. Khoshsafar, "Preparation and characterization of magnetic nanocomposite of Schiff base/silica/magnetite as a preconcentration phase for the trace determination of heavy metal ions in water, food and biological samples using atomic absorption spectrometry," *Talanta,* vol. 97, pp. 87-95, 2012.

[24] T. Swanston *et al.*, "Synchrotron X-ray fluorescence imaging evidence of biogenic mercury identified in a burial in colonial Antigua," *Journal of Archaeological Science,* vol. 58, pp. 26-30, 2015.

[25] J.-P. Cornard, A. Caudron, and J.-C. Merlin, "UV–visible and synchronous fluorescence spectroscopic investigations of the complexation of Al (III) with caffeic acid, in aqueous low acidic medium," *Polyhedron,* vol. 25, no. 11, pp. 2215-2222, 2006.

[26] S. Arpadjan, G. Celik, S. Taşkesen, and Ş. Güçer, "Arsenic, cadmium and lead in medicinal herbs and their fractionation," *Food and chemical toxicology,* vol. 46, no. 8, pp. 2871-2875, 2008.

[27] K. Bhat, J. Arunachalam, S. Yegnasubramanian, and S. Gangadharan, "Trace elements in hair and environmental exposure," *Science of the Total Environment,* vol. 22, no. 2, pp. 169-178, 1982.

[28] G. Sener, L. Uzun, and A. Denizli, "Colorimetric Sensor Array Based on Gold Nanoparticles and Amino Acids for Identification of Toxic Metal Ions in Water," *ACS Applied Materials & Interfaces,* vol. 6, no. 21, pp. 18395-18400, 2014/11/12 2014.

[29] Z. Wang *et al.*, "Fluorescence sensor array based on amino acid derived carbon dots for pattern-based detection of toxic metal ions," *Sensors and Actuators B: Chemical,* vol. 241, pp. 1324-1330, 2017.

[30] Y. Ma, H. Liu, K. Qian, L. Yang, and J. Liu, "A displacement principle for mercury detection by optical waveguide and surface enhanced Raman spectroscopy," *Journal of colloid and interface science,* vol. 386, no. 1, pp. 451-455, 2012.

[31] W. Zeng, Y. Chen, H. Cui, F. Wu, Y. Zhu, and J. S. Fritz, "Single-column method of ion chromatography for the determination of common cations and some transition metals," *Journal of Chromatography A,* vol. 1118, no. 1, pp. 68-72, 2006.

[32] L. Zhao, S. Zhong, K. Fang, Z. Qian, and J. Chen, "Determination of cadmium (II), cobalt (II), nickel (II), lead (II), zinc (II), and copper (II) in water samples using dual-cloud point

extraction and inductively coupled plasma emission spectrometry," *Journal of hazardous materials,* vol. 239, pp. 206-212, 2012.

[33] A. Sánchez-Calvo, M. T. Fernández-Abedul, M. C. Blanco-López, and A. Costa-García, "Paper-based electrochemical transducer modified with nanomaterials for mercury determination in environmental waters," *Sensors and Actuators B: Chemical,* vol. 290, pp. 87-92, 2019/07/01/ 2019.

[34] M. Lu *et al.*, "Graphene Aerogel–Metal–Organic Framework-Based Electrochemical Method for Simultaneous Detection of Multiple Heavy-Metal Ions," *Analytical chemistry,* vol. 91, no. 1, pp. 888-895, 2018.

[35] M. F. Kabir, M. T. Rahman, A. Gurung, and Q. Qiao, "Electrochemical phosphate sensors using silver nanowires treated screen printed electrodes," *IEEE Sensors Journal,* vol. 18, no. 9, pp. 3480-3485, 2018.

[36] M. T. Rahman, M. F. Kabir, and Q. Qiao, "Electrochemical Phosphate Sensors Using Silver Nanowires Treated Screen Printed Electrodes," in *2018 IEEE International Conference on Electro/Information Technology (EIT)*, 2018, pp. 0993-0997: IEEE.

[37] D. Jadreško and M. Lovrić, "A theory of square-wave voltammetry of surface-active, electroinactive compounds," *Electrochimica Acta,* vol. 53, no. 27, pp. 8045-8050, 2008.

[38] Z. Li, S. Xia, J. Wang, C. Bian, and J. Tong, "Determination of trace mercury in water based on N-octylpyridinium ionic liquids preconcentration and stripping voltammetry," *Journal of hazardous materials,* vol. 301, pp. 206-213, 2016.

[39] M. Lovrić and Š. Komorsky-Lovrić, "Theory of square wave voltammetry of three step electrode reaction," *Journal of Electroanalytical Chemistry,* vol. 735, pp. 90-94, 2014.

[40] Z. Rafiei-Sarmazdeh, S. M. Zahedi-Dizaji, and A. K. Kang, "Two-Dimensional Nanomaterials," in *Nanostructures*: IntechOpen, 2019.

[41] A. Lerf, H. He, M. Forster, and J. Klinowski, "Structure of graphite oxide revisited," *The Journal of Physical Chemistry B,* vol. 102, no. 23, pp. 4477-4482, 1998.

[42] M. T. Rahman, A. K. Roy, H. M. A. R. Bhuiyan, M. T. Islam, and A. G. Bhuiyan, "DC characteristics of dual gated large area graphene MOSFET," in *2013 International Conference on Electrical Information and Communication Technology (EICT)*, 2014, pp. 1-6: IEEE.

[43] M. Fahim-Al-Fattah, M. T. Rahman, M. S. Islam, A. Bhuiyan, and A. A. Khan, "DC and RF characteristics of graphene FET using analytical approach," in *2015 International Conference on Electrical Engineering and Information Communication Technology (ICEEICT)*, 2015, pp. 1-4: IEEE.

[44] A. K. Geim and K. S. Novoselov, "The rise of graphene," in *Nanoscience and technology: a collection of reviews from nature journals*: World Scientific, 2010, pp. 11-19.

[45] A. Grüneis *et al.*, "Tight-binding description of the quasiparticle dispersion of graphite and few-layer graphene," *Physical Review B,* vol. 78, no. 20, p. 205425, 2008.

[46] M. Fahim-Al-Fattah, M. T. Rahman, M. S. Islam, and A. G. Bhuiyan, "A Study on Theoretical Performance of Graphene FET using Analytical Approach with Reference to High Cutoff Frequency," *International Journal of Nanoscience,* vol. 15, no. 03, p. 1640001, 2016.

[47] M. S. Islam, M. T. Rahman, A. Bhuiyan, and A. Hashimoto, "Vacancy induced phonon properties of hydrogen passivated graphene," in *2013 International Conference on Electrical Information and Communication Technology (EICT)*, 2014, pp. 1-5: IEEE.

[48] J. Zhu, D. Yang, Z. Yin, Q. Yan, and H. Zhang, "Graphene and graphene-based materials for energy storage applications," *Small,* vol. 10, no. 17, pp. 3480-3498, 2014.

[49] Q. He, S. Wu, Z. Yin, and H. Zhang, "Graphene-based electronic sensors," *Chemical Science,* vol. 3, no. 6, pp. 1764-1772, 2012.
[50] C. Lee, X. Wei, J. W. Kysar, and J. Hone, "Measurement of the elastic properties and intrinsic strength of monolayer graphene," *science,* vol. 321, no. 5887, pp. 385-388, 2008.
[51] M. T. Rahman, M. A. R. Laskar, A. A. Maruf, and Q. Qiao, "Silver Nanowires Functionalized Graphene Oxide Based Biosensor for Trace level Detection of Mercury Ions," *Bulletin of the American Physical Society,* 2020.
[52] M. S. Islam, M. T. Rahaman, A. G. Bhuiyan, and A. Hashimoto, "Numerical Analysis on Phonon Localization of Vacancy Type Disordered Graphene," *Journal of Circuits, Systems and Computers,* vol. 24, no. 02, p. 1540002, 2015.
[53] K. S. Novoselov *et al.*, "Electric field effect in atomically thin carbon films," *science,* vol. 306, no. 5696, pp. 666-669, 2004.
[54] M. S. Hassan and M. T. Rahman, "Effect of Impact Ionization and Carrier Multiplication on Graphene MOSFET at different dimensions," *Google Scholar There is no corresponding record for this reference*.
[55] D. Chen, H. Feng, and J. Li, "Graphene oxide: preparation, functionalization, and electrochemical applications," *Chemical reviews,* vol. 112, no. 11, pp. 6027-6053, 2012.
[56] W. S. Hummers Jr and R. E. Offeman, "Preparation of graphitic oxide," *Journal of the american chemical society,* vol. 80, no. 6, pp. 1339-1339, 1958.
[57] G. Eda and M. Chhowalla, "Chemically derived graphene oxide: towards large-area thin-film electronics and optoelectronics," *Advanced materials,* vol. 22, no. 22, pp. 2392-2415, 2010.
[58] F. Kim, L. J. Cote, and J. Huang, "Graphene Oxide: Surface Activity and Two-Dimensional Assembly," *Advanced Materials,* vol. 22, no. 17, pp. 1954-1958, 2010.
[59] X. Li *et al.*, "Highly conducting graphene sheets and Langmuir–Blodgett films," *Nature nanotechnology,* vol. 3, no. 9, p. 538, 2008.
[60] A. C. Neto, F. Guinea, N. M. Peres, K. S. Novoselov, and A. K. Geim, "The electronic properties of graphene," *Reviews of modern physics,* vol. 81, no. 1, p. 109, 2009.
[61] S. Aldrich. *Graphene oxide nanocolloids* Available: https://www.sigmaaldrich.com/catalog/product/aldrich/795534?lang=en&region=US&cm_sp=Insite-_-caContent_prodMerch_raiOtherymlCtr-_-prodMerch10-3
[62] L. J. Cote, F. Kim, and J. Huang, "Langmuir− Blodgett assembly of graphite oxide single layers," *Journal of the American Chemical Society,* vol. 131, no. 3, pp. 1043-1049, 2009.
[63] Q. H. Wang, K. Kalantar-Zadeh, A. Kis, J. N. Coleman, and M. S. Strano, "Electronics and optoelectronics of two-dimensional transition metal dichalcogenides," *Nature nanotechnology,* vol. 7, no. 11, p. 699, 2012.
[64] Q. He *et al.*, "Fabrication of flexible MoS2 thin-film transistor arrays for practical gas-sensing applications," *Small,* vol. 8, no. 19, pp. 2994-2999, 2012.
[65] K. F. Mak, C. Lee, J. Hone, J. Shan, and T. F. Heinz, "Atomically thin MoS 2: a new direct-gap semiconductor," *Physical review letters,* vol. 105, no. 13, p. 136805, 2010.
[66] A. Splendiani *et al.*, "Emerging photoluminescence in monolayer MoS2," *Nano letters,* vol. 10, no. 4, pp. 1271-1275, 2010.
[67] M. Chhowalla, H. S. Shin, G. Eda, L.-J. Li, K. P. Loh, and H. Zhang, "The chemistry of two-dimensional layered transition metal dichalcogenide nanosheets," *Nature chemistry,* vol. 5, no. 4, p. 263, 2013.
[68] L. J. Sevin, "Field-effect transistors," 1965.

[69] H. Eren and J. G. Webster, "Measurement, Instrumentation, and Sensors Handbook: Electromagnetic, Optical, Radiation, Chemical, and Biomedical Measurement," 2014.
[70] B. Radisavljevic, A. Radenovic, J. Brivio, V. Giacometti, and A. Kis, "Single-layer MoS 2 transistors," *Nature nanotechnology,* vol. 6, no. 3, p. 147, 2011.
[71] Z. Zeng *et al.*, "Single-Layer Semiconducting Nanosheets: High-yield preparation and device fabrication," *Angewandte Chemie International Edition,* vol. 50, no. 47, pp. 11093-11097, 2011.
[72] Z. Zeng *et al.*, "An effective method for the fabrication of few-layer-thick inorganic nanosheets," *Angewandte Chemie International Edition,* vol. 51, no. 36, pp. 9052-9056, 2012.
[73] S. Wu *et al.*, "Electrochemically reduced single-layer MoS2 nanosheets: Characterization, properties, and sensing applications," *Small,* vol. 8, no. 14, pp. 2264-2270, 2012.
[74] J. Ping, Z. Fan, M. Sindoro, Y. Ying, and H. Zhang, "Recent advances in sensing applications of two-dimensional transition metal dichalcogenide nanosheets and their composites," *Advanced Functional Materials,* vol. 27, no. 19, p. 1605817, 2017.
[75] T. Wang, R. Zhu, J. Zhuo, Z. Zhu, Y. Shao, and M. Li, "Direct detection of DNA below ppb level based on thionin-functionalized layered MoS2 electrochemical sensors," *Analytical chemistry,* vol. 86, no. 24, pp. 12064-12069, 2014.
[76] J. Tang *et al.*, "Three-dimensional WS 2 nanosheet networks for H 2 O 2 produced for cell signaling," *Nanoscale,* vol. 8, no. 10, pp. 5786-5792, 2016.
[77] Z. Hu, Z. Wu, C. Han, J. He, Z. Ni, and W. Chen, "Two-dimensional transition metal dichalcogenides: interface and defect engineering," *Chemical Society Reviews,* vol. 47, no. 9, pp. 3100-3128, 2018.
[78] N. Rohaizad, C. C. Mayorga-Martinez, Z. k. Sofer, and M. Pumera, "1T-phase transition metal dichalcogenides (MoS2, MoSe2, WS2, and WSe2) with fast heterogeneous electron transfer: application on second-generation enzyme-based biosensor," *ACS applied materials & interfaces,* vol. 9, no. 46, pp. 40697-40706, 2017.
[79] B. Mahler, V. Hoepfner, K. Liao, and G. A. Ozin, "Colloidal synthesis of 1T-WS2 and 2H-WS2 nanosheets: applications for photocatalytic hydrogen evolution," *Journal of the American Chemical Society,* vol. 136, no. 40, pp. 14121-14127, 2014.
[80] A. Khalil *et al.*, "Metallic 1T-WS 2 nanoribbons as highly conductive electrodes for supercapacitors," *RSC Advances,* vol. 6, no. 54, pp. 48788-48791, 2016.
[81] R. Aswathi and K. Sandhya, "Ultrasensitive and selective electrochemical sensing of Hg (II) ions in normal and sea water using solvent exfoliated MoS 2: affinity matters," *Journal of Materials Chemistry A,* vol. 6, no. 30, pp. 14602-14613, 2018.
[82] X. Zuo, H. Zhang, Q. Zhu, W. Wang, J. Feng, and X. Chen, "A dual-color fluorescent biosensing platform based on WS2 nanosheet for detection of Hg2+ and Ag+," *Biosensors and Bioelectronics,* vol. 85, pp. 464-470, 2016.
[83] S. Xu, D. Li, and P. Wu, "One-pot, facile, and versatile synthesis of monolayer MoS2/WS2 quantum dots as bioimaging probes and efficient electrocatalysts for hydrogen evolution reaction," *Advanced Functional Materials,* vol. 25, no. 7, pp. 1127-1136, 2015.
[84] C. Feng, L. Huang, Z. Guo, and H. Liu, "Synthesis of tungsten disulfide (WS2) nanoflakes for lithium ion battery application," *Electrochemistry communications,* vol. 9, no. 1, pp. 119-122, 2007.
[85] Q. Liu *et al.*, "Stable metallic 1T-WS2 nanoribbons intercalated with ammonia ions: the correlation between structure and electrical/optical properties," *Advanced Materials,* vol. 27, no. 33, pp. 4837-4844, 2015.

[86] H. Y. Yue *et al.*, "Electrochemical determination of dopamine in the presence of uric acid using WS2 nanospheres-carbon nanofibers," *Journal of Electroanalytical Chemistry,* vol. 833, pp. 427-432, 2019.

[87] R.-L. Zong *et al.*, "Synthesis and optical properties of silver nanowire arrays embedded in anodic alumina membrane," *The Journal of Physical Chemistry B,* vol. 108, no. 43, pp. 16713-16716, 2004.

[88] S. L.-C. Hsu and R.-T. Wu, "Synthesis of contamination-free silver nanoparticle suspensions for micro-interconnects," *Materials Letters,* vol. 61, no. 17, pp. 3719-3722, 2007.

[89] A. D. McFarland and R. P. Van Duyne, "Single silver nanoparticles as real-time optical sensors with zeptomole sensitivity," *Nano letters,* vol. 3, no. 8, pp. 1057-1062, 2003.

[90] R. Chimentao *et al.*, "Different morphologies of silver nanoparticles as catalysts for the selective oxidation of styrene in the gas phase," *Chemical communications,* no. 7, pp. 846-847, 2004.

[91] Y. Lu, M. Yang, F. Qu, G. Shen, and R. Yu, "Enzyme-functionalized gold nanowires for the fabrication of biosensors," *Bioelectrochemistry,* vol. 71, no. 2, pp. 211-216, 2007.

[92] X. Gao, L. Jin, Q. Wu, Z. Chen, and X. Lin, "A nonenzymatic hydrogen peroxide sensor based on silver nanowires and chitosan film," *Electroanalysis,* vol. 24, no. 8, pp. 1771-1777, 2012.

[93] L. Wang, X. Gao, L. Jin, Q. Wu, Z. Chen, and X. Lin, "Amperometric glucose biosensor based on silver nanowires and glucose oxidase," *Sensors and Actuators B: Chemical,* vol. 176, pp. 9-14, 2013.

[94] J. Wang *et al.*, "Electrostatic assembly of peptide nanofiber–biomimetic silver nanowires onto graphene for electrochemical sensors," *ACS Macro Letters,* vol. 3, no. 6, pp. 529-533, 2014.

[95] M. D. Ho *et al.*, "Percolating network of ultrathin gold nanowires and silver nanowires toward “invisible” wearable sensors for detecting emotional expression and apexcardiogram," *Advanced Functional Materials,* vol. 27, no. 25, p. 1700845, 2017.

[96] S. Chen, Y. Wei, S. Wei, Y. Lin, and L. Liu, "Ultrasensitive cracking-assisted strain sensors based on silver nanowires/graphene hybrid particles," *ACS applied materials & interfaces,* vol. 8, no. 38, pp. 25563-25570, 2016.

[97] S. Kumar-Krishnan *et al.*, "Chitosan supported silver nanowires as a platform for direct electrochemistry and highly sensitive electrochemical glucose biosensing," *RSC advances,* vol. 6, no. 24, pp. 20102-20108, 2016.

[98] *Silver nanowires guide electricity and light in nanophotonic circuits*. Available: https://www.laserfocusworld.com/lasers-sources/article/16564455/silver-nanowires-guide-electricity-and-light-in-nanophotonic-circuits

[99] *Graphene-Silver nanowires builds future touch screen*. Available: http://www.graphene-uses.com/graphene-silver-nanowires-builds-future-touch-screen/

[100] *Stretchable nanowire mesh heats your sore muscles*. Available: https://www.engadget.com/2015-07-05-stretchable-nanowire-heating-mesh.html

[101] *Silver Nanowires Antibacterial*. Available: https://www.nanoshel.com/product/silver-nanowires-antibacterial

[102] P. Blake *et al.*, "Graphene-based liquid crystal device," *Nano letters,* vol. 8, no. 6, pp. 1704-1708, 2008.

[103] J. Liu, S. Fu, B. Yuan, Y. Li, and Z. Deng, "Toward a universal “adhesive nanosheet” for the assembly of multiple nanoparticles based on a protein-induced

reduction/decoration of graphene oxide," *Journal of the American Chemical Society,* vol. 132, no. 21, pp. 7279-7281, 2010.

[104] G. Williams, B. Seger, and P. V. Kamat, "TiO2-graphene nanocomposites. UV-assisted photocatalytic reduction of graphene oxide," *ACS nano,* vol. 2, no. 7, pp. 1487-1491, 2008.

[105] J. Gong, T. Zhou, D. Song, and L. Zhang, "Monodispersed Au nanoparticles decorated graphene as an enhanced sensing platform for ultrasensitive stripping voltammetric detection of mercury (II)," *Sensors and Actuators B: Chemical,* vol. 150, no. 2, pp. 491-497, 2010.

[106] K. Liu, S. Chen, Y. Luo, and L. Liu, "Hybrid of silver nanowire and pristine-graphene by liquid-phase exfoliation for synergetic effects on electrical conductive composites," *RSC Advances,* vol. 4, no. 79, pp. 41876-41885, 2014.

[107] P. S. Chandrasekhar *et al.*, "Plasmonic silver nanowires for higher efficiency dye-sensitized solar cells," *Materials Today Energy,* vol. 5, pp. 237-242, 2017/09/01/ 2017.

[108] B. Vaagensmith and Q. Qiao, "Effect of Synthesis Temperature, UV-Ozone Treatment, and Nanowire Diameter on the Failure of Silver Nanowire Electrodes," *IEEE Journal of Photovoltaics,* vol. 6, no. 6, pp. 1549-1553, 2016.

[109] J. Li, S. Guo, Y. Zhai, and E. Wang, "High-sensitivity determination of lead and cadmium based on the Nafion-graphene composite film," *Analytica chimica acta,* vol. 649, no. 2, pp. 196-201, 2009.

[110] J. Li, S. Guo, Y. Zhai, and E. Wang, "Nafion–graphene nanocomposite film as enhanced sensing platform for ultrasensitive determination of cadmium," *Electrochemistry Communications,* vol. 11, no. 5, pp. 1085-1088, 2009.

[111] R. J. Grim, "Catalytic Activity of an Intermetallic Compound of Cadmium and Copper in the Vapor-phase Reduction of Nitrobenzene," *The Journal of Physical Chemistry,* vol. 46, no. 4, pp. 464-469, 1942.

[112] A. Ben-Bassat and A. Azrad, "Intermetallic compounds formed in mixed (complex) amalgams—I. The systems: copper—mercury, zinc—mercury and copper—zinc—mercury," *Electrochimica Acta,* vol. 23, no. 1, pp. 63-69, 1978.

[113] S. L. Ting, S. J. Ee, A. Ananthanarayanan, K. C. Leong, and P. Chen, "Graphene quantum dots functionalized gold nanoparticles for sensitive electrochemical detection of heavy metal ions," *Electrochimica Acta,* vol. 172, pp. 7-11, 2015.

[114] N. Zhou, J. Li, H. Chen, C. Liao, and L. Chen, "A functional graphene oxide-ionic liquid composites–gold nanoparticle sensing platform for ultrasensitive electrochemical detection of Hg 2+," *Analyst,* vol. 138, no. 4, pp. 1091-1097, 2013.

[115] S. Muralikrishna, K. Sureshkumar, T. S. Varley, D. H. Nagaraju, and T. Ramakrishnappa, "In situ reduction and functionalization of graphene oxide with L-cysteine for simultaneous electrochemical determination of cadmium (II), lead (II), copper (II), and mercury (II) ions," *Analytical Methods,* vol. 6, no. 21, pp. 8698-8705, 2014.

[116] N. Wang, M. Lin, H. Dai, and H. Ma, "Functionalized gold nanoparticles/reduced graphene oxide nanocomposites for ultrasensitive electrochemical sensing of mercury ions based on thymine–mercury–thymine structure," *Biosensors and Bioelectronics,* vol. 79, pp. 320-326, 2016.

[117] Y. Zhang *et al.*, "Electrochemical sensor based on electrodeposited graphene-Au modified electrode and nanoAu carrier amplified signal strategy for attomolar mercury detection," *Analytical chemistry,* vol. 87, no. 2, pp. 989-996, 2015.

[118] Y. Zhang *et al.*, "Simple and signal-off electrochemical biosensor for mercury (II) based on thymine-mercury-thymine hybridization directly on graphene," *Electrochimica Acta,* vol. 170, pp. 210-217, 2015.
[119] G.-L. Wen *et al.*, "N-doped reduced graphene oxide/MnO2 nanocomposite for electrochemical detection of Hg2+ by square wave stripping voltammetry," *Electrochimica Acta,* vol. 291, pp. 95-102, 2018.
[120] K. Chen *et al.*, "Hg (II) ion detection using thermally reduced graphene oxide decorated with functionalized gold nanoparticles," *Analytical chemistry,* vol. 84, no. 9, pp. 4057-4062, 2012.
[121] T. Zhang *et al.*, "Self-assembled 1-octadecanethiol monolayers on graphene for mercury detection," *Nano letters,* vol. 10, no. 11, pp. 4738-4741, 2010.
[122] H. G. Sudibya, Q. He, H. Zhang, and P. Chen, "Electrical detection of metal ions using field-effect transistors based on micropatterned reduced graphene oxide films," *ACS nano,* vol. 5, no. 3, pp. 1990-1994, 2011.
[123] D. S.-H. Chan, H.-M. Lee, C.-M. Che, C.-H. Leung, and D.-L. Ma, "A selective oligonucleotide-based luminescent switch-on probe for the detection of nanomolar mercury (II) ion in aqueous solution," *Chemical Communications,* no. 48, pp. 7479-7481, 2009.
[124] N. Kanayama, T. Takarada, and M. Maeda, "Rapid naked-eye detection of mercury ions based on non-crosslinking aggregation of double-stranded DNA-carrying gold nanoparticles," *Chemical Communications,* vol. 47, no. 7, pp. 2077-2079, 2011.
[125] Y. Xu *et al.*, "Metal-induced aggregation of mononucleotides-stabilized gold nanoparticles: an efficient approach for simple and rapid colorimetric detection of Hg (II)," *Chemical Communications,* vol. 47, no. 21, pp. 6039-6041, 2011.
[126] A. M. Golsheikh, N. Huang, H. Lim, and R. Zakaria, "One-pot sonochemical synthesis of reduced graphene oxide uniformly decorated with ultrafine silver nanoparticles for non-enzymatic detection of H 2 O 2 and optical detection of mercury ions," *Rsc Advances,* vol. 4, no. 69, pp. 36401-36411, 2014.
[127] J. Ge *et al.*, "Highly sensitive fluorescence detection of mercury (II) ions based on WS2 nanosheets and T7 exonuclease assisted cyclic enzymatic amplification," *Sensors and Actuators B: Chemical,* vol. 249, pp. 189-194, 2017.
[128] N. Kamaruddin, A. A. Bakar, N. Mobarak, M. S. Zan, and N. Arsad, "Binding affinity of a highly sensitive Au/Ag/Au/chitosan-graphene oxide sensor based on direct detection of Pb2+ and Hg2+ ions," *Sensors,* vol. 17, no. 10, p. 2277, 2017.
[129] S. Jiang, R. Cheng, R. Ng, Y. Huang, and X. Duan, "Highly sensitive detection of mercury (II) ions with few-layer molybdenum disulfide," *Nano Research,* vol. 8, no. 1, pp. 257-262, 2015.
[130] G. Zhou *et al.*, "Ultrasensitive mercury ion detection using DNA-functionalized molybdenum disulfide nanosheet/gold nanoparticle hybrid field-effect transistor device," *ACS Sensors,* vol. 1, no. 3, pp. 295-302, 2016.
[131] A. Nigam *et al.*, "Real time detection of Hg2+ ions using MoS2 functionalized AlGaN/GaN high electron mobility transistor for water quality monitoring," *Sensors and Actuators B: Chemical,* vol. 309, p. 127832, 2020.
[132] W. Li *et al.*, "Flowerlike WSe 2 and WS 2 microspheres: one-pot synthesis, formation mechanism and application in heavy metal ion sequestration," *Chemical communications,* vol. 52, no. 24, pp. 4481-4484, 2016.

[133] X. Li, J. Liu, X. Gong, T. Qing, P. Zhang, and B. Feng, "Synthesis of fluorescent tungsten disulfide by nitrogen atom doping and its application for mercury (ii) detection," *Journal of Materials Chemistry C,* vol. 7, no. 14, pp. 4096-4101, 2019.

[134] D. Voiry *et al.*, "Conducting MoS2 nanosheets as catalysts for hydrogen evolution reaction," *Nano letters,* vol. 13, no. 12, pp. 6222-6227, 2013.

[135] K. Chang *et al.*, "Targeted Synthesis of 2H-and 1T-Phase MoS2 Monolayers for Catalytic Hydrogen Evolution," *Advanced Materials,* vol. 28, no. 45, pp. 10033-10041, 2016.

[136] A. J. Bard, L. R. Faulkner, J. Leddy, and C. G. Zoski, *Electrochemical methods: fundamentals and applications*. wiley New York, 1980.

[137] M. T. Rahman *et al.*, "Metallic 1T Phase Tungsten Disulfide Microflowers for Trace Level Detection of Hg2+ Ions," *Advanced Sustainable Systems,* p. 2000068.

[138] F.-G. Banica, *Chemical sensors and biosensors: fundamentals and applications*. John Wiley & Sons, 2012.

[139] P. Li, D. Zhang, C. Jiang, X. Zong, and Y. Cao, "Ultra-sensitive suspended atomically thin-layered black phosphorus mercury sensors," *Biosensors and Bioelectronics,* vol. 98, pp. 68-75, 2017.

[140] Z. Meng, R. M. Stolz, L. Mendecki, and K. A. Mirica, "Electrically-transduced chemical sensors based on two-dimensional nanomaterials," *Chemical reviews,* vol. 119, no. 1, pp. 478-598, 2019.

[141] J. R. Vig and F. L. Walls, "A review of sensor sensitivity and stability," in *Proceedings of the 2000 IEEE/EIA International Frequency Control Symposium and Exhibition (Cat. No. 00CH37052)*, 2000, pp. 30-33: IEEE.

[142] H.-P. Loock and P. D. Wentzell, "Detection limits of chemical sensors: Applications and misapplications," *Sensors and Actuators B: Chemical,* vol. 173, pp. 157-163, 2012.

[143] M. Püntener, T. Vigassy, E. Baier, A. Ceresa, and E. Pretsch, "Improving the lower detection limit of potentiometric sensors by covalently binding the ionophore to a polymer backbone," *Analytica chimica acta,* vol. 503, no. 2, pp. 187-194, 2004.

[144] D. C. Harris, *Quantitative chemical analysis*. Macmillan, 2010.

[145] K. Kalantar-zadeh, "Sensors Characteristics," in *Sensors*: Springer, 2013, pp. 11-28.

[146] L. Ma, Q. Wang, S. M. Islam, Y. Liu, S. Ma, and M. G. Kanatzidis, "Highly selective and efficient removal of heavy metals by layered double hydroxide intercalated with the MoS42–ion," *Journal of the American Chemical Society,* vol. 138, no. 8, pp. 2858-2866, 2016.

[147] (2019). *Model 600D Series Electrochemical Analyzer/Workstation*. Available: http://www.ijcambria-webshop.com/mall/Model%20CHI600D%20series%20specs.htm

[148] M. J. Reinhardt, "Metal complexes containing non-innocent ligands for functional materials," 2013.

[149] D. S. Aaron, "Transport in fuel cells: Electrochemical impedance spectroscopy and neutron imaging studies," Georgia Institute of Technology, 2010.

[150] M. A. R. Laskar *et al.*, "Phenylhydrazinium Iodide for Surface Passivation and Defects Suppression in Perovskite Solar Cells," *Advanced Functional Materials,* vol. 30, no. 22, p. 2000778, 2020.

[151] S. Abdulkarim, "Urea and rGO Additives to Iodine/Triiodide Electrolyte for Higher Efficiency Dye-sensitized Solar Cells," 2018.

[152] K. Chen *et al.*, "SnO 2 Nanoparticles Embedded Biochar as Anode Material in Lithium Ion Batteries," in *2019 IEEE International Conference on Electro Information Technology (EIT)*, 2019, pp. 1-4: IEEE.

[153] W. Su, M. Lin, H. Lee, M. Cho, W.-S. Choe, and Y. Lee, "Determination of endotoxin through an aptamer-based impedance biosensor," *Biosensors and Bioelectronics,* vol. 32, no. 1, pp. 32-36, 2012.
[154] K. M. Reza *et al.*, "Tailored PEDOT: PSS hole transport layer for higher performance in perovskite solar cells: enhancement of electrical and optical properties with improved morphology," *Journal of Energy Chemistry,* vol. 44, pp. 41-50, 2020.
[155] G. Instruments, "Basics of electrochemical impedance spectroscopy," *G. Instruments, Complex impedance in Corrosion,* pp. 1-30, 2007.
[156] *Standard Reduction Potential* Available: https://chem.libretexts.org/Bookshelves/Analytical_Chemistry/Supplemental_Modules_(Analytical_Chemistry)/Electrochemistry/Redox_Chemistry/Standard_Reduction_Potential
[157] *Standard Reduction Potentials*. Available: https://courses.lumenlearning.com/boundless-chemistry/chapter/standard-reduction-potentials/
[158] A. Townshend, "Standard potentials in aqueous solutions: Allen J. Bard, Roger Parsons and Joseph Jordan (Eds.), M. Dekker, New York, 1985 (ISBN 0-8247-7291-1). xii+ 834 pp. Price $29.95 (personal subscription)," ed: Elsevier, 1987.
[159] A. C. Ferrari and D. M. Basko, "Raman spectroscopy as a versatile tool for studying the properties of graphene," *Nature nanotechnology,* vol. 8, no. 4, p. 235, 2013.
[160] *Raman Spectroscopy*. Available: https://www.horiba.com/en_en/raman-imaging-and-spectroscopy/
[161] R. Yan *et al.*, "Thermal conductivity of monolayer molybdenum disulfide obtained from temperature-dependent Raman spectroscopy," *ACS nano,* vol. 8, no. 1, pp. 986-993, 2014.
[162] J. Paredes, S. Villar-Rodil, P. Solís-Fernández, A. Martínez-Alonso, and J. Tascon, "Atomic force and scanning tunneling microscopy imaging of graphene nanosheets derived from graphite oxide," *Langmuir,* vol. 25, no. 10, pp. 5957-5968, 2009.
[163] M. Zhou, Y. Zhai, and S. Dong, "Electrochemical sensing and biosensing platform based on chemically reduced graphene oxide," *Analytical chemistry,* vol. 81, no. 14, pp. 5603-5613, 2009.
[164] P. Graves and D. Gardiner, "Practical raman spectroscopy," *Springer,* 1989.
[165] W. H. Bragg and W. L. Bragg, "The reflection of X-rays by crystals," *Proceedings of the Royal Society of London. Series A, Containing Papers of a Mathematical and Physical Character,* vol. 88, no. 605, pp. 428-438, 1913.
[166] M. W. Tate *et al.*, "High dynamic range pixel array detector for scanning transmission electron microscopy," *Microscopy and Microanalysis,* vol. 22, no. 1, pp. 237-249, 2016.
[167] *FTIR Analysis* Available: https://rtilab.com/techniques/ftir-analysis/
[168] P. R. Griffiths and J. A. De Haseth, *Fourier transform infrared spectrometry*. John Wiley & Sons, 2007.
[169] A. Dato, V. Radmilovic, Z. Lee, J. Phillips, and M. Frenklach, "Substrate-free gas-phase synthesis of graphene sheets," *Nano letters,* vol. 8, no. 7, pp. 2012-2016, 2008.
[170] J. Wu *et al.*, "Facile synthesis of 3D graphene flowers for ultrasensitive and highly reversible gas sensing," *Advanced Functional Materials,* vol. 26, no. 41, pp. 7462-7469, 2016.
[171] S. Nimesh, R. Chandra, and N. Gupta, *Advances in nanomedicine for the delivery of therapeutic nucleic acids*. Woodhead Publishing, 2017.

[172] S. Liu, B. Weng, Z.-R. Tang, and Y.-J. Xu, "Constructing one-dimensional silver nanowire-doped reduced graphene oxide integrated with CdS nanowire network hybrid structures toward artificial photosynthesis," *Nanoscale,* vol. 7, no. 3, pp. 861-866, 2015.

[173] Y. Sun and Y. Xia, "Large-scale synthesis of uniform silver nanowires through a soft, self-seeding, polyol process," *Advanced Materials,* vol. 14, no. 11, pp. 833-837, 2002.

[174] J. Jiu, K. Murai, D. Kim, K. Kim, and K. Suganuma, "Preparation of Ag nanorods with high yield by polyol process," *Materials Chemistry and Physics,* vol. 114, no. 1, pp. 333-338, 2009.

[175] Z. Wang, H. Wang, Z. Zhang, and G. Liu, "Electrochemical determination of lead and cadmium in rice by a disposable bismuth/electrochemically reduced graphene/ionic liquid composite modified screen-printed electrode," *Sensors and Actuators B: Chemical,* vol. 199, pp. 7-14, 2014.

[176] L. Zhu, L. Xu, B. Huang, N. Jia, L. Tan, and S. Yao, "Simultaneous determination of Cd (II) and Pb (II) using square wave anodic stripping voltammetry at a gold nanoparticle-graphene-cysteine composite modified bismuth film electrode," *Electrochimica Acta,* vol. 115, pp. 471-477, 2014.

[177] S.-F. Zhou *et al.*, "Individual and simultaneous electrochemical detection toward heavy metal ions based on L-cysteine modified mesoporous MnFe2O4 nanocrystal clusters," *Journal of Alloys and Compounds,* vol. 721, pp. 492-500, 2017.

[178] Y. Lin, Y. Peng, and J. Di, "Electrochemical detection of Hg (II) ions based on nanoporous gold nanoparticles modified indium tin oxide electrode," *Sensors and Actuators B: Chemical,* vol. 220, pp. 1086-1090, 2015.

[179] A. L. Suherman *et al.*, "Electrochemical detection of ultratrace (picomolar) levels of Hg2+ using a silver nanoparticle-modified glassy carbon electrode," *Analytical chemistry,* vol. 89, no. 13, pp. 7166-7173, 2017.

[180] A. Ravikumar, P. Panneerselvam, and K. Radhakrishnan, "Fluorometric determination of lead (II) and mercury (II) based on their interaction with a complex formed between graphene oxide and a DNAzyme," *Microchimica Acta,* vol. 185, no. 1, p. 2, 2018.

[181] P. K. Sahoo, S. Sahoo, A. K. Satpati, and D. Bahadur, "Solvothermal synthesis of reduced graphene oxide/Au nanocomposite-modified electrode for the determination of inorganic mercury and electrochemical oxidation of toxic phenolic compounds," *Electrochimica Acta,* vol. 180, pp. 1023-1032, 2015/10/20/ 2015.

[182] J. Li, L. Lu, T. Kang, and S. Cheng, "Intense charge transfer surface based on graphene and thymine–Hg (II)–thymine base pairs for detection of Hg2+," *Biosensors and Bioelectronics,* vol. 77, pp. 740-745, 2016.

[183] M. Piao *et al.*, "Hydrothermal synthesis of stable metallic 1T phase WS2 nanosheets for thermoelectric application," *Nanotechnology,* vol. 29, no. 2, p. 025705, 2017.

[184] Z. Liu *et al.*, "Colloidal synthesis of 1T'phase dominated WS2 towards endurable electrocatalysis," *Nano Energy,* vol. 50, pp. 176-181, 2018.

[185] X. Zeng *et al.*, "Hierarchical nanocomposite of hollow N-doped carbon spheres decorated with ultrathin WS2 nanosheets for high-performance lithium-ion battery anode," *ACS applied materials & interfaces,* vol. 8, no. 29, pp. 18841-18848, 2016.

[186] X. Zhang, C. Wang, M. Xue, B. Lin, X. Ye, and W. Lei, "HYDROTHERMAL SYNTHESIS AND CHARACTERIZATION OF ULTRATHIN MoS 2 NANOSHEETS," *Chalcogenide letters,* vol. 13, no. 1, 2016.

[187] N. Gajić, Ž. Kamberović, Z. Anđić, J. Trpčevská, B. Plešingerova, and M. Korać, "Synthesis of tribological WS2 powder from WO3 prepared by ultrasonic spray pyrolysis (USP)," *Metals,* vol. 9, no. 3, p. 277, 2019.

[188] S. J. Hazarika and D. Mohanta, "Inorganic fullerene-type WS 2 nanoparticles: processing, characterization and its photocatalytic performance on malachite green," *Applied Physics A,* vol. 123, no. 5, p. 381, 2017.

[189] C. Li *et al.*, "Superelastic and Arbitrary-Shaped Graphene Aerogels with Sacrificial Skeleton of Melamine Foam for Varied Applications," *Advanced Functional Materials,* vol. 28, no. 8, p. 1704674, 2018.

[190] L. Lu *et al.*, "Nanochannel-confined graphene quantum dots for ultrasensitive electrochemical analysis of complex samples," *ACS nano,* vol. 12, no. 12, pp. 12673-12681, 2018.

[191] H. Yuan *et al.*, "Influence of metal–MoS2 interface on MoS2 transistor performance: Comparison of Ag and Ti contacts," *ACS applied materials & interfaces,* vol. 7, no. 2, pp. 1180-1187, 2015.

[192] A. Castellanos-Gomez *et al.*, "Local strain engineering in atomically thin MoS2," *Nano letters,* vol. 13, no. 11, pp. 5361-5366, 2013.